Characterization of the transverse phase space at the photo-injector test facility in DESY, Zeuthen site

Dissertation
zur Erlangung des Doktorgrades
des Department Physik
der Universität Hamburg

vorgelegt von
Lazar Staykov
aus Burgas

Hamburg
2008

Gutachter der Dissertation:	Prof. Dr. J. Rossbach Prof. Dr. S. Khan
Gutachter der Disputation:	Prof. Dr. J. Rossbach Dr. B. Schmidt
Datum der Disputation:	26. März 2009
Vorsitzende des Promotionsausschusses: Vorsitzender des Promotionsausschusses:	Prof. Dr. C. Hagner Prof. Dr. R. Klanner
Dekan der MIN-Fakultt:	Prof. Dr. H. Graener

Abstract

High brightness electron beams with charge of 1 nC and low transverse emittance are necessary for the functioning of advanced light sources such as the Free-electron Laser in Hamburg (FLASH) and the European X-ray FEL (XFEL). The photo-injector test facility at DESY, Zeuthen site (PITZ) is dedicated to the optimization of such electron beams. At PITZ the electrons are produced using an RF gun cavity operated at accelerating gradients of up to 60 MV/m. The gun is equipped with a pair of solenoids for the compensation of the emittance growth due to linear space charge forces. This solenoid compensation scheme is enhanced with a properly matched TESLA type normal conducting booster cavity. The main tool for the characterization of the transverse phase space of the electron beam at PITZ is the emittance measurement system (EMSY). It employs the single slit method for the measurement of the transverse phase space distribution of the electron beam. In this thesis, the performance of the EMSY was optimized for measurement of low emittances in a wide range of photo-injector parameters including such that result in electron beams close to the XFEL specifications. First results on the characterization of the PITZ photo-injector with a gun operated at maximum accelerating gradient of 60 MV/m are presented. This includes scans of the solenoid focusing strength, the initial beam size and the booster gradient. A comparisson between results obtained at lower accelerating gradients is made with emphasize on the benefit of higher accelerating gradient.

Zusammenfassung

Für den Betrieb von Freien-Elektronen-Lasern (FEL), wie FLASH in Hamburg und den zukünftigen Europäischen X-FEL, sind Elektronenstrahlen hoher Brillianz und niedriger transversaler Emittanz bei einer Ladung von 1 nC notwendig. Der Photo-Injektor-Teststand am DESY - Standort Zeuthen (PITZ) beschäftigt sich speziell mit der Optimierung derartiger Elektronenstrahlen. Bei PITZ werden die Elektronen in einer Hochfrequenz-Elektronenquelle erzeugt, welche mit Gradienten von bis zu 60 MV/m betrieben wird. Zur Kompensation des durch Raumladungseffekte hervorgerufenen Anwachsens der Emittanz ist die Elektronenquelle mit zwei Solenoiden ausgestattet. Diese Kompensation wird durch eine normal leitende TESLA - Beschleunigungsstruktur verstärkt. Die Charakterisierung der Elektronenstrahlen erfolgt hauptsächliche mit einem System zur Emittanzmessung (EMSY), bei dem mit Hilfe der Einzel-Schlitz-Methode der transversale Phasenraum vermessen wird. Im Rahmen dieser Dissertation wurde das Messsystem für die Messung kleiner Emittanzen bei verschiedenen Parametern des Photoinjektors, einschliesslich derer zur Erfüllung der XFEL-Spezifikationen, optimiert. Erste Ergebnisse der Charakter-

isierung einer Elektronenquelle, die mit maximalen Beschleunigungsgradienten von 60 MV/m betrieben wurde, werden präsentiert. Dies beinhaltet das Scannen der Solenoidfeldstärke, der Elektronenstrahlgrösse bei der Emission sowie verschiedene Gradienten der TESLA Kavität. Der Vorteil hoher Beschleunigungsgradienten wird durch einen Vergleich verschiedener Gradienten demonstriert.

To my family,

the most incredible source of power and inspiration.

Contents

List of Figures

List of Tables

Chapter 1

Introduction

Since the beginning of the human civilization, there has been a continual striving for powerful and reliable light sources that are used for improved comfort, protection, hunting, learning etc. In many cultures, the light sources were placed at the highest rank of the society, the God divine. However, modern man's astoundment falls mostly into knowledge. Knowledge needs light to be shed on specific objects for revealing the imperceptible details. Generally speaking a light source is an emitter of electromagnetic radiation of desired properties. A possible characterization of a photon beam can be given in terms of brilliance. It is defined as the number of photons per given cross section per opening angle per unit time and 0.1% bandwidth [1]. As such it is given in terms of $photons/s/mm^2/mrad^2/0.1\%$ BW, where 0.1% BW denotes a bandwidth of 10^{-3} centred around the frequency ω. The broadest range of photon beam properties in the present day is covered by the accelerator-based light sources, synchrotron light sources or Free Electron Lasers (FELs). In an accelerator based light source, electron beams moving with relativistic speed produce photon beams under the influence of external magnetic fields. Therefore the properties of the electron beam, namely the brightness, determine the properties of the photon beam. The accelerator based light sources cover the electromagnetic spectrum, from THz radiation to ultra hard X-rays [2]. All this combined with the high brilliance and high degree of spatial coherence makes this type of light sources indispensable in many areas of research, i.e. biosciences, medical research, chemical and environmental sciences, advanced materials, engineering etc.

The most challenging demand in the present day is the production of extremely short, ultra high brightness laser pulses with wavelengths reaching down to 1 Å and high spatial coherence. The only source that can meet these requirements is the Free Electron Laser (FEL). In contrast to the conventional lasers where the electrons are bound to some atomic or molecular states of the lasing media, an FEL uses a relativistic electron beam, therefore it is called "free-electron" laser. In an FEL, a relativistic electron beam passes through the periodic magnetic field of an undulator superimposed with an electromagnetic wave which results in a stimulated emission of light. For the wavelengths down to an Å the only mechanism for generation of coherent light pulses is the Self Amplified Spontaneous Emission of light which can be achieved only in a single pass through the undulator. The characteristics of the emitted light are determined by the electron beam energy and spatial distribution, and the magnetic field characteristics of the undulator.

For the operation of an FEL, electron beam of a very special properties is required. The emittance is used as a figure of merit describing the electron beam quality. It is related to the volume occupied by the electrons in the phase space. More specifically, a sufficiently high electron phase space density i.e. a bunch consisting of a large number of high energy electrons with small energy spread contained in a small volume with similar flight direction of all the electrons. Roughly speaking the product of the transverse rms beam size and the rms angular spread of the flight directions of the electrons is called transverse *geometrical emittance* of the beam. Another quantity often used in order to compare the emittance of beams with different kinetic energy is the normalized emittance, which is simply the geometrical emittance multiplied by the relativistic and the Lorentz factors $\beta\gamma$ of the electrons.

To test and to study the possibilities for creation of electron beams with minimum emittance, the Photo Injector Test facility at DESY, Zeuthen site (PITZ) was created [3].

In this thesis, a short description of the FEL principle is given in Chapter 2 as well as a motivation for the requirements to the electron beam. A detailed description of the Photo Injector Test Facility at DESY, Zeuthen site, (PITZ)

is located in Chapter 3. The beam dynamics in the photo-injector is briefly described in Chapter 4. Different techniques used for the characterization of the transverse phase space of an electron beam is given in Chapter 5. In the same chapter a detailed description of the single slit method, which is employed at PITZ, and a detailed analysis of the uncertainty and the systematic deviations related to this method is made. In Chapter 6, experimental results from the characterization of the electron beam transverse phase space are given. Analysis of the phase space density in different charge contours is made in Chapter 7. Chapter 8 include numerical optimization of the PITZ photo-injector for different bunch charges and a performance estimation of the single slit method at this optimized points. Conclusions and outlook are placed in Chapter 9. A description of the image processing algorithm that was used for the data analysis is placed in Appendix A. The procedures necessary for proper phase space characterization at PITZ are given in Appendix B together with a list of criteria for data consistency.

Chapter 2

Electron beams for Free Electron Lasers

The FEL is able to produce ultra-short UV or X-ray pulses, with high brilliance and spatial coherence. Presently it is believed that this can be achieved only in the single pass Self Amplified Spontaneous Emission (SASE) FELs by combination of electron beam with very special properties and the undulator magnetic field. When certain relations between the undulator and the electron beam parameters are fullfiled, the electrons interact resonantly with an existing electro-magnetic field thus emitting coherent almost monochromatic light. The SASE process is characterized by several different phases: start-up from shot noise - where the *"ignition"* of SASE is achieved in the first part of the undulator, exponential growth and saturation. Optimal operation of a SASE FEL is in the last phase - saturation.

After the successful demonstration of SASE-FEL operating at VUV wavelengths at 80 and 120 nm performed at the TESLA Test Facility (TTF) in DESY Hamburg site [4, 5], the European X-ray FEL (XFEL) was proposed in 2003 [6]. The goal of XFEL is to produce FEL radiation pulses with peak brilliance of 5.0x10^{33} $photons/s/mm^2/mrad^2/0.1\%$ BW at wavelengths down to 0.1 nm which corresponds to a photon energy of 12.4 keV, already in the X-ray region of the light spectrum. For this to be achieved an electron beam with kinetic energy of 17.5 GeV is required.

In this chapter I will give a short introduction to the main principles behind a successful FEL operation in the single pass SASE regime. This includes

properties of the undulator magnet and the electron beam that is required.

2.1 Description of the FEL

Two main components are required for FEL operation, the electron beam and a periodic magnetic structure called undulator magnet. Electro-magnetic radiation is produced as the electron beam passes through the undulator. A schematic representation of the process is shown in figure 2.1. Important notation there is the coordinate system that is going to be used in this thesis. The electrons are moving along the z axis, called *longitudinal*. The vertical and horizontal *transverse* axes are y and x, respectively.

An undulator is typically made of permanent magnet dipole blocks ar-

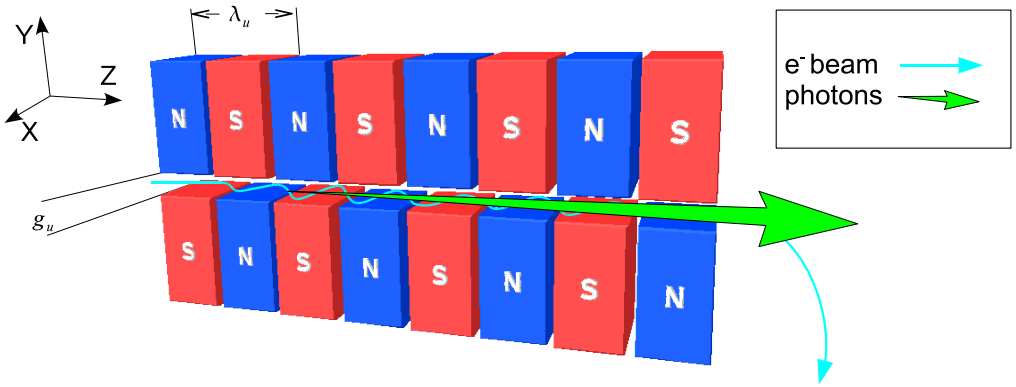

Figure 2.1: Schematic layout of a planar undulator and FEL process. The trajectory of the electrons is shown with cyan blue line, the emitted light is shown as green arrow, the bending of the trajectory under the influence of the magnetic field of the undulator is exaggerated.

ranged with alternating polarity in the longitudinal direction (see fig. 2.1). Typical parameters of the undulator are the gap between the poles g_u, the distance between a pair of dipoles or the period λ_u and the peak magnetic field on axis $\tilde{B}$. An important quantity used for undulator characterization is the so called undulator parameter K [2]:

$$K = \frac{\lambda_u e \tilde{B}}{2\pi m_e c^2}, \tag{2.1}$$

where e and m_e are the electron charge and mass, c is the speed of light in vacuum and $\tilde{B}$ is the magnetic field on the undulator axis. For a planar sinusoidal undulator $\tilde{B} = B_0/cosh(\pi\frac{g_u}{\lambda_u})$, where B_0 is the flux density in the middle of the poletip.

There is a strict relation between the undulator parameter and the performance of the FEL, namely that the undulator radiation emitted during the passage of the electrons through the undulator will be amplified at the resonance wavelength λ_r shown on equation 2.2:

$$\lambda_r = \frac{\lambda_u}{2\gamma^2}\left(1 + \frac{K^2}{2}\right), \tag{2.2}$$

where $\gamma = (1-\beta^2)^{-1/2}$ is the relativistic Lorentz factor, $\beta = v/c$ where v is the speed of the electrons.

Table 2.1: Working parameters of FLASH as of June 2007.

Parameter	**Value**	**Units**
Electron beam:		
normalized emittance	2.0	$[mm\ mrad]$
nominal bunch charge	1.0	$[nC]$
peak current	2500	$[A]$
momentum	700	$[MeV/c]$
Undulator:		
gap	12	$[mm]$
period	2.73	$[cm]$
length	6×4.5	$[m]$
peak field on-axis	0.47	$[T]$
FEL beam:		
saturation wavelength	13.2	$[nm]$
pulse duration	10	$[fs]$
peak power	≤20	$[GW]$

An important implication from equation 2.2 is that the radiation wavelength which will be amplified in the FEL process can be tuned by changing either the undulator parameter (i.e. pole gap g_u) or the momentum of the electrons. Since change of electron beam momentum involves changing the

whole lattice of the accelerator, it is more practical to change the pole gap of the undulator instead [6]. Typically all the other parameters of an FEL are optimized for the shortest achievable wavelength. An example for optimized parameters [7] of the electron beam at the Free Electron Laser in Hamburg (FLASH) are given in table 2.1.

2.2 Requirements for the electron beam

There are several limitations to the minimum wavelength that can be amplified up to saturation. The lower limit is given by the growth of the uncorrelated energy spread of the electrons induced from quantum fluctuations of the undulator radiation [8]. This effect is proportional to γ^4 and poses a fundamental limit on achieving very short wavelengths. Another constraint on the minimum wavelength of the FEL radiation comes from the electron beam distribution. It is shown in [8–10] that the minimum achievable wavelength can be expressed as:

$$\lambda_{min} \simeq 18\pi\varepsilon_n \frac{\Delta E}{E} \left[\frac{\gamma I_A}{I_p} \frac{1+K^2}{K^2} \right]^{1/2} \tag{2.3}$$

where ε_n is the normalized transverse emittance of the electron beam[1], E is the nominal beam energy, ΔE is the energy spread of the electrons, I_p is the beam peak current, I_A is the Alfven current $\simeq 17\ kA$.

As can be seen from equation 2.3, when moving toward short wavelengths one must keep the energy spread and the emittance of the electron beam as low as possible and the peak current as high as possible. These requirements are contradictory because higher peak current means stronger influence of the space charge induced effects which degrade both the emittance and the energy spread of the electrons.

Another important parameter of the FEL is the gain length L_g (equation 2.4) or the path length through the undulator at which the radiation power is increased by a factor of e. Here the emittance again plays a significant role

[1] detailed definition of the transverse beam emittance is given in chapter 4

$$L_g \simeq 1.6\varepsilon\gamma^2 \left[\frac{\gamma I_A}{I_p\,(1+K^2)\,K^2}\right]^{1/2} \tag{2.4}$$

SASE FEL operation in saturation can be achieved only if the undulator length is sufficiently larger than L_g. It is estimated that saturation can be reached after about twenty gain lengths [9]. An additional constraint is the transverse coherence condition:

$$\varepsilon_n \leq \frac{\gamma\lambda_r}{4\pi}, \tag{2.5}$$

which imposes another important requirement for the electron beam transverse phase space, namely that the realization of SASE FEL operation at a given wavelength can only be achieved if the emittance of the electron beam is sufficiently small.

Following the above mentioned relations in equations 2.3-2.5 one can define the requirements for the electron beam in order to have SASE FEL operation in the saturation regime. It was estimated [6] that in order to reach the planned characteristics for the Euro XFEL, peak current of 5 kA is needed where the kinetic energy of the electrons must be 17.5 GeV with energy spread of 1 MeV and the projected transverse normalized emittance of at most 1.4 $mm \cdot mrad$. Since the beam quality can only be degraded from the source to the entrance of the undulator, even higher quality of 0.9 $mm \cdot mrad$ must be reached still at the source.

Chapter 3

PITZ

3.1 Overview

The Photo Injector Test facility at DESY, Zeuthen site (PITZ) was proposed in 1999 as a research and development project for electron sources with short bunch length and small emittance [3]. It is now a big collaboration including different research institutes, laboratories and universities, namely BESSY in Berlin, Daresbury Laboratory, DESY (Zeuthen and Hamburg), FZ Rossendorf, Humboldt University, INFN Frascati, INFN Milano, INR Troitsk, INRNE Sofia, LAL Orsay, MBI Berlin, TU Darmstadt - TEMF, University of Hamburg and Yerevan Physics Institute.

The goal of PITZ is to develop and optimize photo-injector electron sources that can fulfill the requirements for FLASH and the European XFEL [6].

During the time this work was performed, PITZ was equipped with a Nd:YLF photo cathode laser illuminating a cesium telluride (Cs_2Te) cathode which is placed in the half cell of a 1.6 cell L band (1.3 GHz) RF gun followed by a booster cavity, both cavities are made of copper. The cavities are fed by different RF sources. A solenoid magnet near the gun cavity is provided for the emittance compensation [11] and another solenoid called bucking is placed behind the gun in order to compensate the magnetic field of the main solenoid reaching the cathode. The beamline is equipped with various diagnostics for characterization of the longitudinal and transverse distribution of the electron beam. The schematic layout of the PITZ components is shown on figure 3.1.

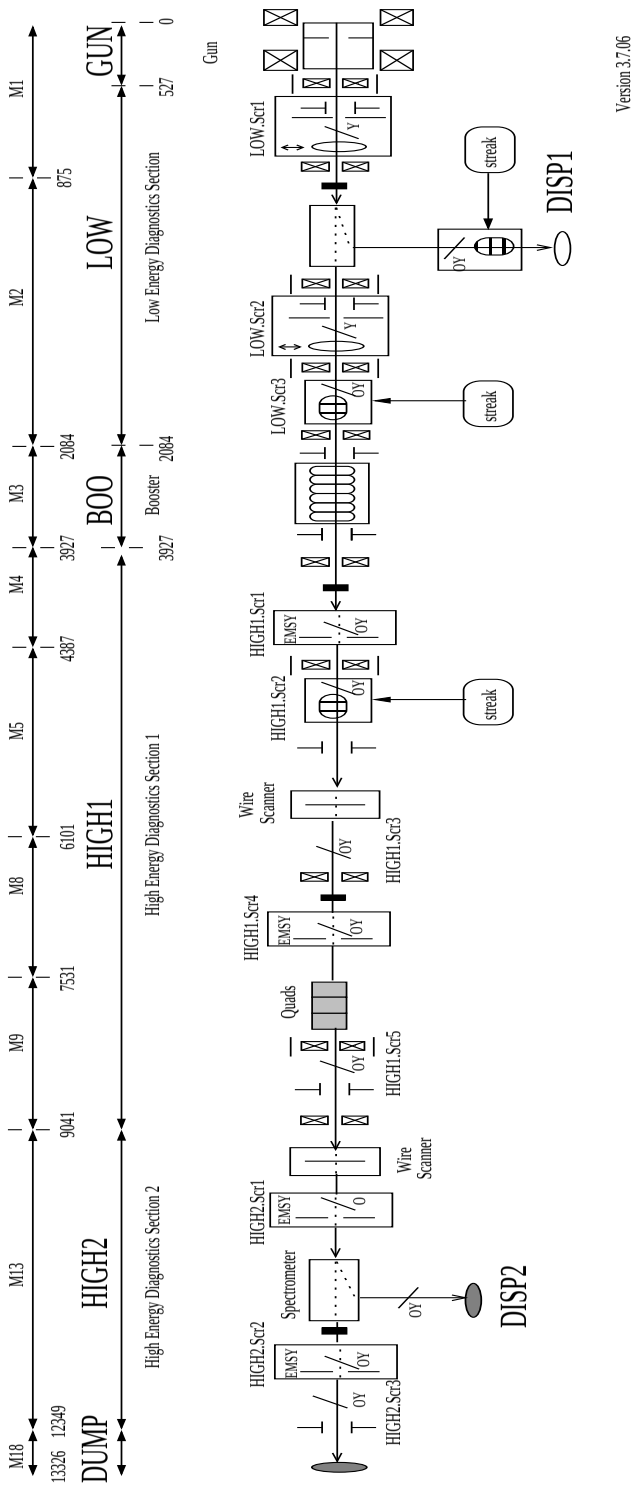

Figure 3.1: Schematic layout of PITZ. The electrons are accelerated from top. Screens are marked as O in the case of OTR and Y in the case of YAG, *streak* stays for readout to the streak camera for analysis of the electrons longitudinal distribution, *DISP* is dipole spectrometer magnet.

3.2 Subsystems

3.2.1 RF system

The RF system of PITZ consists of two separate RF stations providing pulsed power for extraction and acceleration of the electrons from the gun and through the booster cavity. Each station is equipped with a klystron, an HV modulator, pulse transformer network, preamplifier and a waveguide system for the delivery of the RF power to the cavities. An advanced low-level RF control system (LLRF) is dedicated to the control of the RF pulse shape, amplitude and phase. Interlock and control systems provide protection of the different components of the RF stations.

The klystrons installed at PITZ are produced by THALES [12] and are operating at 1.3 GHz with a bandwidth of about 1 MHz. Presently two different models are in use, TH2104-C and TH1801-MBK, with the first one delivering up to 5 MW of peak power. The second is a 10 MW multibeam klystron which aims to fulfill the XFEL specifications on power and efficiency [6]. The RF system is able to deliver pulsed power with a repetition rate of 10 Hz and RF pulse duration of more than 900 μs.

The RF power is delivered to the cavities through about 20 m rectangular waveguides filled with SF_6 to improve conductivity and to suppress sparks. Because of limitations in the available RF-to-vacuum windows, the power from the 10 MW klystron is separated in two waveguides and delivered to the RF gun with a T-combiner equipped with two RF windows. The phase between both waves is controlled with a motor controlled phase shifter.

The LLRF control of the 5 MW klystron consists of DSP boards and is meant to compensate phase and amplitude variations within the flat top duration of the RF pulse caused by modulator voltage ripples or thermal shifts in power cables or accelerating structures. The forward and the reflected power are measured with directional waveguide coupler and the control is realized via the klystron preamplifier.

3.2.2 Cathode laser system

The laser system of PITZ consists of a diode pumped laser, a laser beamline to transport and image the laser light to the cathode and diagnostics for the laser pulse intensity and temporal and spatial distribution. To fulfill the XFEL requirements, the laser pulse must have round, uniform transverse and flat top longitudinal distributions [13].

A schematic of the diode pumped laser is shown on figure 3.2. It is designed to produce short laser pulses, stacked in trains of up to 800 separated by 1 μs with a train repetition rate of up to 10 Hz. The laser system is developed by Max-Born Institute (MBI) in Berlin.

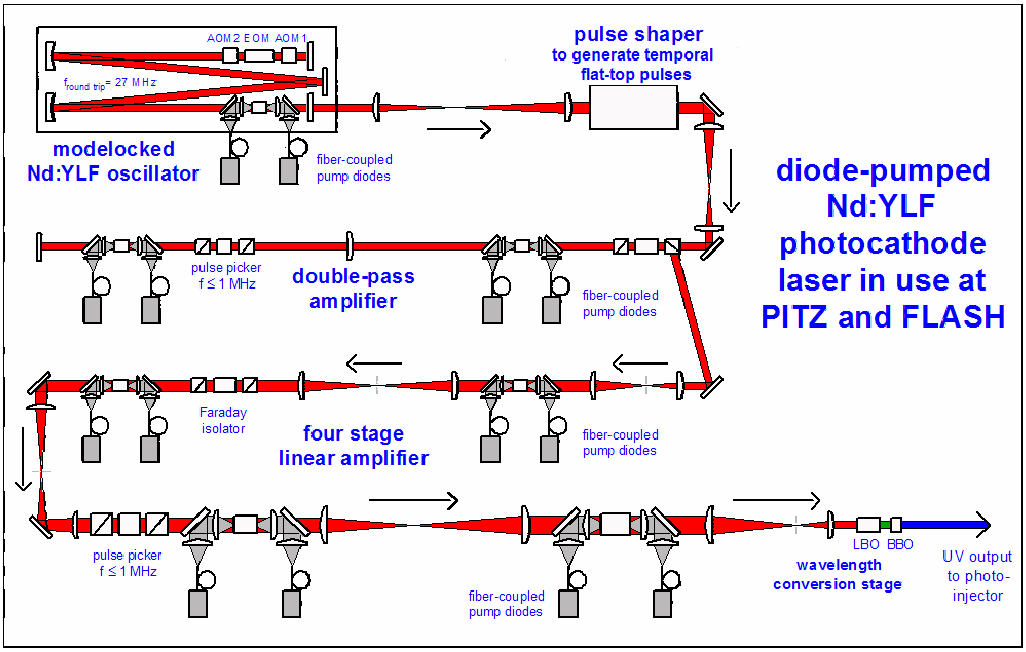

Figure 3.2: Schematic layout of PITZ laser.

A single laser pulse with a wavelength of 1048 nm and Gaussian distribution is produced by a mode locked pulse train oscillator (PTO). The pulse is shaped longitudinally by means of a grating stretcher and birefringent crystals, resulting in a trapezoidal intensity distribution with about 20 ps FWHM and rise-/fall times of 6-8 ps. The pulse shaper is followed by six stages of diode pumped Nd:YLF amplifiers, pulse picker and wavelength conversion crystals where the fourth harmonic or 262 nm is selected since the Cs_2Te cathode

quantum efficiency is higher at this wavelength. The intensity of the laser pulses is varied with an attenuator placed at the exit of the laser system thus keeping the thermal conditions in the lasing media stable. In order to reach the parameters required for the XFEL, namely the rise and fall times of the longitudinal laser pulse shape, an upgrade of the laser system was made in summer 2008.

The laser light is transported to the cathode through the laser beam-line (LBL) [14]. The LBL consists of lenses and mirrors and a beam shaping aperture (BSA) all with a total length of about 20 m. The uniformity of the transverse intensity distribution is achieved by cutting a round spot from the center of a widened Gaussian distribution. Further, the light is relay imaged on the photo cathode.

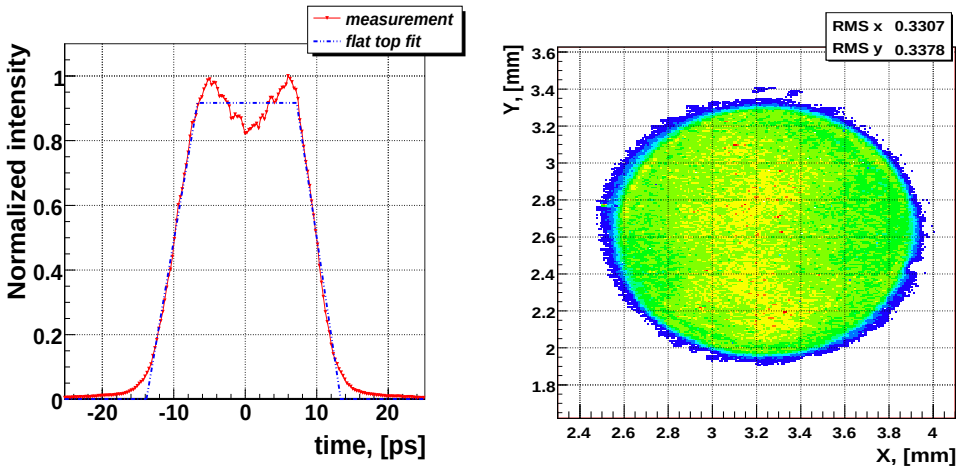

(a) longitudinal (projection) (b) transverse

Figure 3.3: Typical distribution of the laser pulse.

The stability of the laser parameters, such as pulse energy, transverse distribution and jitter in the transverse position is monitored at the so called virtual cathodes (VCs) [15], to which the laser beam is deflected. For monitoring purpose a fraction of the laser light is deflected via a beam splitter and can be monitored during the operation of the photo-injector. The VC is placed next to the real cathode at an optically equivalent position. The laser diagnostics system contains a PMT for monitoring the intensity of the different pulses in the pulse train, an UV sensitive CCD camera which is illuminated by

the laser for observation and measurement of the transverse distribution of the laser and a quadrant diode for monitoring of the transverse position jitter [16]. An image of the typical transverse and longitudinal laser distribution is shown in figure 3.3.

The longitudinal distribution of the UV laser pulse is monitored with a streak camera (Hamamatsu C5680) [17]. The streak camera is synchroscan enabled, which allows overlaying of multiple pulses to increase the signal amplitude. This device has 2 *ps* temporal resolution for UV pulses. An experimental procedure for real time optimization of the longitudinal laser shape has been developed [18]. It consists of tuning four parameters of the pulse shaper to minimize the emittance growth due to imperfections in the longitudinal laser shape.

3.2.3 Vacuum system

The vacuum system at PITZ is designed to provide stable operation conditions for the RF cavities. Special attention goes to hydrocarbons or oxygen containing gases due to the high risk of poisoning and degradation of the Cs_2Te layer of the photocathode. An additional constraint is particle free environment due to the possibility of operation of the RF gun close to the cryogenic cavities in FLASH and XFEL. In addition, the particle free environment reduces the risk of occurrence of field emitters at high accelerating gradient in the gun cavity. The vacuum system consists of turbo-molecular pumps and a combination of Ion Getter Pumps (IGP) and Titanium Sublimation Pumps (TSP). The initial pressure of 10^{-3} to 10^{-4} *mbar* is provided by turbo-molecular pumps. The IGP's are then started to reach pressures on the order of 10^{-8} *mbar* when the TSP's are activated. As nominal operating pressure in the gun cavity is considered 10^{-9} *mbar*.

In addition, some diagnostics components such as bunch length measurement stations are equipped with aerogel, a material well known for its high outgasing rate. Such devices are separately contained and additionally supplied with IGP's in order to prevent the spread of gases and particles to other parts of the vacuum system.

3.2.4 Control and interlock systems

The control of the accelerator is achieved with the help of a dedicated control environment, the so called control system. The control system allows remote control of various inaccessible components of the machine during operation. It maintains the data flow from/to the end devices, monitors critical operational parameters close to real time and is able to interrupt machine operation if dangerous limits are approached.

The control system integrates device oriented protocols like DOOCS (Distributed Object Oriented Control System) [19], TINE (Three-fold Integrated Networking Environment) [20] and various types of frontend firmware and real-time operating systems. This results in a flexible user interface for ease of integration of self made control and measurement software written in C++, Matlab, LabVIEW etc.

3.2.5 Water Regulation System

The water regulation system (WRS) is used to provide cooling power to various systems at PITZ, i.e., the RF system, the laser system. Also precise regulation of the body temperature of the RF cavities is achieved with the WRS, this means tuning of the resonant frequency of the cavity (see section 3.3.2).

3.3 Production of high quality electron beams

There are various methods of electron beam production, e.g., thermal or photo cathodes in DC guns, thermal cathodes in RF guns, needle cathode arrays etc. The photocathode RF gun scheme is used at PITZ. In this section, a short description of the components needed for production of the electron beam at PITZ is given.

3.3.1 Photocathode

Recently, photocathodes have become the primary choice for creation of electron beams for short wavelength FEL's. The main advantage of photocathodes is the possibility to strictly control the spatial and temporal distribution of

the electron bunch using a combination of well defined laser pulse and high-gradient accelerating field. General characteristics of a photocathode are short response time, high quantum efficiency (QE), uniformity of the QE area, high current densities (hundreds of Amperes per square centimeter) and long life-time. Many factors such as bad vacuum conditions, high levels of dark current or the high electric field in the cavity can have strong impact on the cathode lifetime.

An additional constraint in the case of low emittance photo-injectors is also the thermal emittance which is related to the remnant kinetic energy of the electrons as they leave the cathode and the initial beam size of the electron beam. A more detailed description of the thermal emittance is given in section 4.2.1

In PITZ the semiconductor Cs_2Te is chosen as a photo sensitive material for the electron extraction. It has the advantage of relatively good balance between lifetime, QE and ease of production [21]. The Cs_2Te has a bandgap energy of 3.3 eV and an electron affinity of 0.2 eV. This implies that the photo-effect can take place only with photons in the UV range.

The cathodes used in PITZ are produced by LASA in INFN-Milano. A thin layer of Cs_2Te is deposited in the center of a Molybdenum (Mo) cylinder that is used to plug the cathode in the gun cavity. The QE was measured at PITZ for 262 nm to be on the order of 10 % for fresh cathodes [22]. However in the harsh operating conditions inside the gun, the QE decreases over time reaching about 2 % after 100 hours of operation, as observed at PITZ at gradients of 60 MV/m [23].

3.3.2 Gun cavity

In order to preserve the desired initial beam shape and to contain the bunch in a small phase space volume, rapid acceleration of the electrons is required. From the numerical optimization of the photo-injector it was found that an accelerating gradient of 60 MV/m is needed in order to reach the desired beam quality as specified in [6] (see chapter. 4). To obtain such a high gradient a one-and-a-half cell normal conducting copper cavity is used (the scheme of the RF gun with the solenoids is shown on fig. 3.4). The gun was designed in DESY, Hamburg site [24] and so far was successfully operated in TTF phases 1 and

2 and presently in FLASH [6]. In the framework of this thesis two identical cavity prototypes called 3.1 and 3.2 were conditioned and characterized.

When the RF power pulse is fed through the coaxial coupler in the gun, the

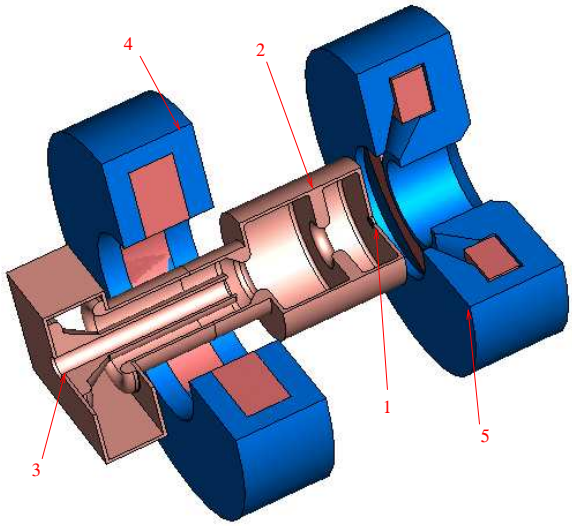

Figure 3.4: Sketch of the RF gun with the solenoids: 1 - Cs_2Te cathode; 2 - copper gun cavity; 3 - coaxial coupler; 4 - main solenoid magnet; 5 - bucking solenoid.

energy of the pulse is stored as a standing wave in a TM_{010} mode with resonant frequency of 1.3 GHz. In this way, the cavity acts like an oscillator with a quality factor Q_{cav}:

$$Q_{cav} = \frac{f_r}{\Delta f}, \tag{3.1}$$

where f_r is the resonant frequency and Δf is the width of the resonance defined as the frequency shift at which the amplitude is reduced by 3 dB [1].

For the PITZ gun, the quality factor Q_{cav} was simulated using the numerical code Superfish and results were presented in [24, 25]. Measurements confirmed Q_{cav} to be about 2.4×10^4 for the cavity prototype 3.1 and 3.2 (see [26, 27]). This implies that the width of the resonance Δf is about 54 kHz.

The resonance frequency of a pill-box cavity in TM_{010} mode is given by the relation equation 3.2

$$f_r = \frac{x_1 c}{2\pi R_{cav}}, \tag{3.2}$$

where R_{cav} is the inner radius of the cavity, x_1 is the first zero of the cylindrical Bessel function and f_r is the resonance frequency [1].

From equation 3.2 one can see that tiny changes in the cavity radius will result in a large shift of the resonance frequency i.e. 1 μm change of the R_{cav} will result in 14.7 kHz change of f_r. In PITZ the regulation of the cavity radius, therefore the resonant frequency, is achieved with a strict control of the body temperature. Taking into account the coefficient of thermal expansion of copper to be 16.8 $\mu m/m/K^o$ will lead to -21.8 kHz/K^o frequency shift. At this shift almost half of the power forwarded to the cavity will be reflected. Since the RF gun geometry is slightly different from the idealized pill-box cavity, the real frequency shift is a more complicated issue. However it was measured experimentally to be about -23 kHz/K^o [25] which is in fairly good agreement with the theory.

The relation between the RF power and the amplitude of the wave in $TM_{010,\pi}$ is shown on equation 3.3 from where R_s is the so called shunt impedance, which gives the amount of RF power that is dissipated in the walls as heat [1].

$$U_{cav} = \sqrt{2P_{RF}R_s} \tag{3.3}$$

This expression is valid if the frequency of the forward wave and the cavity resonant frequency are the same. In [25] it was numerically estimated that the accelerating gradient on the cathode can be expressed as:

$$E_{acc} = 23.336\sqrt{P_{RF}} \tag{3.4}$$

Again this is only valid if there is perfect coupling between the waveguide and the RF gun and that the gun is operating exactly at resonance frequency. Considering E_{acc} to be 60 MV/m will require RF power delivered in the gun of about 6.6 MW. Taking into account equation 3.3 and the XFEL specifications, 700 μs duration of the RF pulse, 10 Hz repetition rate will bring average power load of the cavity of about 46 kW. The water regulation system (WRS) can provide stable temperature with 0.1 K° peak to peak stability. The associated amplitude and phase drifts must be compensated from the LLRF control.

The longitudinal (accelerating) component of the electric field can be written as:

$$E_z = E(z)sin(2\pi ft + \phi_0), \tag{3.5}$$

here $E(z)$ is the longitudinal shape of the electric field[1]; ϕ_0 is the phase at which the electron leaves the cathode. The simulated shape of $E(z)$ is shown on figure 3.5.

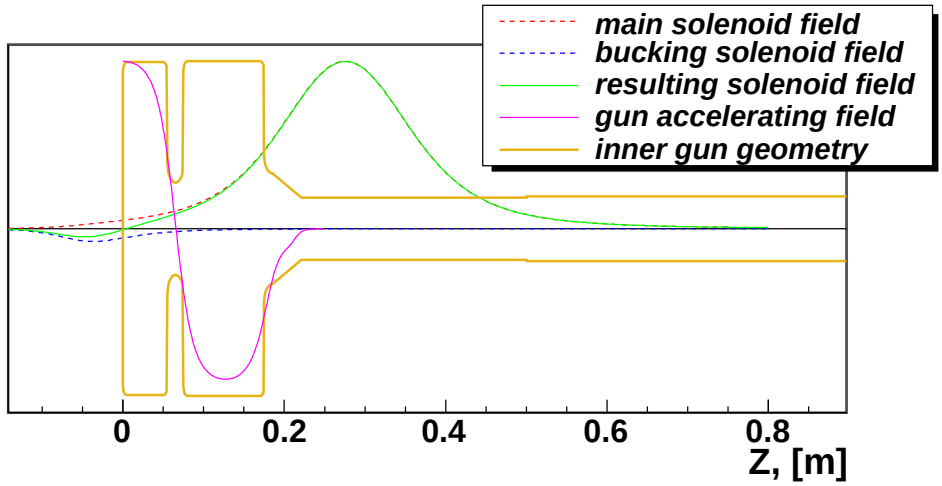

Figure 3.5: Aperture and fields distribution in the gun area; the vertical axis is in arbitrary units.

3.3.3 Solenoids

A pair of solenoids is installed around the gun (see figure 3.4), one (main solenoid) used for focusing and space charge compensation of the electron beam, the other called bucking is meant to counter the remnant magnetic field on the cathode created from the main solenoid in order to remove any initial angular momentum. The dependence of the transverse emittance on the remnant magnetic field on the cathode surface was studied in details in [28], where also the theoretical basis for the emittance degradation is described in the appendix.

The longitudinal component of the solenoid field is shown on figure 3.5. For practical reasons, later on on this thesis, the peak value of the magnetic field will be expressed in the units of the current in the magnet power supply, Amperes. The relation between the current in the magnet power supply and the peak field was measured in [29]. The calibration constant for the main solenoid is 5.8838×10^{-4} $[T/A]$. The main solenoid is placed such that the

[1] this shape depends on the inner geometry of the cavity and can not be expressed by a simple analytic formula

peak field is at 0.275 m from the cathode position. The solenoid focusing is major part of the so called emittance compensation scheme [11,30]. The main idea of this scheme is to cancel the correlation induced by the space charge in the beginning of the acceleration.

3.3.4 Booster cavity

An essential part of the emittance compensation scheme is applying acceleration further downstream. This is achieved with a booster cavity that is a copper normal conducting 9 cell TESLA prototype [31].

The booster is powered from the 5 MW TH2104-C klystron. The maximum accelerating gradient is estimated to be 14.75 MV/m. It was successfully conditioned in 2005 [31] and first beam measurements were done in 2006.

Presently a new booster cavity of a type Cut Disk Structure [32] is under construction at DESY, Hamburg site. The new cavity will have 14 cells and will allow higher accelerating field, resulting in higher beam momentum with improved stability and field uniformity. The accelerating component of the electric field distribution of the TESLA and the CDS booster cavities is shown on figure 3.6.

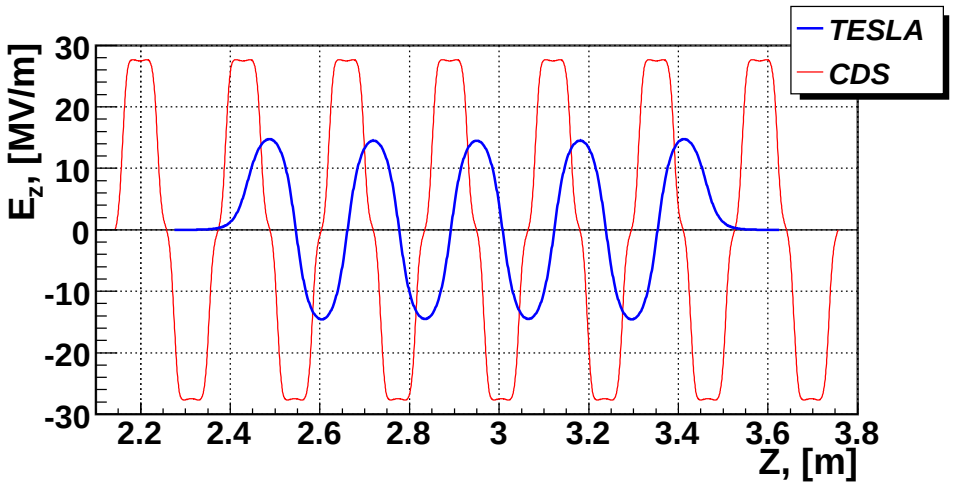

Figure 3.6: Fields distribution in the 9 cell TESLA type and the 14 cell CDS type booster cavities. Simulation with Superfish.

3.4 Electron beam diagnostics

As can be seen on figure 3.1, PITZ is abundant with various diagnostics components needed for the complete characterization of the electron beam. The different diagnostics can be separated in charge measurement devices, diagnostics of the longitudinal distribution of the electrons, i.e., mean momentum, momentum spread and current distribution, and transverse distribution diagnostics including emittance. The main difference between transverse and longitudinal diagnostics is the corresponding momentum range, on the order of MeV for the longitudinal and few keV for the transverse distribution.

3.4.1 Charge measurements

The net charge of the bunch is measured with two different devices, an Integrating Current Transformer (ICT) from *Bergoz* [33] and a Faraday Cup (FC) produced at DESY, Hamburg site. The ICT's provide non-interceptive diagnostics but offer lower sensitivity which makes them inappropriate for charges lower than 100 pC. The FC penetrates the beam path thus completely destroying the beam, and is used in case of low charge measurements (below 100 pC), as well as for dark current measurement.

3.4.2 Diagnostics of the longitudinal distribution

Longitudinally the electrons occupy two orthogonal dimensions in phase space, the spatial/temporal and the momentum. For measurements of the momentum distribution of the electrons a dispersive dipole magnet is used [34]. The measurement principle is based on the fact that the bending of the trajectory of an electron moving in magnetic field perpendicular to the magnetic field lines is proportional to the field strength and inversely proportional to the momentum of the electron. This implies that the momentum distribution in the bunch of electrons will be translated in a spatial distribution in the plane of dispersion. The resulting spatial distribution is observed via a charge-coupled device (CCD) camera and a Yttrium Aluminum Garnet (YAG) scintillator screen placed after the magnet. The image can be analyzed to reveal the mean momentum and the root mean square (RMS) of the momentum distribution. The error of the measured mean momentum is about 2.2 % [34].

For measurement of the temporal structure of the electron bunch, the electrons are passed through a radiating medium such as an Optical Transition Radiation (OTR) screen or a chamber filled with aerogel used as emitter of Cherenkov light. Further, this light is imaged on a streak camera (Hamamatsu-C5680) and the temporal distribution of the pulse is analyzed. Both measurements of momentum and temporal distribution can be combined for semi-simultaneous measurement that can be used for analysis of the correlated distribution of the electrons in the z p_z plane [35].

3.4.3 Diagnostics of the transverse distribution

The intensity distribution of the electrons in the transverse plane xy can be measured by a wire scanner (WS) [36] or with YAG or OTR screens observed by a CCD camera. The preferred method in PITZ is the screen based method since it offers the possibility to observe simultaneously the $2D$ distribution and can be used for single shot measurements. The WS delivers only separate x or y projections and needs to integrate many pulse trains thus losing information on the two dimensional distribution and accumulating position jitter that leads to increase of the uncertainty.

The YAG screens used in PITZ are typically mounted with normal incidence angle to the beam (see figure 3.7(a)). The emitted light is then directed through a set of mirrors to the CCD camera. The OTR screens are mounted with 45° degrees with respect to the beam axis (see figure 3.7(b)). The uncertainties and the systematic deviations associated with the screen based beam size measurements will be discussed in chapter 5.

There are two different types of cameras used in PITZ, analog cameras from JAI and digital cameras from Prosilica. The JAI model used is M10 SX [37], which is equipped with a CCD chip of 1/2" size consisting of 768×574 square pixels. The analog signal output is transmitted to a PC with framegrabber card installed where the signal is encoded into pictures with 8 bit amplitude resolution [37]. The other type is a Prosilica GE/GC 1350 digital camera [38], which comes with a CCD chip 1360×1024 pixels, 4.3 μm pixel size and 12 bit digital resolution of the signal amplitude. In addition the signal readout from neighboring elements in the CCD chip of the Prosilica camera can be combined thus increasing the light sensitivity of the device at the ex-

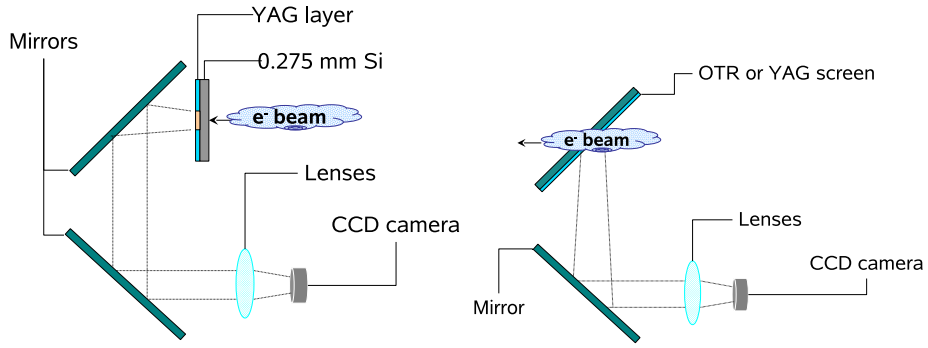

(a) 90^o incidence (b) 45^o incidence

Figure 3.7: Typical screen geometry at PITZ.

pense of decreased spatial resolution (effective size of the CCD chip 765×512 pixels). Both camera types are monochrome. Each of them can be remotely controlled for optimal performance and are externally triggered to match the repetition rate of the accelerator. The cameras are successfully incorporated in the PITZ video system [39].

Another type of transverse diagnostics is the Emittance Measurement System (EMSY) [28, 40]. It is based on the single slit method for measuring the emittance where the beam is sampled at different locations across one of the transverse planes and the divergence is estimated from the rms sizes of these beam samples (beamlets) measured after a drift distance. The EMSY consists of two orthogonal actuators mounted perpendicularly to the longitudinal axis of the beam. The actuators hold YAG and OTR screens as well as single slit masks. Detailed description of the Emittance measurement apparatus will be given in chapter 5. The uncertainties associated with each component included in the emittance measurements such as screens, slits etc. are discussed in the same chapter.

Chapter 4

Beam dynamics in the photo-injector

The beam dynamics in the PITZ photo-injector is dominated by three forces, acceleration, focusing and self repulsion by the space charge. They are all electromagnetic in nature thus described by the Lorentz force equation. Maintaining delicate balance between them is a prerequisite for the production of a beam with a fine quality.

$$F_L = q \cdot (\mathbf{E} + v \times \mathbf{B}) = m_e \frac{dv}{dt}, \tag{4.1}$$

where q is the charge of the particle, $\mathbf{E}$ is the external electric field, v is the velocity of the particle and $\mathbf{B}$ is the external magnetic field.

The Lorentz force F_L describes the action of all the electromagnetic fields on the charged particle where the resulting force represents a superposition of all the external and internal forces. The external forces are typically created by accelerating cavities or magnetic focusing lenses. The internal forces are the combined action of the other electrons from the beam.

Another major influence on the beam quality comes from the charge extraction from the photocathode. The process of charge extraction and the effects associated with it determines the ultimate beam quality. In this chapter a brief introduction to the basics of the beam physics is given together with the theory of the compensation of space-charge and RF induced emittance.

4.1 Phase space and emittance

The position of a particle can be represented by a point described by the three coordinates x, y and z or a vector $\vec{r} = (x,\ y,\ z)$ giving the position of the particle in space. The state of a system that consist of many such particles can be described in any moment in time, given that the momentum components of the particles in the system are also known. In the case of charged particles such as electrons, the canonical momentum is used which can be expressed as $\hat{p}_c = \vec{p} + q\vec{A}$, where $\vec{p} = (p_x,\ p_y,\ p_z)$, q is the particle charge and $\vec{A}$ is the magnetic vector potential. Combining these 6 components we form the so called *phase space* which gives concise knowledge of the state of a particle or ensemble of particles in each particular moment in time. Usually the transverse components of the momentum p_x and p_y are normalized to the longitudinal momentum component p_z. The resulting six dimensional phase space $(x,\ y,\ z,\ x^{'},\ y^{'},\ z^{'})$ is called trace space, where:

$$\begin{aligned} x^{'} &\equiv \frac{dx}{dz} = \frac{p_x}{p_z} \\ y^{'} &\equiv \frac{dy}{dz} = \frac{p_y}{p_z} \\ z^{'} &\equiv \frac{1}{\gamma^2} \cdot \frac{\Delta p}{p_z}. \end{aligned} \tag{4.2}$$

Here p_z is the momentum component in the direction of beam propagation, $\gamma = (1-\beta^2)^{-1/2}$ is the Lorentz factor, $\beta = v/c$ is the normalized particle velocity, c is the speed of light and Δp is the difference between the momenta of the given and the average momentum of the particle ensemble.

An electron bunch of 1 nC consists of about 6.2 billions of electrons distributed in some volume in the trace space. The description of such a vast collection of particles in the trace space can be given by the covariance matrix $\hat{\Sigma}$ (equation 4.3) where the diagonal elements are the second order central moments of the distribution and the off diagonal elements are the covariances between the diagonal elements. The covariance matrix is real and symmetric. Second-order moments give the main statistical characteristics of the given distribution in the 6D trace space and characterize how the electrons are spread around the mean position (for a centered distribution). The emittance of a beam is related to the volume occupied by the particles in this six dimensional

space. Due to large variety of the distributions in the phase space the so called *rms* emittance is used which is the root of the determinant of the covariance matrix or $\varepsilon_{rms}^{6D} = \sqrt[6]{det|\hat{\Sigma}|}$. This is the so called geometric emittance or in other words it is the volume occupied by a distribution with the given central moments. In order to compare emittance of beams with different momentum, the normalized emittance is defined as the product of the rms emittance and the relativistic Lorentz factors $\varepsilon_{n,rms} = \beta\gamma \cdot \varepsilon_{rms}$. In practice the 6D trace space description is usually split into three 2D planes where the distribution is given as a projection $(x,\ x^{'})$, $(y,\ y^{'})$ and $(z,\ z^{'})$ given that no correlation between them is present. Thus, the so called projected emittance is defined which is the area that the particles occupy in these planes. In fact, in the RF gun due to the time dependence of the accelerating field (see equation 3.5) and the finite bunch distribution (fig. 3.3(a)) this condition is violated and there is a correlation between the transverse and longitudinal planes, which can lead to increase of the projection of this distribution in the transverse plane and thus to increase of the projected emittance. Another reason for correlations between different subspaces can be as well inhomogeneities in the laser pulse shape or nonvanishing magnetic flux at the cathode. Nevertheless, the concept of separating the longitudinal from the transverse planes is useful and pays off in reducing the amount of variables in the calculations.

$$\hat{\Sigma}_{6D} = \begin{pmatrix} \sigma_{11} & \cdots & \sigma_{16} \\ \vdots & \ddots & \vdots \\ \sigma_{61} & \cdots & \sigma_{66} \end{pmatrix} \approx \begin{pmatrix} \hat{\sigma}_x & 0 & 0 \\ 0 & \hat{\sigma}_y & 0 \\ 0 & 0 & \hat{\sigma}_z \end{pmatrix} \tag{4.3}$$

here $\hat{\sigma}_i,\ (i = x,\ y,\ z)$ represents the block matrix of a size 2x2 containing the second moments of the particle distribution in the corresponding spatial dimension i.e. for the x plane:

$$\hat{\sigma}_x = \begin{pmatrix} \sigma_x^2 & \sigma_{xx'} \\ \sigma_{xx'} & \sigma_{x'}^2 \end{pmatrix} = \begin{pmatrix} \langle x^2 \rangle & \langle xx^{'} \rangle \\ \langle xx^{'} \rangle & \langle x^{'2} \rangle \end{pmatrix} \tag{4.4}$$

The second central moment of a two dimensional distribution $\rho(x, x^{'})$ [41]

or the mean square is given by equation 4.5.

$$\langle x^2 \rangle = \frac{\int x^2 \rho(x, x^{'}) dx dx^{'}}{\int \rho(x, x^{'}) dx dx^{'}} - \left(\frac{\int x \rho(x, x^{'}) dx dx^{'}}{\int \rho(x, x^{'}) dx dx^{'}} \right)^2 \tag{4.5}$$

In order for equation 4.5 to represent the 2D projection of the 6D trace space the integration in the other four dimensions must also be done.

Following the above statements we can give a definition of the normalized projected rms emittance of the beam as follows

$$\varepsilon_{n,x,rms} = \beta\gamma \cdot \sqrt{\langle x^2 \rangle \langle x'^2 \rangle - \langle x x^{'} \rangle^2} \tag{4.6}$$

The projected normalized transverse emittance is measured in units of $m \cdot rad$ or what is more practical in $mm \cdot mrad$. From now on the notations rms and n will be omitted and if not especially mentioned we will speak only about the projected normalized rms emittance defined in equation 4.6 given as ε_x or ε_y. Since it contains integration in all the other dimensions the area of the projection can increase due to cross-correlations between the different planes while the volume of the distribution in the phase space remains unchanged.

Historically, the emittance is also described as an ellipse whose parameters are determined by the rms values of the distribution function [1]:

$$\beta \sigma_x^{'} + 2\alpha \sigma_{xx'} + \gamma \sigma_x = 1 \tag{4.7}$$

where $\alpha,\ \beta,\ \gamma$ are the so called Twiss parameters and the covariance matrix can be expressed as [1]

$$\hat{\sigma}_x = \begin{pmatrix} \sigma_x^2 & \sigma_{xx'} \\ \sigma_{xx'} & \sigma_{x'}^2 \end{pmatrix} = \varepsilon_x \begin{pmatrix} \beta & -\alpha \\ -\alpha & \gamma \end{pmatrix} \tag{4.8}$$

The emittance is a very important concept for describing the quality of the electron beam and it has important implications for understanding the dynamics of the system. In general it gives an idea on how well contained is the beam dynamically. The most important sources of projected emittance growth in a photo-injector as described in [42] are: linear space charge; nonlinear space charge; nonlinear time-independent RF; and linear time-dependent RF. When the emittance reaches values about or below 1 $mm \cdot mrad$ the contribution from

the initial velocity spread of the electrons becomes significant. That is the so called *thermal emittance*. In the following, a short description of the various sources of emittance growth and procedures for its control will be discussed.

4.2 Production of electrons in the RF gun

4.2.1 Extraction, photo effect and thermal emittance

There are three major sources of electrons in a photocathode RF gun concisely described in [43]. These are electrons due to field emission from the body of the gun cavity, electrons from the photo-electric effect and secondary electrons driven out of the gun and cathode material from the primary electrons. While the first and the last can only contribute to radiation damage of machine components and noise in beam diagnostics, the mechanism which is important from point of view of beam dynamics is the photo effect.

At PITZ the semiconductor Cs_2Te is used as photocathode. In order to produce photo electrons in a semiconductor material the photons must have energy E_{ph} higher than the band gap E_G of the semiconductor. In our case the cathode is illuminated by photons with energy $E_{ph} = h\nu \simeq 4.72\ eV$, Cs_2Te has a band gap of $E_G = 3.3\ eV$. After the energy of a photon is absorbed from an electron located in the cathode material, the electron drifts to some of the maximum of the density states of the conduction band of the semiconductor. In the case of Cs_2Te the first maximum of the density state[1] E_{CB} is located at 4.05 eV [44]. Electron located at this state have energy sufficient to eject it through E_G and the surface potential barrier, the electron affinity E_A. The electron affinity is defined as the energy difference between the vacuum level and the tail of the conduction band density distribution. It was measured that $E_A = 0.2\ eV$. The final mean kinetic energy of the free electrons is then given by $E_k = E_{CB} - E_{vac} = 0.55\ eV$.

Besides the energy absorption of the photon by an electron there are several other effects that are taking place during the illumination of the cathode with photons i.e. reflection, when all of the photon energy is driven back to the vacuum.

[1] the next maximum of electron density in Cs_2Te is at 4.9 eV and is not contributing to the photo effect

All these effects can be summarized as the cathode quantum efficiency (QE) which is simply defined as the number of photo electrons per number of photons or $QE = n_e/n_{ph}$.

Major influence on the above described quantities is caused by the high electric field applied during the photo emission. This can be described with an analogy to the so called Schottky effect which is a lowering of the potential barrier in the presence of an electric field. This leads to increase of the electron escape probability which effectively increases the QE. A counteracting effect is the poisoning of the Cs_2Te surface from residual gases in the vacuum system. These effects were examined in details in [28, 43].

The energy distribution of the photo electrons resulting from the above mentioned description of the photo effect is contained within the thermal emittance ε_{th} under the following definition [44]

$$\varepsilon_{th} = \sigma_{ini}\sqrt{\frac{2E_k}{m_e c^2}}\frac{1}{\sqrt{3}} \tag{4.9}$$

where σ_{ini} is the radius of the laser spot on the cathode, E_k is the kinetic energy after all the effects described above.

This is the lower limit to the emittance from a photo-injector, and the actual emittance of the electron beam is typically higher than the one given by 4.9. The effects leading to increase of the emittance and possible ways to their elimination/compensation will be discussed later in this chapter.

4.2.2 Acceleration and RF focusing

Taking into account Eqs. 3.5, and 4.1 the momentum gain when an accelerating field is applied to an electron at phase ϕ_0 takes the form of equation 4.10 where $\alpha = eE_0/(4\pi f m_e c^2)$ is the normalized vector potential or the so called RF parameter representing the strength of the accelerating field, E_0 is the peak on-axis field and ϕ_0 is the phase with respect to the RF wave at which the electron leaves the cathode:

$$\frac{d\gamma}{dz} = \alpha \cdot \frac{E(z)}{E_0}\sin\left(2\pi f t + \phi_0\right). \tag{4.10}$$

Integrating equation 4.10 with respect to z will reveal the momentum of the particle after the exit from the accelerating region. Since the electrons in the bunch are distributed within a finite length of about 20 ps their momentum will differ from each other depending on the phase between them.

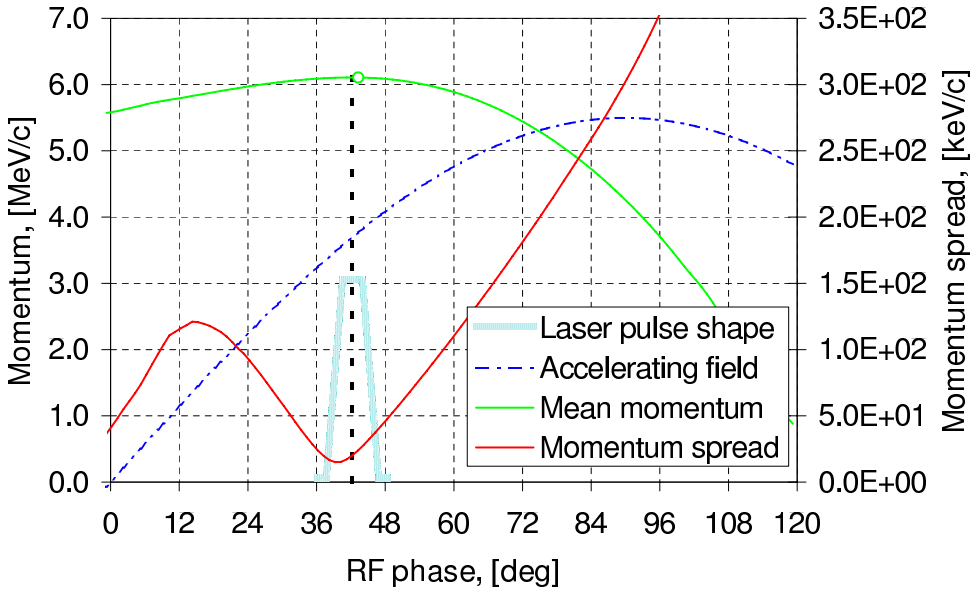

Figure 4.1: Simulation with ASTRA of the bunch acceleration using gradient of 60 MV/m at the cathode. The accelerating field is shown normalized by the maximum bunch momentum.

On figure 4.1 is shown the result from a simulation with ASTRA of the dependence between ϕ_0, the mean momentum and the momentum spread of the bunch. The shape of $E(z)$ is shown on figure 3.5, the laser distribution is the one shown on figure 3.3(a). Of our practical interest is the phase at which the mean momentum of the bunch is in the maximum, in this case this is 42.7°. This is important because it is easy to measure it in practice and establish a reference condition for the photo-injector setup. This phase (of max. mean momentum gain) will always be referred to as the $reference$ phase ϕ_{ref}. Further in the work all the phases are given with respect to ϕ_{ref}.

In addition to the longitudinal acceleration of the electrons due to the RF field, a transverse force from the RF field is also acting on the bunch, resulting in linear and non-linear effects on the phase space distribution [42,45,46]. This force can be summarized using equation 3.5 and the condition $\nabla \cdot \vec{E} = 0$ which

brings us to:

$$E_r = -\frac{r}{2}\frac{\partial E_z}{\partial z}, \tag{4.11}$$

where E_r is expressed in cylindrical coordinates. Equation 4.11 due to the time dependence of the RF field brings the next constraint $\nabla \times \vec{B} = \frac{1}{c^2}\frac{\partial \vec{E}}{\partial t}$ out of which the azimuthal magnetic field can be expressed as:

$$cB_\theta = -\frac{r}{2c}\frac{\partial \vec{E}}{\partial t}, \tag{4.12}$$

equations 4.11 and 4.12 lead us to the radial force expressed as

$$F_r = -e\left(E_r - \beta c \times B_\theta\right) \tag{4.13}$$

This equation shows that a transverse force from the RF cavity is acting upon the electrons in the beam. It can be expressed as average focusing strength or:

$$K_r = -\frac{F_r}{r\gamma\beta^2 mc^2}, \tag{4.14}$$

which gives the so called ponderomotive RF focusing force [46].

Since the electrons have finite longitudinal distribution with respect to the RF wave (see figures 3.3(a) and 4.1) the effect on different longitudinal slices along the beam will result in correlation between the longitudinal coordinate and the angular momentum spread which leads to increase of the projected beam emittance. Using equation 4.13 and integrating the distribution in $\langle x^2 \rangle$ and $\langle x'^2 \rangle$, an estimate on the contribution of the RF acceleration and focusing to the projected emittance can be made. In the case of a uniform cylindrical distribution, it is of the form given by [45]:

$$\varepsilon_x^{RF} = \frac{\alpha 2\pi^3 a^2 L^2}{\lambda_{RF}^3 \sqrt{6!}}, \tag{4.15}$$

where a is the initial beam radius, L is the length of the bunch and λ_{RF} is the RF wavelength.

The increased projected emittance due to the varying RF field is due to the finite length of the bunch with respect to the variation of the RF field. It can be minimized by choosing proper launching phase and/or decreasing the

length of the electron bunch. The later, however, can lead to increase of the undesired effects due to the space charge field of the bunch.

4.2.3 Space charge influence

A distribution of charged particles such as electrons, provides an electromagnetic field that is acting as a repulsive force on each of the particles.

The electromagnetic force acting on an electron due to the electric field of the rest of the electrons in the bunch can be expressed as follows [45]:

$$F_x^{sc} = \frac{e}{\gamma^2} E_x^{sc}, \tag{4.16}$$

where E_x^{sc} is the x component of the electrostatic field $\vec{E}^{sc} = (E_x^{sc}, E_y^{sc}, E_z^{sc})$ due to the given charge distribution. Assuming that the beam has a cylindrical symmetry the y component of the force is of the same form.

Due to the fact that the space charge forces are decreasing with $1/\gamma^2$, the most important region for mitigating its effect is during the extraction and initial acceleration of the electrons. We can use the relation:

$$\frac{d\gamma}{dz} \simeq \frac{eE_0}{mc^2} sin(\phi_0) \tag{4.17}$$

and apply integration over the space charge distribution $\rho(x, y, z)$ with respect to dz to obtain an expression for the momentum components at the final stage of acceleration [45]

$$\vec{p} = \frac{1}{E_0 sin(\phi_0)} \frac{\pi}{2} \vec{E}^{sc} \tag{4.18}$$

here $\vec{E}^{sc}(x, y, \Delta z) = \frac{n_0}{4\pi\epsilon_0} \xi(x, y, \Delta z)$ is the electrostatic field of the bunch where ξ is the normalized field, $n_0 = \int \rho(x, y, 0) dx dy$ the line charge density in the center of the bunch and ϵ_0 the permittivity of free space.

Using this expression one can estimate the contribution of the space charge to the projected emittance as follows [45]:

$$\varepsilon_{n,x}^{sc} = \frac{\pi}{4} \frac{1}{\alpha k} \frac{1}{sin(\phi_0)} \frac{I}{I_0} \mu_x(A). \tag{4.19}$$

Here μ_x is a dimensionles form factor corresponding to the distribution function of the electrons in the trace space

$$\mu_x = \sqrt{\langle \xi_x^2 \rangle \langle x^2 \rangle - \langle \xi_x x \rangle^2}$$

and A is the bunch aspect ratio defined as $A = R/L$ where R is the transverse diameter of the bunch and L is the length.

The influence of the space charge can be summarized as a defocusing lense acting differently along the bunch.

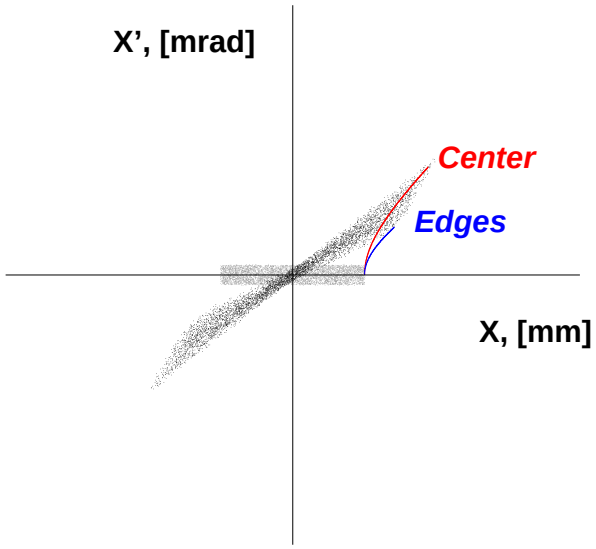

Figure 4.2: The effect of linear the space charge on the transverse phase space of a bunch with finite length z_{max}, gray is the initial uniform charge distribution with small divergence and dark is its evolution in free space. The trajectories of two reference particles are shown, red line represents particles located at ($x = x_{max},\ z = 0$), blue at ($x = x_{max},\ z = \pm z_{max}$).

4.2.4 Linear space charge compensation

Because the radial space charge forces are stronger in the central longitudinal slice of the bunch than in the head/tail regions, the angle between $(x^{'}, x)$ in the phase space becomes a function of the longitudinal displacement with respect

to the center of mass of the bunch $\varphi(\Delta z)$.

$$\varphi = arctan\left(\frac{x^{'}}{x}\right) \tag{4.20}$$

This correlation leads to an increase of the projected emittance as shown in figure 4.2. Therefore, different longitudinal slices of the beam receive different kick in the angular spread of the phase space resulting in a fan like structure (figure 4.2).

It has been shown in [42] that the linear part of the space charge emittance growth can be compensated by applying another linear force that counteracts the defocusing force from the space charge. This is achieved using a solenoid lens with focusing strength matching the defocusing force of the space charge.

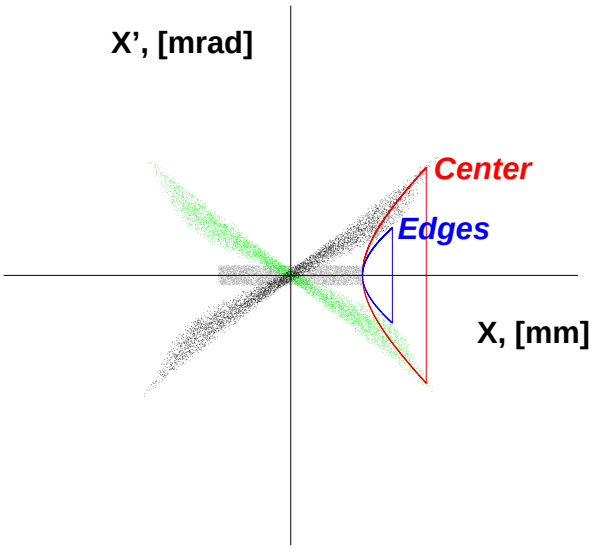

Figure 4.3: The phase space distribution from figure 4.2 immediately after the solenoid (green), after a drift in the empty space (dark) and inbetween with a compensated space charge (gray). The trajectories of two reference particles are shown, red line represents particle located at ($x = x_{max}$, $z = 0$), blue at ($x = x_{max}$, $z = \pm z_{max}$).

Under the assumptions that the beam is already relativistic, the electric

field has only radial components, the solenoid field is acting as a thin lense, the longitudinal slices do not mix and the beam has no spread in the longitudinal velocities we can use two representative slices of the bunch called here *center* (c) and *edge* (e) to describe the process of compensation. They are characterized by their angle of rotation in the phase space $(x, x^{'})$ or φ_c and φ_e. After a thin solenoid lense of focal length $1/f_s$, the dark distribution on figure 4.2 is transformed to the green distribution on figure 4.3. Due to the variation of the space charge forces along the bunch, the central slice orientation in phase space $\varphi_c = \varphi(\Delta z = 0)$ (equation 4.20) changes faster than the edge slices. At certain moment in time, the angle between the central slice and the others will be equalized. In the simplified model, illustrated on figures 4.2 and 4.3, this will correspond to $\varphi_c \equiv \varphi_e$ and a complete recovery of the initial phase space distribution (gray distribution on figure 4.3).

In practice due to nonlinearities of the space charge field, nonlinear effects caused by the RF field etc., this condition can not be fully achieved. In addition to that different longitudinal slices will travel with different phase in the RF wave, resulting and in different RF focusing and momentum spread which are also not considered in this simple model.

If all these effects are included, parts of the beam (mainly located in the head and tail regions) will have widely different distribution of the divergence angles, thus appearing as a *halo* in the transverse projections (x, y), (x, x') and (y, y'). Such a halo brings large contribution to the projected *rms* emittance of the whole bunch despite the fact that the halo itself has very small fraction of the charge. In many cases it is practical to define a value for the projected emittance that include smaller fraction of the bunch charge. This quantity is defined as the rms area included in a equidensity contour containing the corresponding fraction of the charge [47]. As typical value 90 % from the charge is accepted. In some cases the term *core emittance* is used, for a detailed description of the core emittance concept see chapter 7.

The solenoid compensation scheme was experimentally studied at PITZ and the results were compared with the theoretical models [28].

4.2.5 Invariant envelope

In order to avoid further emittance growth downstream the optimum point discussed above or due to nonlinearities in the space charge distribution, additional acceleration must be applied so that the space charge forces are canceled. To obtain the minimum emittance at the injector exit one needs to properly match the beam to the accelerating module of the photo-injector, which means that the beam must be propagated in the so called *invariant envelope* regime described in [11, 48, 49].

The rms envelope equation [49] in the paraxial approximation describes a cylindrical symmetric distribution propagating under the effect of acceleration, external focusing from RF and solenoid fields and the defocusing force of the space charge.

$$\sigma^{''} + \sigma^{'}\frac{\gamma^{'}}{\gamma} + \sigma\frac{\Omega^2\gamma^{'2}}{\gamma^2} = \frac{\kappa_s}{\sigma\gamma^3} + \frac{\varepsilon_n^2}{\sigma^3\gamma^2}, \tag{4.21}$$

where σ is the rms beam envelope, the dashes over σ denote derivatives with respect to the direction of propagation (d/dz), $\gamma^{'} = \frac{eE_{acc}}{m_e c^2}$ is the normalized accelerating gradient, E_{acc} is the accelerating field, γ is the Lorentz factor, Ω is the normalized focusing gradient, $\kappa_s = I_p/(2I_A)$ is the beam perveance, I_p is the beam peak current and I_A is the Alfven current.

A bunched beam is represented as axially distributed slices, where the external focusing and the defocusing from the space charge of each slice depends on the position of the slice along the bunch. Using the same assumptions as in the previous subsection, an equation of the form of 4.21 can be used for each longitudinal slice of the bunch.

The propagation of an electron beam is called *space-charge dominated* when the repulsive space charge forces (the first term on the right hand side in equation 4.21) are much greater than the emittance defocusing term (the second term on the right hand side in 4.21). The ratio between those two terms is called the laminarity parameter [49]:

$$\Xi = \frac{I_p \cdot \sigma^2}{2\gamma I_A \varepsilon_n^2}, \tag{4.22}$$

where σ is the rms beam size, ε_n is the normalized rms emittance, γ is the normalized beam kinetic energy, I_p is the peak current of the beam and I_A is

the Alfven current. When Ξ is much greater than 1 the beam propagates in a quasi laminar or space-charge dominated regime.

Detailed theoretical analysis of equation 4.21 under various initial conditions was performed in [11,48], and it is shown that when the beam is propagating in a space-charge dominated regime, mismatches between the defocusing space charge forces and the external focusing fields (such as RF and solenoid) are causing envelope oscillations with amplitude that depends on the longitudinal position in the bunch. Such oscillations are causing growth in the projected normalized emittance. One possible way to damp this growth is by acceleration of the beam or increase of γ until transition from space-charge to emittance dominated beam occurs where $\Xi \ll 1$.

If the beam is properly matched to the accelerating structure the low emittance beam at the exit of the photo-injector can be transported much further downstream under the conditions of the *emittance conservation*. One direct consequence of this theory is that the photo-injector should deliver emittance dominated beams with $\Xi \ll 1$.

An exact analytical solution of the envelope equation 4.21 called *invariant envelope* is given by [49]:

$$\sigma_{ie} = \frac{1}{\gamma'}\sqrt{\frac{2I}{I_A(1+4\Omega^2)\gamma}}, \tag{4.23}$$

where γ is the normalized kinetic energy, $\gamma^{'}$ is the normalized accelerating gradient. The normalized focusing gradient is expressed as Ω which includes the RF ponderomotive focusing force and the focusing due to the magnetic field of a solenoid. Considering B_z as the magnetic field amplitude on axis of the main solenoid and standing wave accelerating structures, Ω takes the form [49]

$$\Omega^2 = \left(\frac{eB_z}{mc\gamma'}\right)^2 + \frac{1}{8} \tag{4.24}$$

An important property of the invariant envelope is that the trace space angle is independent of the slice perveance thus invariant for all longitudinal positions along the beam [50], or

$$\frac{\sigma_{ie}^{'}}{\sigma_{ie}} = -\frac{\gamma^{'}}{2\gamma}.$$

That corresponds to a generalized Brillouin flow condition or the particles in the beam of cylindrical shape are rotating along the axis of movement with the same forward velocity[2] i.e. the slices do not mix.

Following the above mentioned analysis a matching condition between the beam rms size at the waist σ_w, the peak current I_p, incoming mean momentum and the energy gain in the booster is derived in [51]:

$$\gamma'_{booster} = \frac{2}{\sigma_w}\sqrt{\frac{I_p}{3I_A\gamma}}, \tag{4.25}$$

In the case of the PITZ photo-injector setup, consisting of RF gun, solenoid, a drift and a booster cavity, the emittance evolution downstream the cathode shows a characteristic double minimum in the region of the beam waist without further acceleration with the booster cavity. The reason for this double minimum is the slight differences in the momentum of the particles in the head and the tail of the bunch, meaning that the rotation angle in the phase space will be dependent not only on the bunch charge distribution but also on the RF phase for each particular slice. With increasing of the focusing strength of the solenoid these minima tend to come closer to each other and eventually merge (see figure 4.4(a)).

On figure 4.4 results from ASTRA simulations are shown for the following conditions: maximum accelerating gradient at the gun cavity 60.0 MV/m, uniform transverse distribution of the cathode laser with rms size 0.48 mm, flat-top longitudinal distribution - FHWM=20 ps and rise/fall time of 2 ps, RF phases of the gun and the booster are at maximum mean momentum gain. On figure 4.4(a) the emittance evolution was simulated without additional acceleration applied while on figure 4.4(b) a 14 cell booster cavity of the Cut Disk Structure (CDS) type [32] is placed at 2.96 m downstream the cathode (the first iris position), the final beam mean momentum is 26.5 MeV/c. Figures 4.4(c) and 4.4(d)) show the beam size with a contour representing the *invariant envelope* trajectory in the I_{main}/z plane. It can be seen that under this conditions the IE is conserved only about a meter after the booster cavity at $I_{main} = 380$ A. In order to conserve it further downstream additional

[2]this condition is obtained with balance between the focusing force Ω and the repulsing space charge forces described earlier

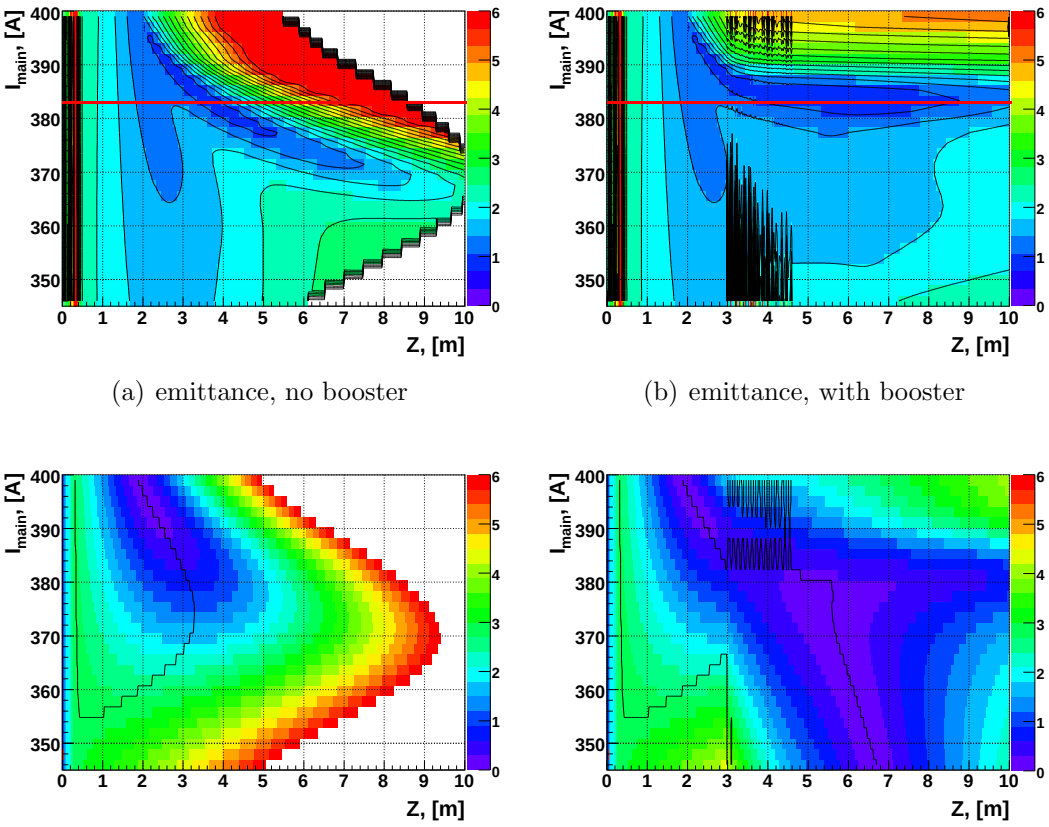

(a) emittance, no booster

(b) emittance, with booster

(c) beam size, no booster

(d) beam size, with booster

Figure 4.4: ASTRA simulation of the emittance (color code in units $mm\ mrad$) and the transverse rms beam size (color code in mm) in the photo-injector. Initial rms size is 0.48 mm, minimum emittance obtained with further acceleration is 0.79 $mm \cdot mrad$ at 6.29 m downstream the cathode and $I_{main} = 383\ A$. With thin red lines the profiles with minimum of the emittance were selected and shown on figure 4.5.

acceleration must be applied.

A cross section from this planes is taken at position of the solenoid current corresponding to the minimum emittance (marked with red lines on figures 4.4(a) and 4.4(b)). The result is shown on figure 4.5 with grey color the location of the booster cavity is displayed, the red lines are plotting the emittance evolution along the z axis, and in blue dotted lines the rms size as a function of the distance to the cathode.

In order to satisfy the invariant envelope matching condition demonstrated in [52], the first cell of the booster is placed at the location of the local maximum between the two characteristic minima exactly at the beam waist. As

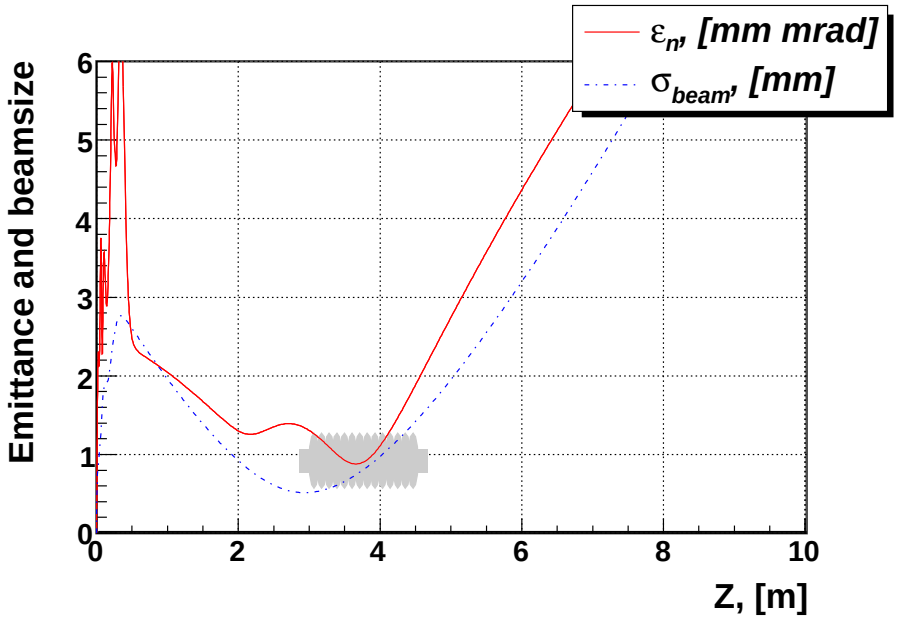

(a) $\varepsilon(z)$, $I_{main} = 383\ A$, no booster

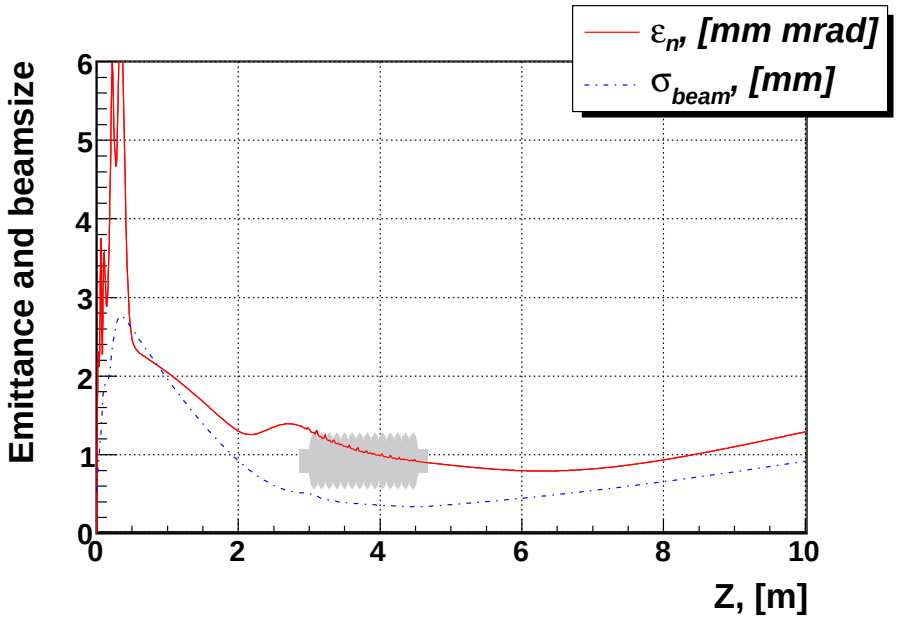

(b) $\varepsilon(z)$, $I_{main} = 383\ A$, with booster

Figure 4.5: ASTRA simulation of the emittance as a function of the distance to the cathode. Initial rms size is 0.48 mm, $I_{main} = 383\ A$, the minimum emittance of 0.79 $mm \cdot mrad$ is obtained with booster and is located at 6.29 m downstream the cathode. With gray the disposition of the CDS booster is shown.

it can be seen on 4.5(b), the second emittance minimum is stretched from

$z = 3.65\ m$ to $z = 6.29\ m$, resulting in a substantial lowering the emittance in the whole examined range up to 10 m. The beam is still largely dominated by the space charge, therefore the emittance is conserved only up to 6-7 m.

4.2.6 Summary

As described above, the production of electrons in the RF gun goes through several stages all of which contribute to the emittance budget of 0.9 $mm \cdot mrad$. These are: thermal emittance from the extraction process; RF induced emittance growth due to correlations induced by the time dependence of the accelerating force and nonlinear forces from the higher order space harmonics in the cavity; emittance growth due to linear and nonlinear space charge forces. Except the latter, all other contributions can be weakened by decreasing the dimensions of the bunch. However all but one - the thermal emittance - are inducing correlations in the beam distribution which can be corrected by some means i.e. solenoid compensation for the space charge or by selecting proper launching phase for the RF wave. This implies that the design of a photo-injector should go through detailed optimization of the driving parameters such as gun cavity inner geometry, RF frequency and gradient, solenoid position and strength, and the dimensions and distribution of the photocathode laser spot. Afterward a careful optimization of the position and the gradient of the next accelerating structures must be made in order to provide quality beam to the linac.

Chapter 5

Emittance measurement setup

In this chapter, a description of various methods for emittance measurements is briefly given. The method of preference is described in details together with thorough analysis of the systematic deviations and uncertainties associated with each component of the measurement setup. Optimization of the method is made for the expected beam parameters at 1 nC charge per bunch. Detailed estimation on the performance of this method for different bunch charge is made in chapter 8.

5.1 Measurement methods

5.1.1 Linear transport methods

To measure the projected normalized emittance, following the definition in 4.6, one needs information on all the components of the covariance matrix (equation 4.3). Whereas, many direct measurement methods exist for the rms spread of the beam distribution σ_x, the other components of the covariance matrix σ'_x and σ'_{xx} can be determined by measuring the beam size under various transport conditions given that the transport matrix is well defined and understood. If the beam matrix at the initial location is $\hat{\sigma}^i_x$, the matrix at some other point can be represented by

$$\hat{\sigma}^f_x = R \cdot \hat{\sigma}^i_x \cdot R^T, \tag{5.1}$$

where

$$R = \begin{pmatrix} R_{11} & R_{12} \\ R_{21} & R_{22} \end{pmatrix}$$

is the transport matrix that can be a product of the matrices of various components from the beam path and R^T is the transpose of matrix R. Since σ_x is measured directly we can express the equation 5.1 in the form

$$\sigma_{11}^f = R_{11}^2\sigma_{11}^i + 2R_{11}R_{12}\sigma_{12}^i + R_{12}^2\sigma_{22}^i$$

The three unknowns in this equation, σ_{11}^i, σ_{12}^i and σ_{22}^i, can be derived when varying the transport matrix and measuring σ_{11}^f for the given conditions and further solving the resulting system of equations. Usually the data from the beam size measurements is subject to a least-squares analysis where the unknown terms of the equation are derived.

Multiple screen method

One example of linear transport method is the multiple screen method, where the beam size is measured on several screens separated by known drift lengths. The transport matrix of a drift space of a length L_d is

$$R_{L_d} = \begin{pmatrix} 1 & L_d \\ 0 & 1 \end{pmatrix}. \tag{5.2}$$

The resulting system of transport equation is of the form

$$\sigma_{11}^1 = \sigma_{11}^i + 2L_{d^1}\sigma_{12}^i + L_{d^1}^2\sigma_{22}^i$$

$$\vdots$$

$$\sigma_{11}^n = \sigma_{11}^i + 2L_{d^n}\sigma_{12}^i + L_{d^n}^2\sigma_{22}^i$$

where the index n in L_{d^n} gives the corresponding n'th drift length. The derivation of σ_{11}^i, σ_{12}^i and σ_{22}^i is afterwards straightforward.

Quadrupole scan

Another similar approach is to use a single screen but change the $\hat{\sigma}$ with the help of a quadrupole lens [53]. Anderson et al. did very thorough analysis of this method in [54]. The transport matrix for focusing Q_F and defocusing Q_D quadrupole is of the form

$$\begin{aligned} Q_F &= \begin{pmatrix} cos(\sqrt{k}L_q) & \frac{sin(\sqrt{k}L_q)}{\sqrt{k}} \\ -\sqrt{k}sin(\sqrt{k}L_q) & cos(\sqrt{k}L_q) \end{pmatrix} \\ Q_D &= \begin{pmatrix} cosh(\sqrt{k}L_q) & \frac{sinh(\sqrt{k}L_q)}{\sqrt{k}} \\ -\sqrt{k}sinh(\sqrt{k}L_q) & cosh(\sqrt{k}L_q) \end{pmatrix} \end{aligned} \tag{5.3}$$

Here k is the focusing strength and L_q is the effective length of the quadrupole. Important to note is that when the quadrupole is focusing in one of the planes, it is defocusing in the other. The $4D$ transport matrix of a quadrupole R_Q is formed by both of them such that if the focusing is in the x plane, the matrix is of the form

$$R_Q = \begin{pmatrix} Q_F & 0 \\ 0 & Q_D \end{pmatrix}.$$

By analogy with the multiple screen method, the same fit procedure is performed using system of equations of the form 5.1.

However, the propagation of the beam in the photo-injector is often dominated by the defocusing strength of the space charge. Appropriate criteria for characterization of the evolution of the beam are given by the laminarity parameter Ξ (equation 4.22), also called the space charge over emittance ratio, used to summarize the evolution in a drift free of acceleration or external focusing elements. Typical values in the PITZ working range, are $\sigma = 0.2 \ldots 1\ mm$, $I_p = 50\ A$, $\gamma = 10 \ldots 60$. If the beam emittance is $\varepsilon_n = 1\ mm \cdot mrad$ then the beam is strongly space charge dominated (see figure 5.1) with values Ξ ranging from 150 at $\gamma = 10$ to slightly less than 1, at $\gamma = 60$ and $\sigma = 0.2\ mm$. The increase of Ξ with the increase of the beamsize can be understood analyzing equation 4.22 and taking into account that the emittance is fixed.

It is obvious that the influence of the space charge forces must be included into the fit since the beam propagation will be influenced by the space charge. Thus the emittance measurement using the methods described above, should

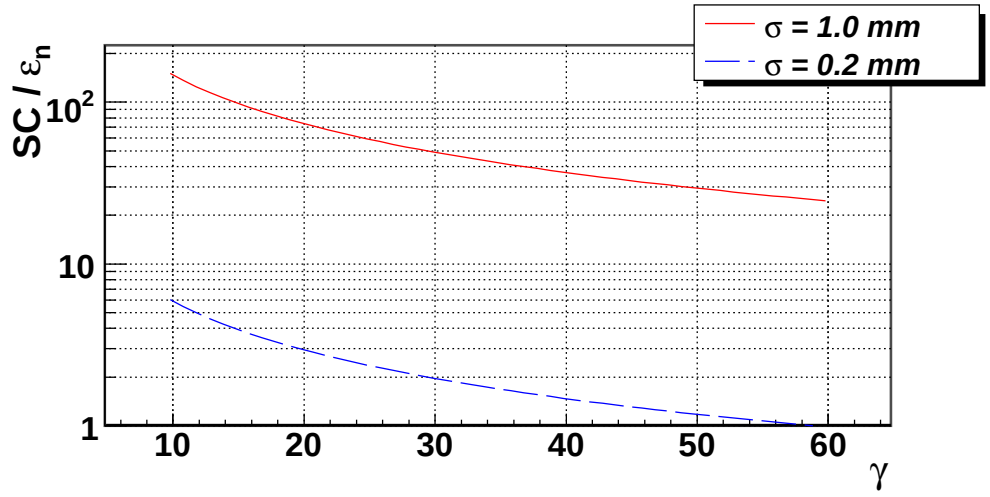

Figure 5.1: Space charge over emittance ratio, $\varepsilon_n = 1.0\ mm \cdot mrad$, $I_p = 50\ A$.

be in parallel with perveance measurement or these methods can not be applied in the PITZ parameter space.

5.1.2 Direct measurement of the angular spread

Another type of diagnostics, called the single slit method (SSM), is able to perform accurate measurements of the emittance of space charge dominated beams. The basic idea of this method is to produce emittance dominated beamlets by cutting tiny fractions out of the space-charge dominated beam [53, 55]. This is achieved by inserting an aperture with slit-like shape, where for measurement in the horizontal plane the slit orientation is vertical and vice versa.

Single slit method

The spread of this beamlet on a screen after a proper drift length L_d corresponds to the local divergence of the beam (see figure 5.2). Figure 5.2 shows a simplified scheme of the principle behind the SSM.

The local divergence $\sqrt{\langle x'^2 \rangle_i}$ at the slit position is given by the relation

$$\langle x'^2 \rangle_i = \frac{\langle x^2 \rangle_b^i}{L_d^2}, \tag{5.4}$$

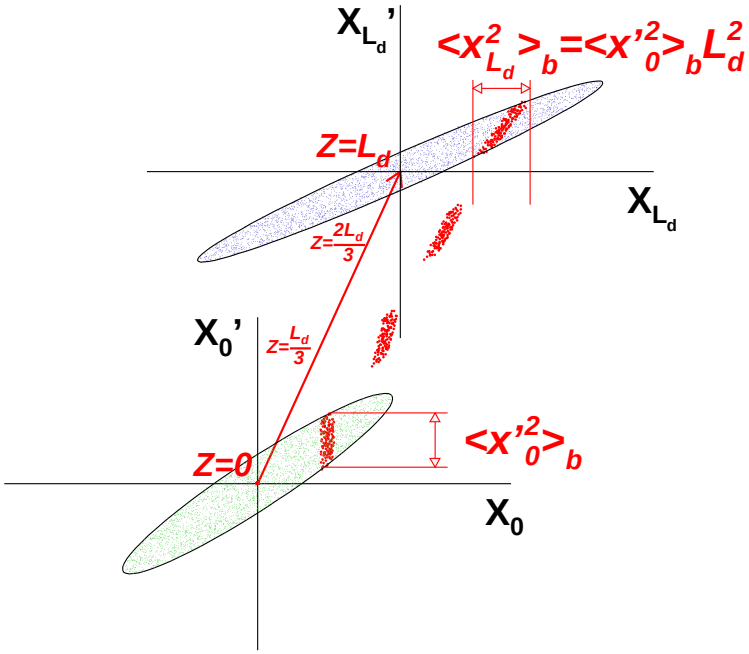

Figure 5.2: Simplified scheme of the slit method. The green ellipse represents the initial beam distribution, the blue ellipse is the same distribution propagated after a drift of a length L_d, with red is shown the fraction from the initial distribution selected from a slit, propagated at distances of 0, $\frac{1}{3}L_d$, $\frac{2}{3}L_d$ and L_d, the direction of beam propagation is shown with thick red arrow.

where $\sigma_b^i = \sqrt{\langle x^2 \rangle_b^i}$ is the beamlet rms size, the index i is related to the position of the slit across the beam transverse distribution and L_d is the distance between the slit and the beamlet observational screen. The initial beamlet size due to the finite slit opening is neglected here, it will be discussed later in this chapter.

Scanning of the beam local divergence across the examined transverse plane can provide information on the sheared divergence of the whole beam by taking the weighted average of the available sheared divergence measurements

$$\langle x'^2 \rangle_s = \sum_{i=0}^{N} w_i \langle x'^2 \rangle_i = \frac{1}{L_d^2} \sum_{i=0}^{N} w_i \langle x^2 \rangle_b^i. \tag{5.5}$$

Here N is the number of divergence measurements taken, w_i is the *weight* of the i^{th} measurement $\sum_{i=0}^{N} w_i = 1$ (i.e. related to the charge of the i^{th} beamlet).

Assuming linear correlation between the position and the momentum in the transverse plane (x, x') the emittance can be expressed simply as the product between the beam rms size $\sqrt{\langle x^2 \rangle}$ and the sheared rms divergence $\sqrt{\langle x'^2 \rangle_s}$ or for the normalized emittance we can write:

$$\varepsilon_{n,rms} = \beta\gamma\sqrt{\langle x^2 \rangle \langle x'^2 \rangle_s}, \tag{5.6}$$

where the rms beam size $\sqrt{\langle x^2 \rangle}$ is measured directly at the position of the slit using YAG or OTR screen and a CCD camera.

Further by performing a scan transversely across the beam, the SSM allows reconstruction of the complete trace space distribution out of which the covariance $\langle xx' \rangle$ and the correlated divergence $\langle x'^2 \rangle$ can be calculated. The trace space distribution is reconstructed by mapping a projection of the beamlet image on the measured axis, to the particular position of the slit across the beam.

In this sense the correlated divergence becomes

$$\langle x'^2 \rangle = \frac{1}{W} \sum_{i,j=1}^{N,m} (\hat{x'} - w_{i,j} x'_j)^2, \tag{5.7}$$

where $\hat{x'}$ is the centroid of the distribution in x' - the divergence axis, N is again the number of divergence/beamlets measurements, m is the number of pixels on the beamlet observational screen, $w_{i,j} = \sum_{k=1}^{l} w_{j,k}$ is the projection of the charge intensity distribution on the divergence axis, $x'_j = j \cdot sL_d^{-1}$ is the divergence coordinate at the beamlet observational screen, j is the pixel location and s is the calibration factor of that screen. In other words the pixel (i, j) is representing an elementary unit area of the measured phase space (x, x').

The covariance term is calculated as

$$\langle xx' \rangle = \frac{1}{W} \sum_{i,j=1}^{N,m} w_{i,j} x_i x'_j - \frac{1}{W^2} \sum_{i,j=1}^{N,m} w_{i,j} x_i \sum_{i,j=1}^{N,m} w_{i,j} x'_j, \tag{5.8}$$

where N is again the number of divergence/beamlets measurements, x_i are

the positions of the slit with respect to the beam center of gravity, $w_{i,j}$ is the intensity value of the pixel (i, j) in the trace space.

The single slit method is a direct measurement of the trace-space distribution of the electrons and provides better accuracy for emittance measurement in the space-charge dominated regime, compared to methods relaying on linear transport matrices.

More details on how the images are processed to extract the useful information are given in Appendix A.

5.2 Design optimization of the emittance measurement system

The first Emittance Measurement SYstem (EMSY) used at PITZ was designed and manufactured jointly by DESY and the Institute for Nuclear Research and Nuclear Energy (INRNE Sofia) in the period 2000-2001 [56,57]. It was successfully commissioned in 2003 and numerous measurements were taken [28,58–60]. The emittance measurement system is based on the SSM (see section 5.1.2), where a space charge dominated beam is collimated by a slit mask and most of the charge is absorbed or scattered in the slit material. The local divergence of the beam is thus estimated when measuring the beamlet at some distance L_d downstream the slit (see figure 5.2). The information on the rms divergence is than estimated when scanning the local divergence at different positions across the beam.

A major upgrade of the PITZ photo-injector and its diagnostics was initiated in 2005 and is still ongoing [14, 26, 31, 61, 62]. This upgrade consists of installation of a 10 MW multibeam klystron for increase of the maximum power available for the gun cavity, improved laser distribution on the cathode (see figure 3.3), installation of a 9 cell booster cavity[1], improved and extended beam diagnostic, etc.

The increase of the peak power in the gun cavity results in higher accelerating gradient (see Eqs. 3.3 and 3.4). Together with the improved laser distribution this results in reduction of the beam emittance caused by the

[1] see section 3.3.4

space charge forces. The CDS booster cavity installation will increase the total beam momentum up to 30 MeV/c. As a consequence of the increased peak current, beam energy and the improved emittance of the photo-injector after the upgrade, the existing EMSY needed to be optimized for best performance with the new beam conditions.

5.2.1 Layout of EMSY

The technical realization of the new system follows the design made in 2001 with the only substantial change in the layout of the screen and slit holders. This design was following closely the considerations given in [55, 56, 63], explained on page 54. The layout of the EMSY is shown on figure 5.3. The components of the system can be described as follows:

- Two motor-driven orthogonal actuators (see figure 5.4), perpendicular to the beam axis are holding the components which intercept the beam:
  - YAG and OTR screens to measure the beam distribution on the exact longitudinal position, where the beamlets are produced
  - single slit masks to produce emittance dominated beamlets
  - multi slit masks
- Stepper motors to move the four axes in order to set and correct the actuator's position or orientation
  - linear motion for precise transverse positioning of the screens and slit masks
  - rotational and goniometric stages for optimization of the angular acceptance of the slits
- Motion controller to steer the insertion of the actuators and the slit orientation
- A screen placed at optimized position downstream the slit masks
- CCD camera and auxiliary structures such as frame-grabber, lenses and light transportation system for observation of the screens at the slit position and downstream at the beamlet measurement screen.

- Software for data acquisition, data analysis and automation of the emittance measurements

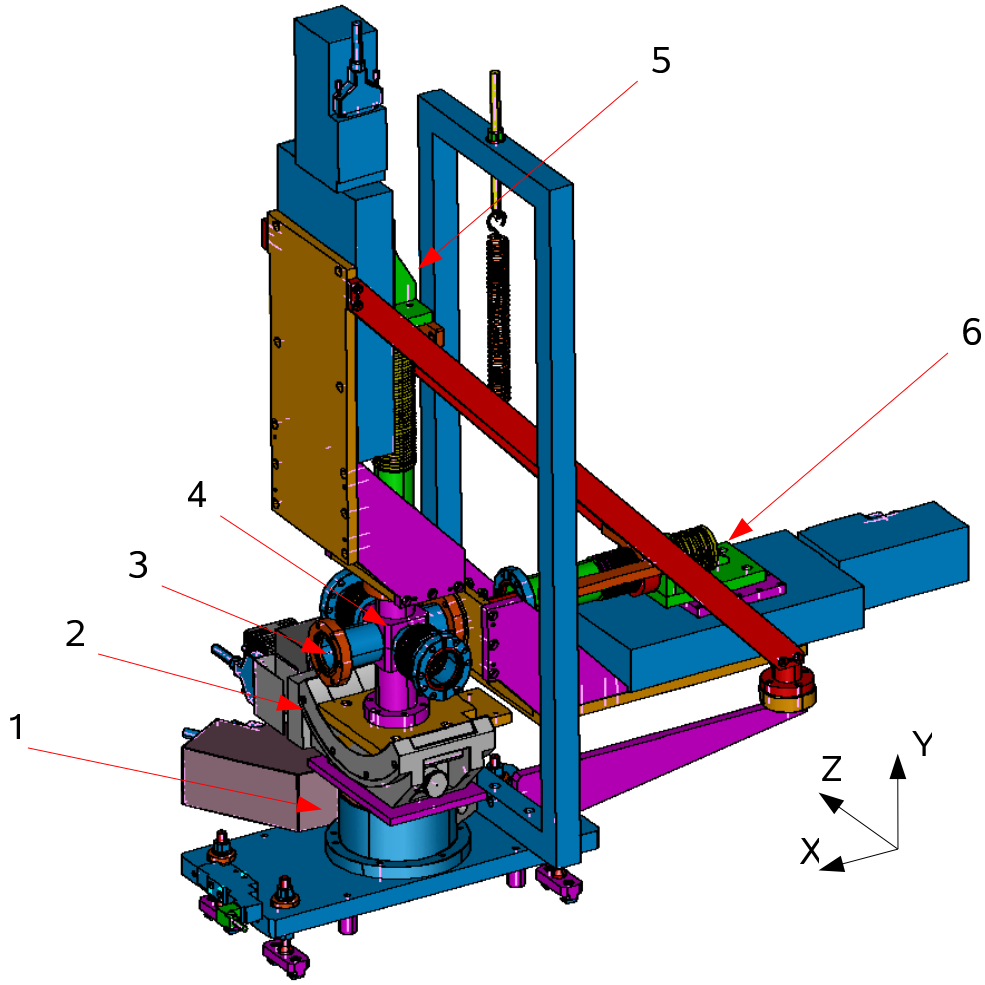

Figure 5.3: Layout of EMSY. 1 - rotation stage of type Newport RV120-PP for adjustment of the angular acceptance of the slit mounted on the horizontal actuator; 2 - goniometric stage of type Newport BGM120-PE for adjustment of the angular acceptance of the slit mounted on the vertical actuator; 3 - viewport for observation and acquisition of the beam images; 4 - vacuum chamber where the beam is intercepted by the screens and slits; 5 - vertical linear stage of type Newport MM100-PP1 with actuator; 6 - horizontal linear stage of the same type with actuator;

On figure 5.4 the layout of the slit and screen holders is shown. A detailed description of the system can be found in [57].

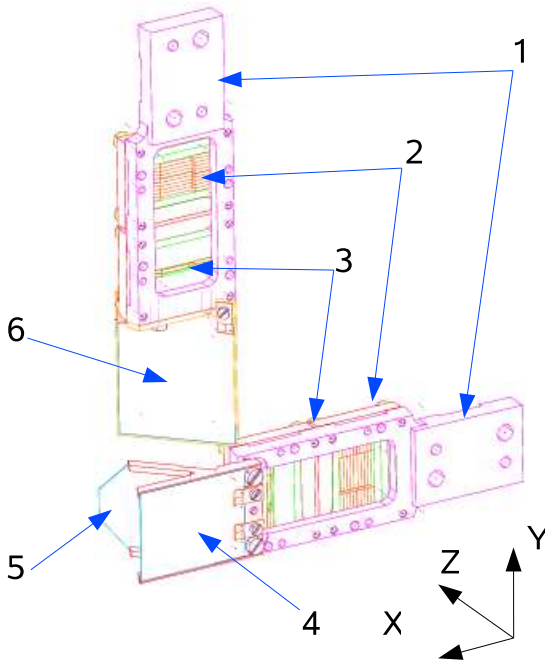

Figure 5.4: Layout of screen and slit holders of EMSY. 1 - stainless steel holders; 2 - multi-slit masks; 3-single slit masks; 4 - YAG powder screen (coated on the back side) with 90° coincidence angle; 5 - mirror for directing the light out of the beam pipe; 6 - OTR screen with 45° coincidence angle.

5.2.2 Physics considerations

To optimize the system for the new working range the following requirements were taken into account [55, 56]:

- The contribution of the initial beamlet size to the one measured at the beamlet observation screen must be as small as possible. Given the appropriate slit opening this can only be controlled by increasing the distance between the slit and the beamlet observational screen.
- The beamlets produced by the slit mask must be emittance and not space charge dominated. This implies the choice of proper slit opening and distance between the slit and beamlet observational screen.
- The distance between the slit mask and the screen must be big enough to resolve small beam divergence, but also must be small enough to minimize the degrading influence due to the remaining space-charge forces.
- The mask thickness must be large enough to scatter the electrons not

passing through the slit in order to produce an uniform background for the beamlets measurements and still it must provide an adequate acceptance angle.

These requirements can be generalized as optimization of the beamlet transport including minimization of the space-charge forces, divergence angle etc., and the mitigation of the technical challenges such as machining of the slits, alignment of the system and optical resolution.

Influence of the finite slit opening

The contribution of the initial beamlet size to the final beamlet size due to the finite slit opening can be described taking into account equation 5.2. This effect can lead to systematic increase of the measured beamlet size, in case where its contribution becomes dominating, it can be subtracted for better accuracy of the divergence measurement.

The rms spread $\sigma_x = \sqrt{\langle x^2 \rangle}$ for a uniform distribution created by a vertical slit with opening d is $\sigma_x = d/\sqrt{12}$. The evolution of the beamlet size is expressed as

$$\sigma_{b,L_d} = \sqrt{\left(\frac{d}{\sqrt{12}}\right)^2 + L_d^2 \cdot \sigma_x'^2}, \tag{5.9}$$

where d is the slit opening, σ_{b,L_d} is the beamlet size after a drift of a length L_d. This implies that the contribution of d is minimized with the increase of L_d. A simple relation can be derived stating that $L_d \gg d/(\sigma_x'\sqrt{12})$. If we consider the extreme case in PITZ, i.e. normalized emittance of 0.9 $mm{\cdot}mrad$, rms beam size of 0.5 mm and beam energy 30 MeV/c, the beam divergence will be $\sigma_x' \sim 0.03$ $mrad$. This means the distance between the slit mask and the screen of observation must be significantly bigger than 47 cm for a slit opening of 50 μm or 9 cm if the slit is 10 μm. However the beamlet size so close to the slit mask can be very small which poses difficulty for the beamlet size measurement system. Therefore one must consider placing the beamlet observational screen further downstream. Transporting the beamlet longer will increase the influence of the space charge forces on the beamlet size.

Below a detailed treatment of both these effects is given. First, the space charge effect is carefully examined to obtain the distance between the slit mask and the screen, at which the combined effect of the initial slit opening and the

space charge forces is minimized. Afterwards, the optical resolution of the system is defined.

Space charge effects

The propagation of an asymmetric beam such as a beamlet can be expressed as a system of two envelope equations [64]

$$\begin{aligned} \sigma_x'' &= \frac{I_p}{I_A(\sigma_x+\sigma_y)\gamma^3} + \frac{\varepsilon_{x,n}^2}{\sigma_x^3\gamma^2} \\ \sigma_y'' &= \frac{I_p}{I_A(\sigma_x+\sigma_y)\gamma^3} + \frac{\varepsilon_{y,n}^2}{\sigma_y^3\gamma^2}, \end{aligned} \tag{5.10}$$

where σ_x and σ_y are the transverse rms sizes of the beam and $\varepsilon_{x,y,n}$ is the normalized emittance.

Using this system of equations, we can estimate the dynamics of the beamlets in the drift region after the slit mask. Fourth order Runge-Kutta numerical integration was used to calculate the beamlet size evolution in the drift space. As input, the nominal values for PITZ were used, namely peak current of 50 A, normalized emittance 0.9 $mm \cdot mrad$ and rms beamsize at the slit mask, $\sigma_0 = 0.2$ mm and 0.5 mm. The rms envelope size evolution of the central beamlet is shown on figure 5.5 as a function of the drift length between the slit and the screen, derived from the above mentioned beam parameters. Only the charge that was cut with a slit placed in the center of an uniform symmetric beam is considered in the analysis. The different lines represent the cases of 10 μm slit opening without space charge forces acting (green dashed line), and 10 and 50 μm slit opening with space charge forces included (blue and red lines). The same was calculated for mean momentum of 15 MeV/c (fig. 5.5(a)) and 30 MeV/c (fig. 5.5(b)).

The green dashed line gives only the contribution from the initial beamlet size of 10 μm as discussed previously.

The influence of the space charge forces over the evolution of the beamlet size can be clearly seen in both cases of 10 and 50 μm slit opening. It is better pronounced at beam momentum of 15 MeV/c. At beam momentum of 30 MeV/c, the difference between the results with and without space charge becomes insignificant for the 10 μm slit opening case, but it is still visible at

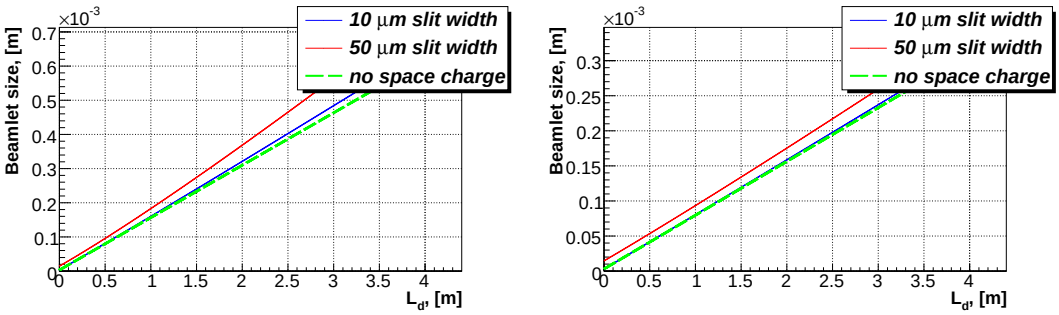

(a) $\vec{P}_{mean} = 15\ MeV/c$ (b) $\vec{P}_{mean} = 30\ MeV/c$

Figure 5.5: Beamlet size as a function of the drift length. Initial rms size is 0.2 mm, normalized emittance 0.9 $mm \cdot mrad$.

50 μm.

The emittance is then calculated using the definition in equation 5.6 and the beamlet size evolution as shown on the figures 5.5. The resulting deviation from the emittance at the slit mask is shown on figure 5.6 for $\sigma_0 = 0.2\ mm$.

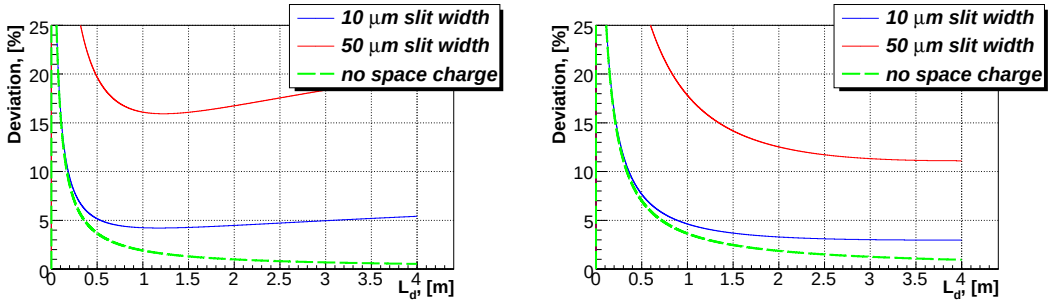

(a) $\vec{P}_{mean} = 15\ MeV/c$ (b) $\vec{P}_{mean} = 30\ MeV/c$

Figure 5.6: Deviation of the emittance as a function of the drift length. Initial rms size is 0.2 mm, normalized emittance 0.9 $mm \cdot mrad$.

It can be seen that the deviation drops abruptly in the beginning and slowly rises until the end of the examined region. The initial drop is due to the decreasing contribution from the initial beamlet size, while the increase that follows is caused by the space charge forces continuously acting on the beamlet.

If the same analysis is conducted for rms beam size of 0.5 mm at the slit mask position (results shown on figure 5.7) we see that the influence of the space charge is less important, however the beamlet size becomes significantly

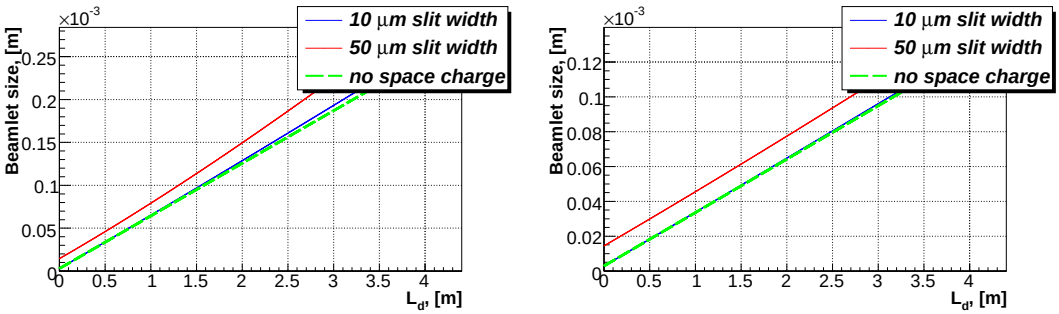

(a) $\vec{P}_{mean} = 15\ MeV/c$ (b) $\vec{P}_{mean} = 30\ MeV/c$

Figure 5.7: Beamlet size as a function of the drift length. Initial rms size is 0.5 mm, normalized emittance 0.9 $mm \cdot mrad$.

smaller, which will increase the contribution from the initial beamlet size and tightens the requirements for the optical readout system. The resulting uncertainty is shown on figure 5.8. Here the influence from the space charge for

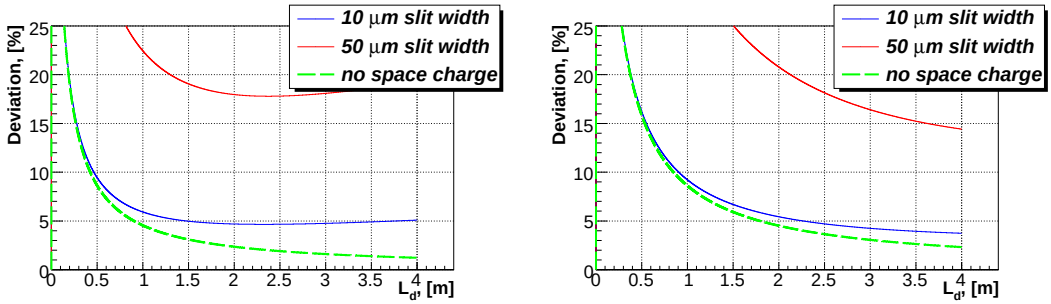

(a) $\vec{P}_{mean} = 15\ MeV/c$ (b) $\vec{P}_{mean} = 30\ MeV/c$

Figure 5.8: Deviation of the emittance as a function of the drift length. Initial rms size is 0.5 mm, normalized emittance 0.9 $mm \cdot mrad$.

the 50 μm slit opening becomes only visible after $L_d = 1\ m$ for the case of 15 MeV/c mean momentum and after 2.5 m for the 30 MeV/c case. Apparently the inverse is true for the contribution from the finite initial beamlet size.It is still 10% at $L_d = 1\ m$ and reaches 5% only at 2 m after the slit mask (figure 5.8(b)).

Choice of slit opening

Taking into account the analysis conducted above, the optimal slit opening should be 10 μm. However, this optimization was targeting only the small-

est emittance case of $\varepsilon_n = 0.9\ mm \cdot mrad$. Since the characterization of the photo-injector will consider beams with larger emittance, the influence of the space-charge and the finite initial beamlet size will be significantly smaller for the sake of lower signal density on the observational screen. Therefore, installation of 50 μm slit mask instead of the multi slit mask was implemented for the first two EMSY stations in the beamline.

Slit mask material and thickness

The aim of the slit mask is to absorb or scatter the residual electrons from the beam such that they do not influence the beamlet propagation and analysis i.e. produce a homogeneous background at the beamlet observational screen. The optimum thickness of the slit mask is a compromise between the need to scatter those electrons, which do not pass the slit and the acceptance of the slit, which if too small can poses great difficulty for the precision of the production and mechanical alignment.

Tungsten was the primary choice for slit material due to its high atomic number which implies short radiation length of 0.35 cm and its abilities to withstand high thermal load. First order approximation to the scattering of the residual electrons can be made using the formalism of the rms scattering angle [63].

$$\Theta_{rms} = \frac{19.2MeV}{E}\sqrt{\frac{s}{X_0}}\left[1 + 0.2\ln\left(\frac{s}{X_0}\right)\right], \tag{5.11}$$

where E is the kinetic energy of the electrons in the beam, s is the mask thickness, X_0 is the radiation length of the electrons in the material for that particular energy.

In order to reduce the density of the electrons scattered from the slit mask on a screen of diameter D, at a distance L_d, the rms scattering angle must obey $\Theta_{rms} \gg D/L_d$.

Knowing θ, an estimate for the signal to noise ratio S/N can be made, using the approximate expression (reference [63]):

$$S/N \geq \frac{1}{2}\left(\frac{\Theta_{rms} \cdot L_d}{\sigma(1 + \frac{\sigma' \cdot L_d}{d})}\right)^2 \tag{5.12}$$

where σ and σ' are the rms beam size and divergence of the incoming beam, and d is the slit opening.

For slit thickness of 1 mm, kinetic energy of 30 MeV, beamsize of 0.2 mm and divergence of 0.03 $mrad$ the lower level of the signal to noise ratio is about 740 at $L_d = 1\ m$ and 960 at $L_d = 2\ m$.

The inversely proportional dependence on the beam kinetic energy (equation 5.11) means that the most stringent requirements will be for the higher energy case. Beside the scattering from the atoms in the media, the electrons convert their kinetic energy also to gamma ray photons. In order to include the noise signal due to the scattered electrons and the photons produced in the process of scattering as well as the particles and photons created from the vacuum pipe, a Monte Carlo simulation using GEANT4 [65] was performed. The energy deposition and the signal to noise ratio S/N were estimated using

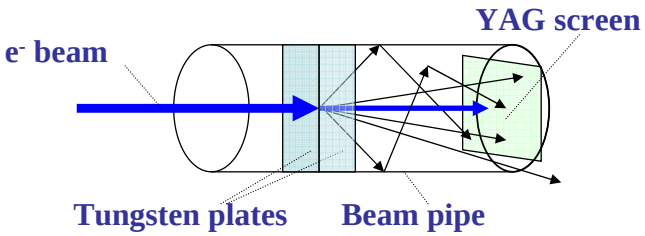

Figure 5.9: Simplified geometry model used for the GEANT4 simulations

the simplified geometry shown on figure 5.9.

$$S/N = \frac{\rho_s}{\rho_n} \tag{5.13}$$

The signal to noise ratio S/N was estimated using the light output from the YAG screen placed at 0.5, 1, 2 and 3 meters downstream the slit mask. The signal density is expressed as $\rho_s = N_s^{ph}/A_b$ where N_s^{ph} is the number of photons produced on the screen from the beamlet and A_b is the area on the screen covered by the beamlet. The noise density is $\rho_n = N_n^p/A_s$, where N_n^{ph} is the number of photons produced on the screen from the scattered electrons, positrons and photons, interacting with the screen of area A_s, which is 4×4 cm^2. The result for slit thickness of 1 mm and slit opening of 10 μm is shown on figure 5.10.

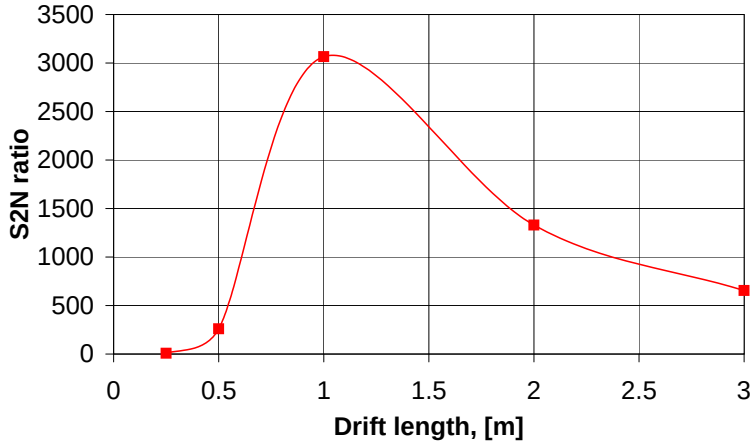

Figure 5.10: The signal to noise ratio for different drift lengths, mask thickness is 1 mm, slit opening 10 μm

5.3 Uncertainties and systematic deviations

Besides the the beam dynamics considerations, the influence of the initial beamlet size and the scattered electrons, there could be also a significant contribution from systems, auxiliary to the SSM. These include the beamsize measurement systems, momentum measurements and overall photo-injector stability.

Here the dynamic range of the EMSY will be described including uncertainties and the known systematic effects for the expected ranges of momentum, drift length, beam size at the slit and beam emittance. The influences of the CCD camera, like spatial and intensity resolution, positioning of the slit across the electron beam and the number of beamlet samples that are needed will be discussed here.

5.3.1 Beam size measurement

An important part of the emittance measurements concern the beam and beamlet size measurement. In PITZ, they are conducted with CCD camera-equipped YAG or OTR screens. Detailed examination of the uncertainties associated with the various screen configurations installed at PITZ was made in [66, 67]. There are three major sources of systematic deviations and uncertainty to the beam size measurements: the screen itself, the optical system for light transport and the camera used to grab and record the image data.

Screen setup

The contribution from the screen setup includes possible saturation of the scintillator (YAG only), increase of the beam size due to scattering in the material of the screen (90° geometry only, see figure 3.7(a)) or insufficient light intensity (OTR only, at energies lower than 15 MeV/c). It was estimated that the saturation of the scintillator play no role at PITZ, while the multiple scattering contribution becomes up to 10% at a beam momentum of 13 MeV/c and for beam sizes below 50 μm [67]. However such small beamlet size is expected only for higher beam momentum. Therefore measurements of beamlet sizes smaller than 50 μm should be conducted on the 45° OTR equipped screens (see figure 3.7(b)).

Optical system

The optical system includes a system of mirrors and an optical lens. Typical angular aperture of the optical system at PITZ is 0.05 rad with a distance between the center of the screen and the image plane of about 0.5 m. The optical resolution of the system depends on the magnification and is found to be in the range of 20 lines per millimeter (mm^{-1}) to 50 mm^{-1} for the magnification range 0.1 - 1.

The degradation of the beam image due to the finite optical resolution $f_{deg}(x)$ can be estimated from a convolution of the distribution of the point spread function $g(x)$ and the initial distribution $f(x)$.

$$f_{deg}(x) = \int_{-\infty}^{\infty} f(y-x)g(y)dy. \tag{5.14}$$

As a response function $g(x)$ and initial distribution $f(x)$ a Gauss distribution was used. The description of the optical resolution of the optical systems is made with the so called Modulation Transfer Function (MTF) formalism [67].

$$z(\omega) = \int_{-\infty}^{\infty} g(x)e^{-i\omega x}dx, \tag{5.15}$$

where ω is called spatial frequency. The optical resolution ω_0 is often defined as a solution of the equation 5.15 when the MTF $z(\omega_0) = 0.1$. In figure 5.11, taken from [67], the difference $\delta\sigma/\sigma = (\sigma_{deg} - \sigma)/\sigma$ between the RMS sizes

of the functions $f_{deg}(x)$ and $f(x)$ related to the initial beam size is shown as a function of the initial beam size for two common resolutions used at PITZ. The effect of the finite optical resolution on the beam size measurement results allways in increased size of the distribution, so it can be considered as another systematic deviation (see figure 5.11).

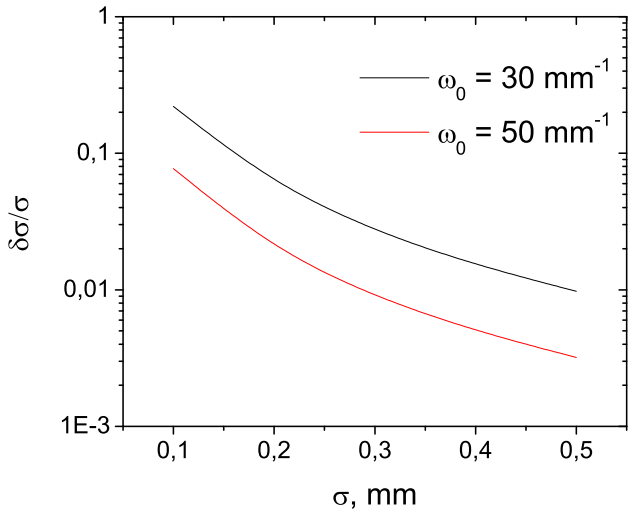

Figure 5.11: Influence of the optical resolution on the measured beam RMS size.

The finite thickness of the scintillation layer or the angle (45°) between the screen and the image plane of the optical system imply different optical paths between different parts of the image on the screen and the image on the CCD chip. This results in an additional deviation of the measured beam size from the real one. A point source situated at a distance l from the image plane results in a spot with radius:

$$\Delta f = l \cdot \tan \alpha \tag{5.16}$$

where α is the light cone. In the case of the YAG screen this is the optical aperture of the system ($\sim$0.05 rad), and for OTR it scales inversely proportional to the relativistic momentum $\alpha = 1/\gamma$. Numerical integration applied to an initial Gauss distribution with 0.1 and 0.5 mm RMS sizes reveals that one should restrict $\Delta f \leq 0.1\ mm$ in order to keep the deviation below 10 %. In the case of the YAG screen l must be kept below 2 mm. For electrons with

energy of 15 MeV the light cone from the OTR is 0.03 rad, and this allows us to use depth of field values up to $\pm 3.3\,mm$.

Contribution from the CCD camera

The main features of a CCD camera are the spatial resolution, defined by the total number of pixels over the size of the projected area in mm, and the digital resolution of the CCD chip defined by the Analog to Digital signal Conversion (ADC) associated with the camera. The main contribution to the uncertainty of the beamsize measurements with a CCD camera is the transformation of the image due to the discrete digital sampling of the amplitude signal from the chip. This effect becomes important when measuring beams with large halos, typical for the photo-injector. Beam halo was simulated by combination of two Gaussian distributions with different weight and RMS size. The "halo" part of the distribution was allways 2 mm rms size and 1/10 of the "core" distribution weight. The rms size of the "core" was changed such to produce combined rms size of 0.2 and 0.1 mm. In fig. 5.12, the projections of these two Gaussian

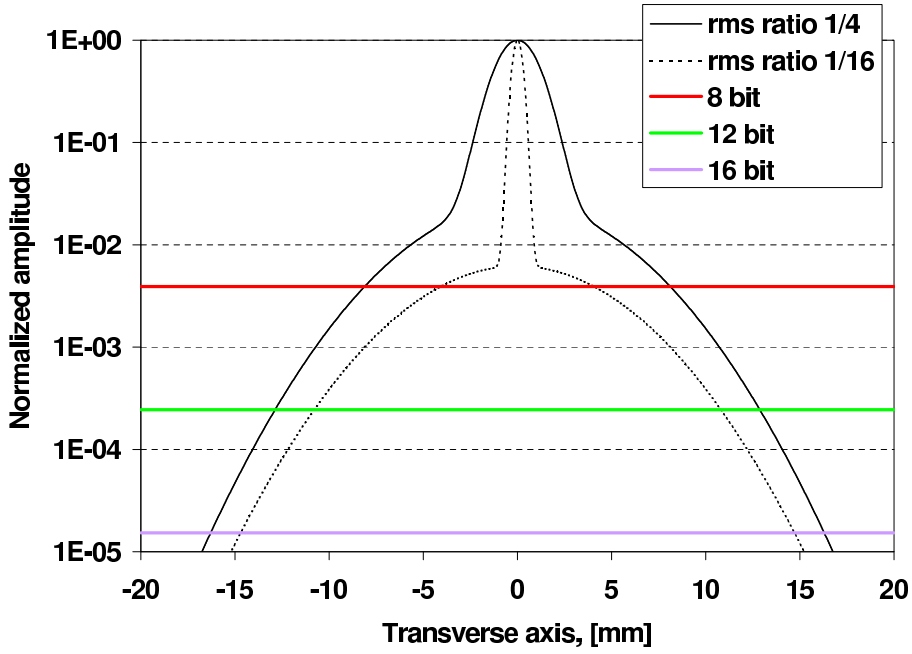

Figure 5.12: Profiles of two mixed Gaussian distributions together with the discrimination levels of 8, 12 and 16 bit.

distributions are shown, together with three different discrimination levels of 8, 12 and 16 bit. The resulting deviation from the initial RMS size is more

than -10 % for the 8 bit case and less than -1 % for the other two. The same

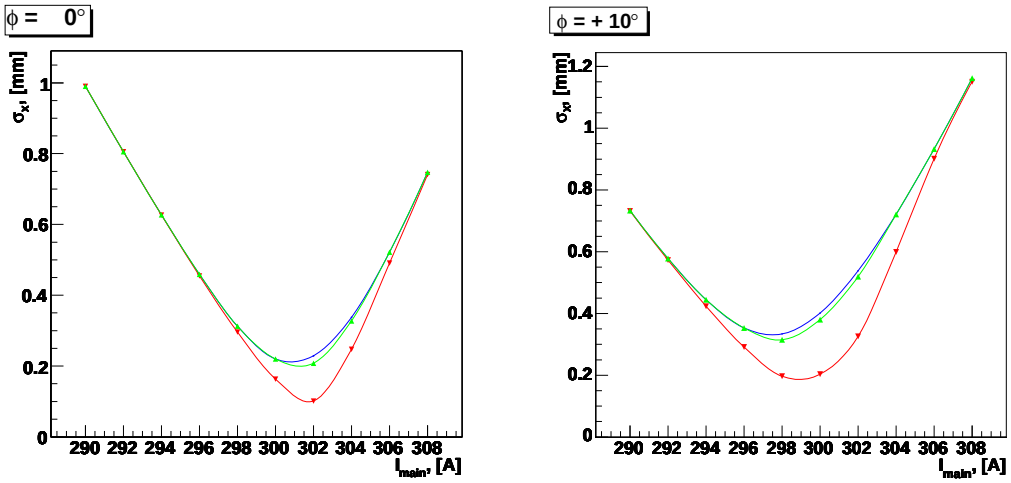

(a) $\phi_{gun} = \phi_0$ (b) $\phi_{gun} = \phi_0 + 10deg$

Figure 5.13: Deviation of the beamsize estimation due to discrimination of the amplitude. ASTRA simulations. The blue line indicates the original beamsize, as obtained from ASTRA, whereas red and green lines represent 8 and 12 bit transformation of the signal.

effect is also visible when a distribution obtained from ASTRA simulations is converted to a 2D discrete matrix of size comparable with the optical size of the CCD chip. The results from such an experiment are shown on figure 5.13. As can be seen, the discretization of the amplitude can have significant impact on the evaluation of the rms size of the distribution, which in the case of 8 bit discretization can bring a difference factor of two. For the 12 bit, this deviation does not exceed -2%. Therefore, 12 bit cameras must be used.

The most critical aspects of the beamsize measurement chain are the spatial resolution of the optical system and the digital resolution of the CCD camera.

5.3.2 Uncertainty of the momentum measurements

At PITZ the mean momentum is measured using a dispersive dipole magnet [34] and CCD equipped YAG screen. The main sources of error are due to mechanical alignment of the magnet with respect to the beam line and uncertainties in the calibration of the magnet field. Thorough analysis of the uncertainties of this system were performed in [34] where the maximum relative uncertainty of the momentum measurements is estimated to be 2%.

5.3.3 Summary

As discussed earlier, the main sources of uncertainty and systematic deviation in the emittance measurements can be summarized as:

- Uncertainty due to beam rms size measurement:
  - uncertainty from the calibration of the screen $\pm 0.5\%$.
  - uncertainty due to discretization of the amplitude of the signal in the CCD camera between 0 and -2%.
  - systematic increase of the measured beamsize due to finite optical resolution of the system.
- Uncertainty in the momentum measurements
- Uncertainties and systematic deviations associated with the divergence measurement
  - a systematic increase due to the space charge influence on the beamlet propagation.
  - a systematic increase due to the initial beamlet size as a fraction of the final beamlet size.
  - uncertainty of the drift length $\sim 0.5\ mm$
  - both sources of uncertainty associated with the beam size measurement.

As shown previously, the uncertainties due to the optical resolution are a function of the beamsize. Therefore, they can be easily parameterized using an appropriate beam distribution. The same is not true for the uncertainties associated with the discretization of the amplitude signal. The uncertainty contribution here was estimated not to exceed -2% for a 12 bit camera. Analysis using asymmetric envelope equations (equation 5.10) including the effect from the beamsize measurements can be applied in order to estimate the overall systematic deviation from space charge, finite slit opening, beam and beamlet size measurements. The systematic deviation of the single slit measurement of emittance is given on figures 5.14 as a function of the drift length at two different beam momenta and initial beam sizes.

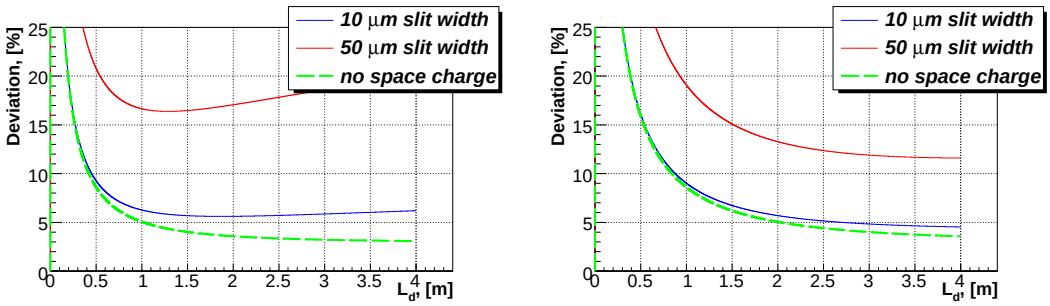

(a) $\sigma_0 = 0.2\ mm,\ P_{mean} = 15\ MeV/c$

(b) $\sigma_0 = 0.2\ mm,\ P_{mean} = 30\ MeV/c$

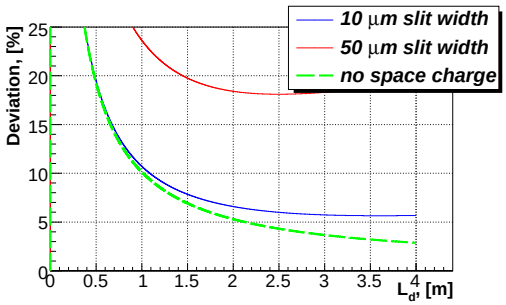

(c) $\sigma_0 = 0.5\ mm,\ P_{mean} = 15\ MeV/c$

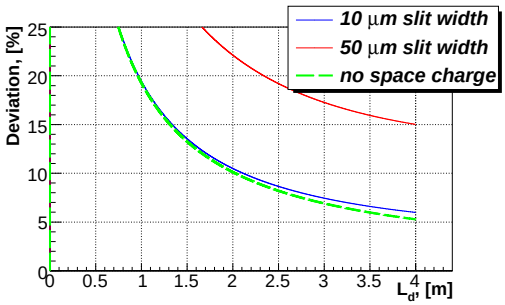

(d) $\sigma_0 = 0.5\ mm,\ P_{mean} = 30\ MeV/c$

Figure 5.14: Systematic deviation of the emittance measurement as a function of the drift length with beam size measurement systematics included. Initial rms normalized emittance is 0.9 $mm \cdot mrad$.

In the case where the mean momentum is 30 MeV/c and the beamsize is 0.5 mm (figure 5.14(d)), the uncertainty for measurements with the 10 μm slit drops below 10 % only after a drift length of about 2 m. This is caused from the tiny size of the beamlets due to the small divergence at $\sigma_0 = 0.5\ mm$ and $\varepsilon_n = 0.9\ mm \cdot mrad$.

Assuming a constant emittance of 0.9 $mm \cdot mrad$ and a drift length of 2 m, estimation of the systematic deviation of the measurement with the single slit is done in the interval $\sigma_0 = 0.1$ .. 1.0 mm and $P_{mean} = 10$ .. 40 MeV/c. The result is shown as color map on figure 5.15. The plot is limited to deviation less than 10 % and gives a clear overview on the working range of the SSM using 10 μm slit.

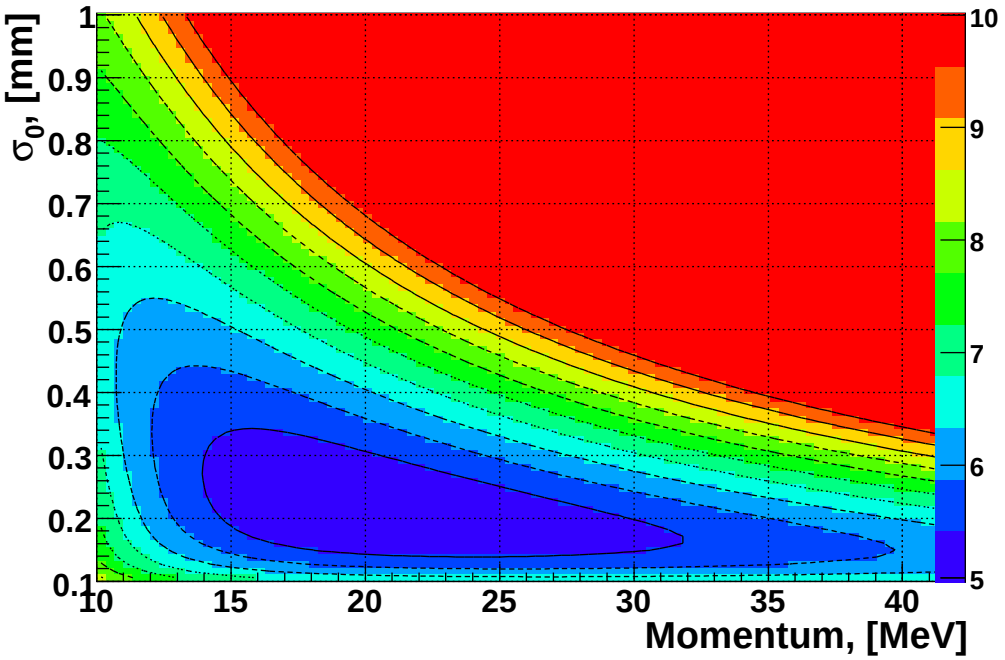

Figure 5.15: Systematic deviation in % as a function of the beam momentum and rms beam size at the slit mask. Optical resolution is 50 $lines/mm$, emittance is 0.9 $mm \cdot mrad$. The 10 μm slit was used.

The same is done for fixed beam momentum with varying beam size and emittance in the range $\sigma_0 = 0.1$ .. 1.0 mm and $\varepsilon_n = 0.5$ .. 5 $mm \cdot mrad$. The results for 15 and 30 MeV/c are shown on figures 5.16(a). and 5.16(b)

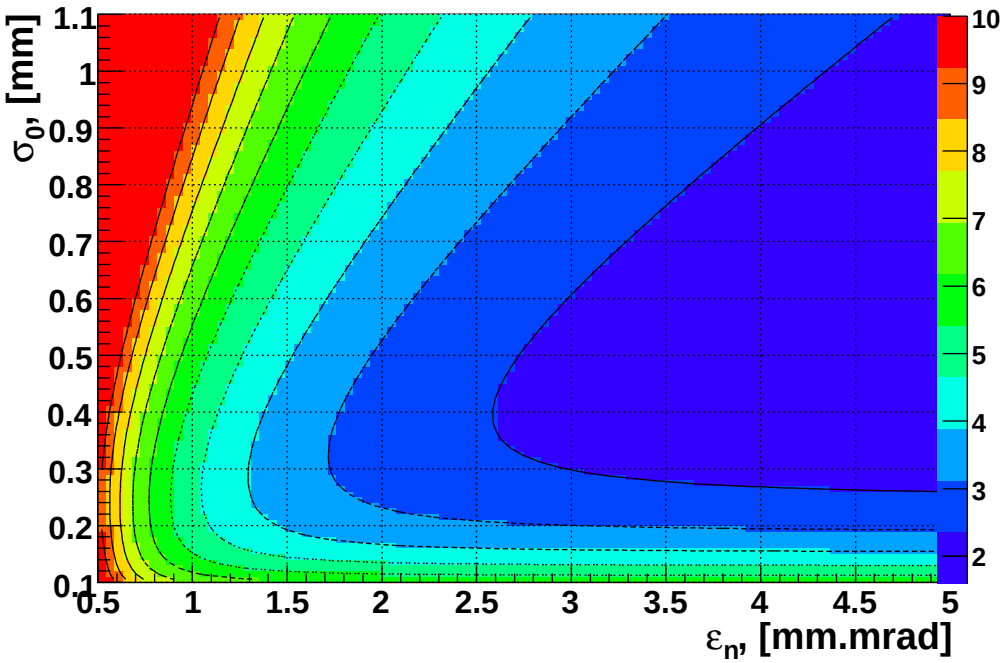

(a) $P_{mean} = 15\ MeV/c$

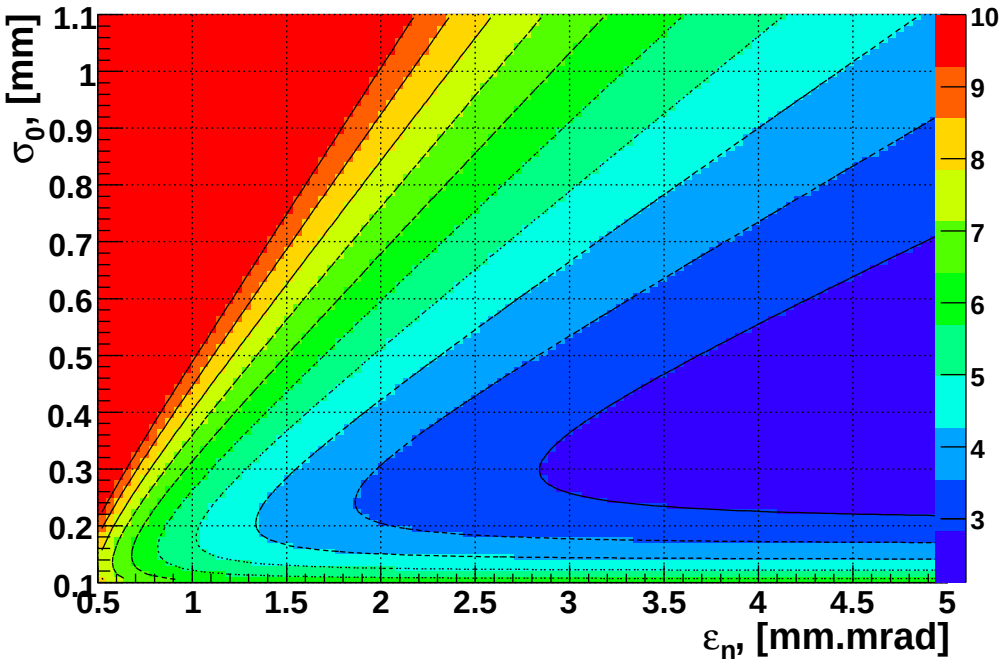

(b) $P_{mean} = 30\ MeV/c$

Figure 5.16: Systematic deviation of the SSM (in %) as a function of the beam normalized emittance and rms beam size at the slit mask. Optical resolution is 50 $lines/mm$. The 10 μm slit was used.

5.4 EMSY optimized parameters

In this chapter it was shown that emittance measurements with uncertainty lower than 10 % can be performed in a wide range of the photo-injector working parameters. In order to achieve this accuracy we have considered the following parameters for the measurement system:

- Slit mask
    - material tungsten
    - mask thickness 1 mm
    - Slit opening 10 μm
- Drift length $\geq$2 m
- Optical resolution $\geq$50 $lines/mm$
- Camera contrast 12 bit
- YAG and OTR screens for beamlet analysis

Chapter 6

Experimental results

Three emittance measurement systems (EMSYs) were produced by the High Tech-High Energy Physics (HT-HEP) group in the Institute for Nuclear Research and Nuclear Energy in Sofia-Bulgaria (INRNE-Sofia). The EMSYs were installed at PITZ on positions 4.3, 6.6 and 9.9 m downstream the cathode, in the spring of 2006. The devices were commissioned and integrated in the PITZ control system in the next gun conditioning period. During the commissioning phase, complete functional tests of all the devices were made. These included stiffness of mounting, ultra high vacuum tests, movement and control of the actuators, screen and camera performance. In parallel, a new control system interface that allows extended controls functionalities and automatization of the measurements was elaborated, with subsequent development of an automatic measurement and analysis procedure.

6.1 Commissioning of the emittance measurement system

The EMSYs were commissioned in the conditioning period at PITZ between May and August 2006. The transparency and the angular acceptance of the slits were measured for all the slits in the three EMSY's. The bunch charge was 1 nC, the focusing current in the main solenoid was 295 A and the total beam momentum was 11 MeV/c, after acceleration with the booster. The result obtained for EMSY-1 (installed at 4.3 m downstream the cathode) are shown on figure 6.1 for 50 μm and 10 μm slits. Since the thickness of the slit

mask is 1 mm, the angular acceptance of the slits should be 50 and 10 mrad for the 50 and 10 μm slits, respectively.

On figure 6.1(a) the beam was scanned transversely with the 50 μm slit and the intensity of the beamlets measured on a screen placed 1.914 m downstream the slit is shown as red dots and line. This corresponds to the transverse beam projection.

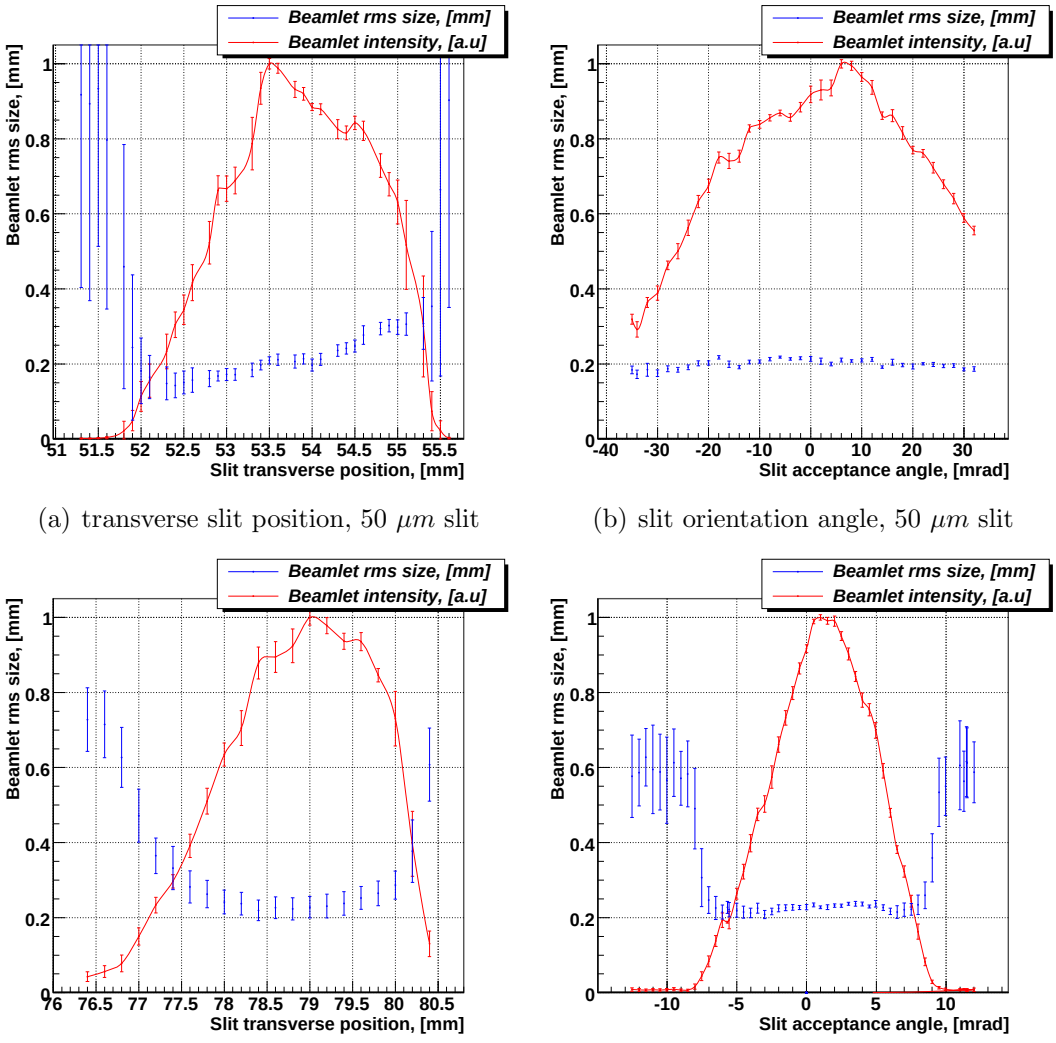

(a) transverse slit position, 50 μm slit

(b) slit orientation angle, 50 μm slit

(c) transverse slit position, 10 μm slit

(d) slit orientation angle, 10 μm slit

Figure 6.1: Tests of the installed 50 and 10 μm opening of the slits. The blue dots represent the beamlet rms size, red line the intensity of the beamlets is shown. The mean value out of 50 measurements is plotted with error bars representing the standard deviation from the mean.

After the position of the slit corresponding to the maximum was found

(in this case at slit position 53.5 mm), the angular orientation of the slit was scanned with the slit transverse position set to the position of the maximum intensity 53.5 mm. The result is shown on figure 6.1(b). Due to restrictions in the maximum bending angle of the bellows of the EMSYs the acceptance angle can be only scanned in the range ± 35 $mrad$, which is not enough to cover the full range of angular acceptance of the 50 μm slit mask. Nevertheless, one could extrapolate the shape of the distribution and reach an angular acceptance of about 50 $mrad$. As can be seen, the angle of maximum charge transmission is at about $+7$ $mrad$. As expected, the beamlet size changes across the beam (blue dots on figure 6.1(a)) mainly because of different local divergence. At the edges of the distribution, the rms size tend to increase dramatically as a result of increased local divergence and low signal to noise ratio. It is important to note that the beamlet rms size stays relatively constant during the full range of the scan of the angular acceptance. This shows that the electrons scattered on the edges of the slit mask do not contribute to the measured value although more than 60 % of the beamlet is scattered, i.e. at angle -31 $mrad$. The small variations of the rms size with respect to the angular acceptance could be a result of slow drifts in the machine working parameters since the scan took more than 30 minutes.

The same procedure as described for figures 6.1(a) and 6.1(b) was repeated also using the 10 μm slit and the results are shown on figures 6.1(c) and 6.1(d). The transverse slit location corresponding to the maximum charge transmission in this case was scanned when the slit was already rotated on $+7$ $mrad$ and in this case it is at 79 mm (see figure 6.1(c)). The angular acceptance of about 10 $mrad$ of the 10 μm slit is clearly visible on figure 6.1(d). Here the beamlet size is constant as long as at least 10 % of the beamlet charge at full transmission is passing through the slit. The rapid growth of the beamlet rms size outside of this range is caused by the higher uncertainty due to the low signal to noise ratio at this charge transmission rather than the scattering of the electrons in the walls of the slit.

6.2 PITZ optimization

The optimization of the PITZ photo-injector was done in two stages using two different gun cavities of the same prototype, called gun 3.1 and gun 3.2. Gun 3.1 was installed and conditioned in 2006 and gun 3.2 was installed and conditioned in 2007.

The first optimization stage was realized in October 2006, using gun prototype 3.1. This gun was foreseen as a spare gun for FLASH and therefore was conditioned using a maximum peak power of 3.5 MW, available from a 5 MW klystron. This power corresponds to a maximum accelerating field at the cathode surface of about 43 MV/m. Besides a detailed characterization of the electron source for FLASH, the goal was to verify that the usage of 10 μm slits delivers reliable results, to elaborate the operation with three emittance measurement devices and to establish procedure for automatization of the emittance measurements.

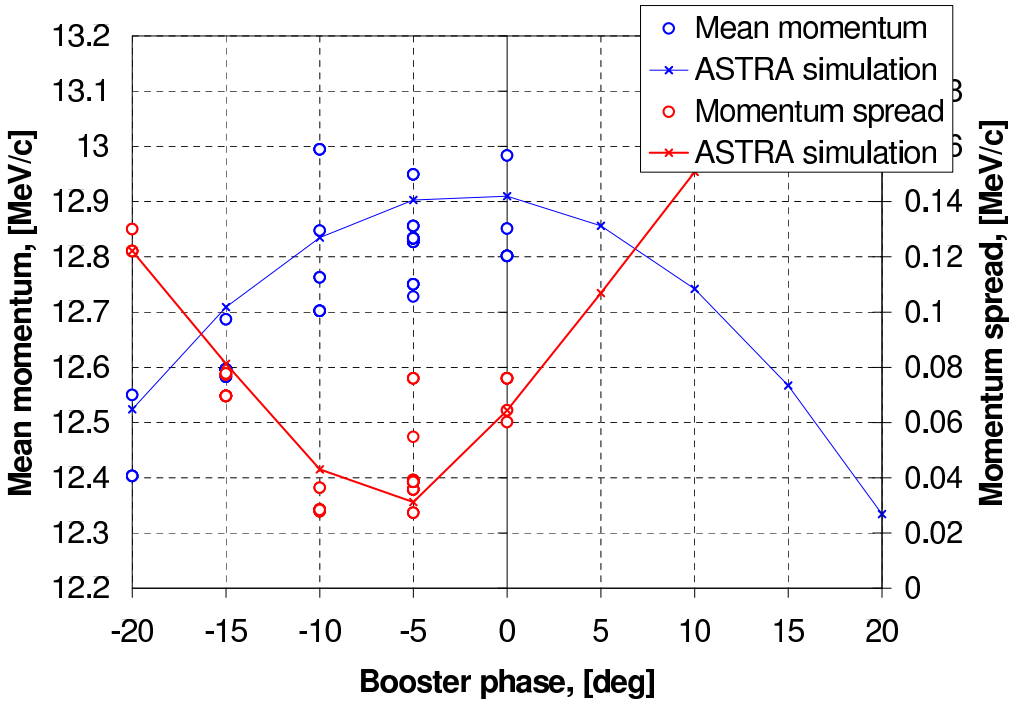

Figure 6.2: Mean momentum and momentum spread measured as a function of the booster phase. Lines show the results from simulations with ASTRA.

The projected emittance was measured at three different longitudinal positions. Only 8 bit JAI cameras were used in this characterization period. As

the main optimization parameter the focusing strength of the main solenoid was used, and as secondary parameter the phase of the booster cavity.

Other important photo-injector parameters such as the transverse size of the photo cathode laser and the phase between the RF wave in the gun and the laser beam were fixed to values experimentally optimized earlier at PITZ (see in [28]). A booster cavity with an accelerating gradient of about 14.8 MV/m was used as additional acceleration. This corresponds to 13.1 MeV/c maximum mean beam momentum after the booster cavity. The value for maximum accelerating gradient was estimated fitting the dependence of the mean momentum on the booster phase to a simulation with ASTRA using the field distribution given on figure 3.6. The result from the fit is shown on figure 6.2.

The complete list of photo-injector parameters used for the characterization of gun 3.1 is shown on table 6.1.

Table 6.1: Main injector parameters in October 2006 (gun 3.1).

Parameter	**value**	**Units**
Gun cavity:		
maximum gradient at the cathode	40 to 43	$[MV/m]$
RF phase	-2	$[deg]$
Booster cavity:		
maximum gradient	14.8	$[MV/m]$
RF phase	-20 to 0	$[deg]$
Cathode laser:		
transverse rms size, σ_{ini}	0.51 to 0.55	$[mm]$
longitudinal profile: FWHM	17 to 21	$[ps]$
longitudinal profile: rise/fall	6.0 to 7.5	$[ps]$
Electron beam:		
charge per bunch	1	$[nC]$
mean momentum after the gun	4.8 to 5.1	$[MeV/c]$
mean momentum after the booster	12.6 to 13.1	$[MeV/c]$
solenoid current	278 to 300	$[A]$

In the next optimization step, gun 3.2 (which is of the same prototype), was installed and conditioned to peak power of up to ∼6.7 MW, corresponding to about 60 MV/m maximum accelerating gradient. Here the main goal was to establish the optimum working point for the photo-injector operating at 60

Table 6.2: Main injector parameters in August 2007 (gun 3.2).

Parameter	**value**	**Units**
Gun cavity:		
maximum gradient at the cathode	58 to 60	$[MV/m]$
RF phase	0	$[deg]$
Booster cavity:		
maximum gradient	5.7 to 14.8	$[MV/m]$
RF phase	0	$[deg]$
Cathode laser:		
transverse rms size, σ_{ini}	0.35 to 0.55	$[mm]$
longitudinal profile: FWHM	17 to 21	$[ps]$
longitudinal profile: rise/fall	6.5 to 7.3	$[ps]$
Electron beam:		
charge per bunch	1	$[nC]$
mean momentum after the gun	6.1 to 6.6	$[MeV/c]$
mean momentum after the booster	9 to 14.5	$[MeV/c]$
solenoid current	360 to 380	$[A]$

MV/m maximum gradient at the cathode and to demonstrate the advantage of a higher gun gradient. For this purpose, the focusing strength of the main solenoid, the transverse size of the photo cathode laser and the maximum accelerating gradient of the booster cavity were scanned. The phases of the gun and the booster were fixed at the maximum mean momentum gain for both cavities, which appeared to be close to the numerically optimized values. The full set of the photo-injector control parameters during the optimization of gun 3.2 is shown on table 6.2.

6.2.1 Beam dynamics simulations

Extensive studies of the beam dynamics in the PITZ photo-injector were made using the program ASTRA [68]. The goal was to establish the most sensitive parameters of the photo-injector and to limit our optimization effort by narrowing the range of the scan to the most important parameters. The full range of the numerical optimization was restricted to the capabilities of the PITZ photo-injector, namely maximum accelerating gradients of the gun and the

booster cavities. The optimum operation point of the PITZ photo-injector was studied using a parallel multi-dimensional search method based on the Nelder-Mead simplex method. This algorithm was called Simplex Wide Area Routing Method (SWARM). The basic idea of the SWARM is to start a large simplex set on multiple hosts (i.e. on a Linux farm), to monitor the development of each simplex and guide them toward the global minimum. In addition, the large number of simultaneous optimizations allows the SWARM to build maps in the examined parameter space and to analyze the existing cross-correlations between the optimization parameters. Based on these input, SWARM is able to initiate a new generation of simplex drones swarming around the interesting areas in the examined parameter space.

A large amount of ideas on improving this tool were borrowed from the Multi-Variate Optimization program (MVO) developed by I.Bazarov in Cornell University, USA [69].

Gun accelerating gradient 40 MV/m

The main PITZ photo-injector parameters during the optimization of gun 3.1 are shown in table 6.1. Parameters such as the phase of the gun or the cathode laser transverse size were fixed to values that were experimentally optimized at PITZ using other gun prototypes (see in [28]). The initial particle distribution used for the simulations is shown on figure 6.3.

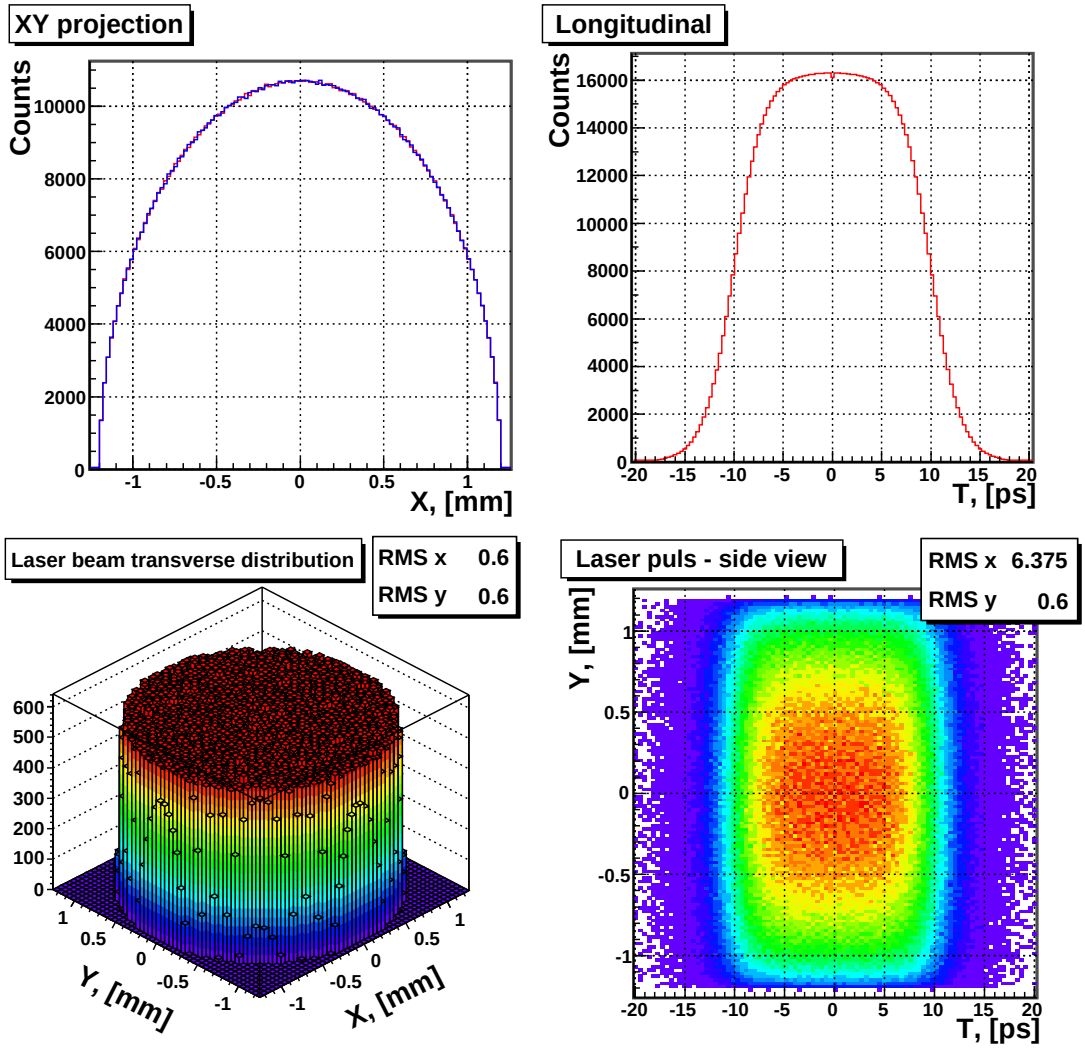

Figure 6.3: Initial particle distribution used for simulations. The transverse size is scaled according to the needs. The width of the initial energy distribution is 0.55 eV.

Dependance of the emittance on the focusing strength of the main solenoid

As was pointed out in chapter 4, the space charge compensating solenoid is an indispensable part of the high brightness photo-injector. On figure 6.4 the minimum emittance found with SWARM for a wide range of solenoid focusing strength is shown, at three different positions downstream the cathode. These positions are at the same distance from the cathode as the three installed EMSYs. In this case the SWARM search was taking place simultaneously in

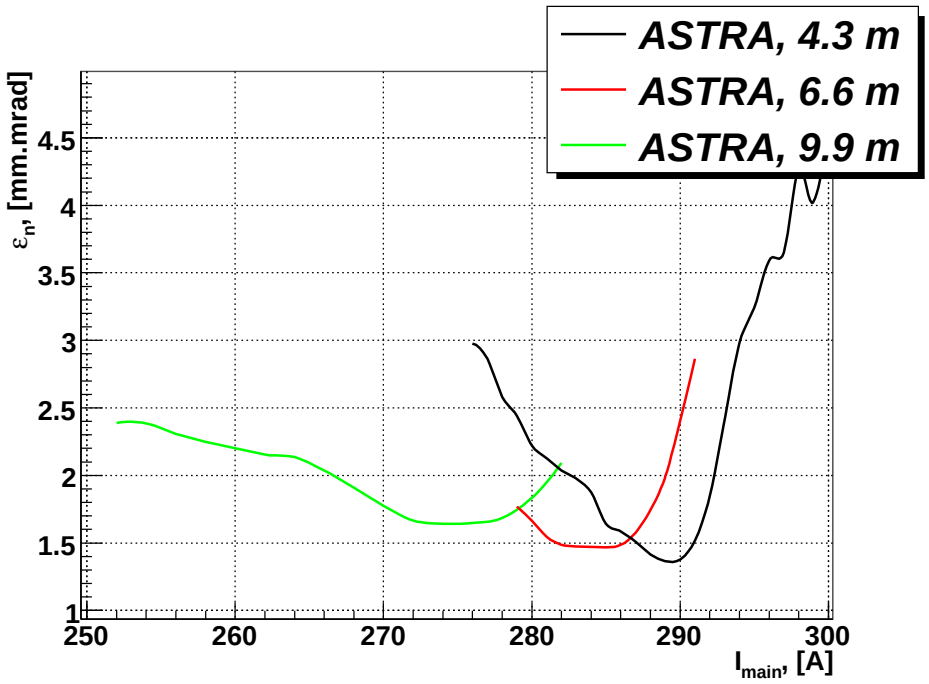

Figure 6.4: ASTRA simulation of the minimum emittance as a function of the main solenoid focusing strength at three locations downstream the cathode corresponding to the EMSY positions. The maximum accelerating gradient at the cathode is chosen to be 41.85 MV/m. The laser distribution used for the simulations (shown in figure 6.3) has 20 ps FWHM and 6 ps rise and fall times. 20000 particles were used in the simulations.

4 dimensions, namely the solenoid strength in the range 250 to 300 A, the transverse diameter of the cathode laser in the range of 0.3 to 1.2 mm and the two phases of the RF cavities. The maximum accelerating gradients in the gun and booster cavities were fixed to a values corresponding to the maximum achievable mean momentum gain, respectively 41.85 MV/m for the gun and

14.8 MeV/m for the booster. The global emittance minimum was found at

Table 6.3: Locations of the minima at the examined locations, maximum gradient at the cathode is 41.85 MV/m.

Parameter	**EMSY1**	**EMSY2**	**EMSY3**	**unit**
downstream location	4.3	6.6	9.9	$[m]$
transverse laser rms size	0.67	0.78	0.98	$[mm]$
phase of gun	-2.5	-1.5	-0.5	$[deg]$
phase of booster	-20	-20	-20	$[deg]$
solenoid current	289	285	274	$[A]$
minimum emittance	1.36	1.47	1.73	$[mm\ mrad]$

EMSY 1 ($z = 4.3\ m$) for the following conditions: initial cathode laser transverse rms size 0.67 mm, the phase of the gun $\phi_g = -2.5\ deg$, booster phase[1] $\phi_b = -20\ deg$.

At the other EMSY positions, 6.6 and 9.9 m, the minima locations are given in table 6.3.

ASTRA simulation of the dependence of the emittance and the beamsize on the solenoid strength is shown on figure 6.5. There, the other injector parameters were fixed to the case delivering the lowest emittance at $z = 4.3\ m$, and 200000 particles were used. In comparison with the results from the optimization shown on figure 6.4, the minimum of the emittance at the other two locations is shifted to lower values of the solenoid current, than obtained with the SWARM. The dependence of the emittance on the main solenoid focusing starts to develop a double minimum corresponding to the different compensating conditions for the slices on the head and the tail of the bunch.

[1]This in practice is the lower limit of the search range. The dependence of the emittance on the booster phase is not very pronounced, at $\phi_b = 0\ deg$ the emittance is 1.39 while for the $\phi_b = -20\ deg$ the emittance is 1.37 $mm \cdot mrad$

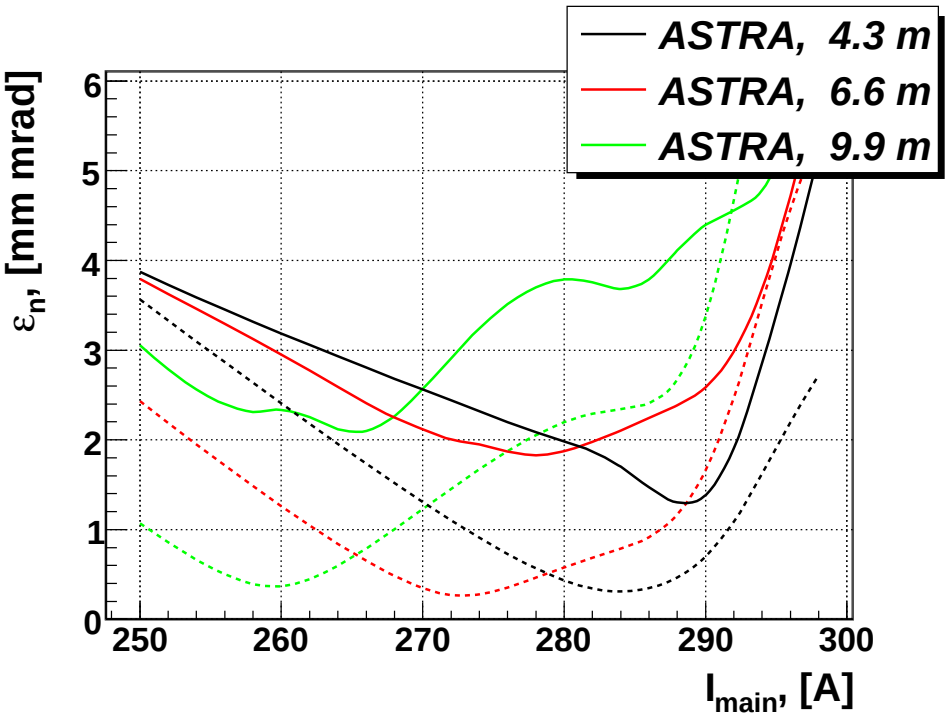

Figure 6.5: ASTRA simulation of the emittance (lines) and the beamsize (doted) as a function of the main solenoid focusing strength at three location downstream the cathode corresponding to the EMSY positions. 200000 particles were used and machine operation parameters are the same for all curves. Doted lines show rms beamsize in mm.

Gun accelerating gradient 60 MV/m

Increase of the maximum accelerating gradient at the cathode to 60 MV/m allows one to decrease the initial size of the cathode laser. This does not deteriorate the beam emittance due to space charge but improves it instead, due to reducing the effect of the nonlinear RF contribution and the thermal emittance - both of which are proportional to the initial beamsize.

On figure 6.6 the dependence of the emittance as a function of the cathode laser rms size σ_{ini} is shown.

What is obvious is that the higher gradient considerably lowers the emittance. The overall lowering of the emittance is a result of reduced space-charge influence due to the faster acceleration. In addition, it allows usage of smaller initial beam sizes that further relax the contribution from the thermal emittance and the nonlinear RF effects.

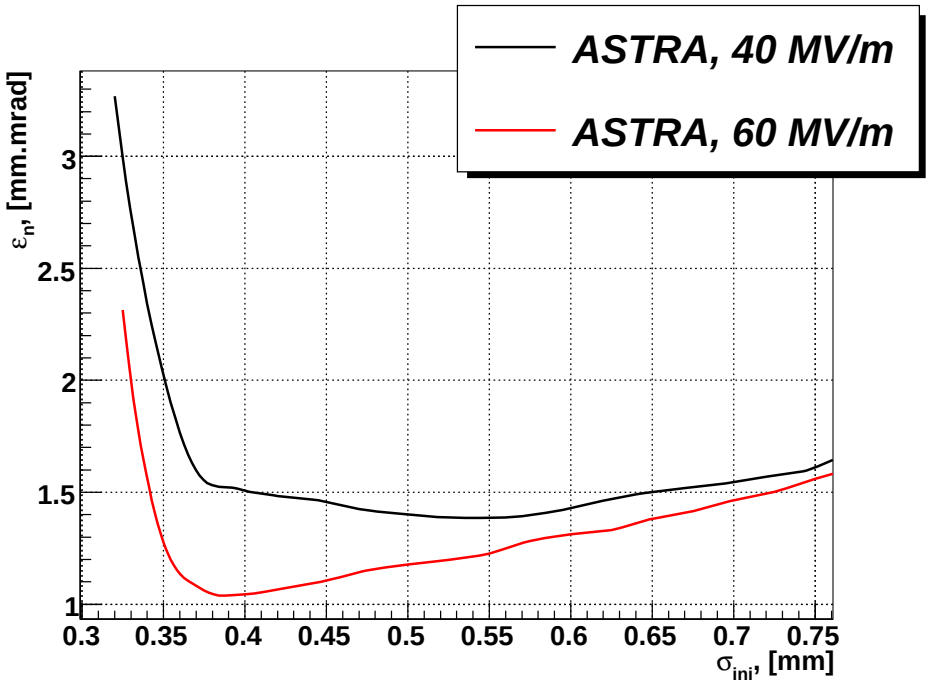

Figure 6.6: ASTRA simulation of the minimum emittance as a function of the initial laser spot size. 20000 particles used. The RF phase of the gun is 0 *deg*, maximum accelerating gradient is 60 MV/m for the red line and 40 MV/m for the black line, longitudinal laser distribution is a flat-top with 20 *ps* FWHM and 6 *ps* rise/fall edges. The initial kinetic energy of the electrons was set to $E_k = 0.55\ eV$.

6.3 Emittance measurements with gun 3.1

6.3.1 Verification of the influence of the slit width

As it was shown in chapter 5, the slit opening can bring considerable uncertainty to the emittance measurements. During the characterization of gun 3.1 some of the measurements were done consequently with both 10 and 50 μm slits and the results were used to verify the estimations made in section 5.2.2. Those measurements that do not fulfill the consistency requirements, i.e. the light signal intensity out of the beamlets observational screen (data consistency description is given in the Appendix), were not considered. As expected, the comparison between the two slit openings showed systematic increase of the emittance obtained with the 50 μm slit. In table 6.4 and in the following figures 6.7(a) and 6.7(b) are some examples of the comparison with both slits. Where Δ_m is the relative deviation of the 50 μm value to the 10 μm one,

given in % or $\Delta_m = \frac{\varepsilon_{50\mu m} - \varepsilon_{10\mu m}}{\varepsilon_{10\mu m}} 100$. Δ_{ae} is the deviation predicted from the asymmetric envelope equations (equation 5.10), in the same manner as Δ_m. As σ_0 the measured rms beamsize σ at the position where the slit mask is located was used. Error bars in the table and the plots are representing only the uncertainty due to statistical fluctuations of the measured value.

Table 6.4: Comparative measurements with 10 and 50 μm slit. z = 4.3 m downstream the cathode (EMSY1), RF phase of the gun is -2 *deg*

I_{main}, $[A]$		ϕ_b, $[deg]$	$\varepsilon_{10\mu m}$, $[mm \cdot mrad]$	$\varepsilon_{50\mu m}$, $[mm \cdot mrad]$	Δ_m, [%]	σ, $[mm]$	Δ_{ae}, [%]
286		5					
	Y		1.43±0.13	1.48±0.13	3.7	0.6	6.5
282		10					
	X		1.53±0.12	1.68±0.12	10.5	0.54	6.5
	Y		1.67±0.16	1.71±0.20	2.1	0.43	6.8

It is shown that the systematic deviation between both types of measurement can be in reasonable agreement with the predictions made with the help of the asymmetric envelope equations 5.10.

On figure 6.7(a) is given a similar comparison for a complete scan of the emittance dependence on the main solenoid focusing strength.

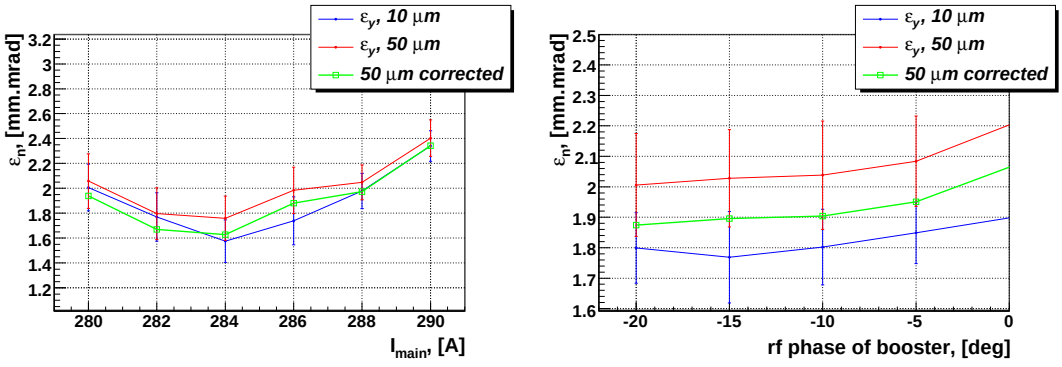

(a) Scan against the solenoid focusing strength, $\phi_b = -15$ *deg*

(b) Scan against the phase of the booster, $I_{main} = 283$ *A*

Figure 6.7: Comparative measurements with 10 (blue line) and 50 (red line) μm slit. The green line corresponds to a correction of the red line using deviation predictions obtained from the model in Chapter 5.

The same comparison was done also for a fixed solenoid current and a varying phase of the booster, relative to the phase of the maximum momentum gain. The results are shown in figure 6.7(b). One can see that even with the correction a systematic deviation between 4 and 7 % is still visible on figure 6.7(b). By detailed comparison of the two sets of data a small difference in the beamlet signal intensity was found, which could explain this deviation.

6.3.2 Emittance results with gun 3.1

Emittance as a function of the solenoid strength and booster phase

The emittance dependence on the solenoid strength was examined as a function of the distance from the cathode for different booster RF phases. As the reliability of the slit measurement using 10 μm was confirmed, a decision to use only the 10 μm slit was made, where only in case of low signal the 50 μm slit should be used. The emittance dependence on the solenoid focusing strength was measured for several phases of the booster and for fixed gun phase of $\phi_g = -2\ deg$ (see table 6.1).

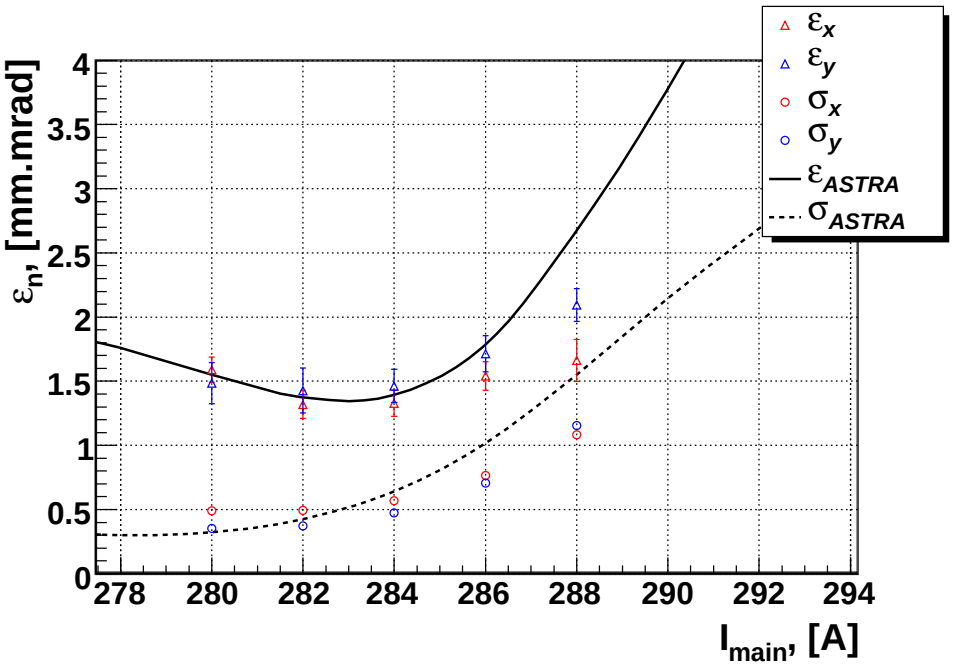

Figure 6.8: Emittance as a function of the solenoid focusing strength, measurements and simulations at $\phi_b = -5\ deg$, $\phi_g = -2\ deg$. The rms beam size is shown in mm (open circles).

On figure 6.8 the results from emittance measurements at booster phase $\phi_b = -5\ deg$ for different values of the main solenoid focusing current[2] are compared to a fit made using ASTRA simulations. The goal function of the comparison with ASTRA was the beam size at the position of the emittance minimum ($I_{main} = 282\ A$) and the geometrical average of the emittance in both transverse planes $\sqrt{\varepsilon_x \varepsilon_y} = 1.37 \pm 0.1$. The input for the simulations is summarized in the table 6.5. A uniform transverse distribution of the shape shown on figure 6.3 was used. The initial kinetic energy spread is related to the transverse emittance via equation 4.9, and the optimistic value of $E_k = 0.55\ eV$ from [44] was used. The field balance in the gun cavity is defined as the ratio between the maximum field in the half cell and the maximum field in the full cell, and it was measured in [27] to be about 1.06. The maximum accelerating gradient at the cathode was estimated from the measurements in [27]. The field balance has an important role in the emittance compensation scheme since it determines the γ' at the very beginning of acceleration where the forces of the bunch space charge are most relevant. No measurement data is available for the maximum gradient in the booster cavity, so the final beam momentum in the simulations was tuned to coincide with the measured one. For this particular scan of emittance vs. the solenoid current, no direct measurement of the mean momentum after the gun was made. For the sake of comparison the average mean momentum in the whole measurement period of October 2006 is given in table 6.5.

Using the same conditions as obtained from the fit of the minimum emittance, the simulations were repeated for $\phi_b = -10\ deg$ and $\phi_b = -15\ deg$ and compared with the measurements on figure 6.9. There is fairly good agreement between the measurements and the simulations.

Emittance as a function of distance to the cathode

The optimum emittance was studied also as a function of the distance from the cathode. The transverse projected emittance was measured with the same conditions at $z = 6.6\ m$ and $z = 9.9\ m$ downstream the cathode at the positions where EMSY2 and EMSY3 were installed. The results are shown on figures 6.10(a) and 6.11(a) for EMSY2 and on figures 6.10(b) and 6.11(b) for

[2]For the measurements done with gun 3.1 the set point of the solenoid current is used.

Table 6.5: Simulation parameters for the fit in figures 6.8 and 6.9.

Parameter	ASTRA	Meas.	Units
Initial transverse size at the cathode	0.55	0.55	$[mm]$
Initial kinetic energy spread	0.55	–	$[eV]$
Field balance in the gun cavity	1.04	1.06	[%]
Max. accelerating gradient at cathode	41.05	–	$[MV/m]$
Max. accelerating gradient in booster	14.8	–	$[MV/m]$
Gun phase	-2	-2	$[deg]$
Booster phase	-5	-5	$[deg]$
Mean momentum after the gun	4.84	4.94	$[MeV/c]$
Mean momentum after the booster	12.85	12.83	$[MeV/c]$

EMSY3. These results together with measurements at EMSY1 are summarized on figure 6.12 where the geometrical average $\varepsilon_{x,y} = (\varepsilon_x \cdot \varepsilon_y)^{1/2}$ is plotted with a different color for each location downstream. Since we are limited in the maximum accelerating gradient about 14.8 MV/m in a booster cavity of 1.35 m length, the emittance conservation can not be demonstrated yet.

On figure 6.13 the results from the emittance measurement at $I_{main} = 282\ A$ at the three EMSY positions is plotted together with ASTRA simulations using the same conditions as given in table 6.5. The results at EMSY2 and EMSY3 strongly disagree with the expectations from the numerical simulations. After more detailed studies of the problem, it was found that due to limitation in the machine aperture, the minimum against the solenoid current could not be demonstrated for positions 6.6 and 9.9 m downstream the cathode. See for example figure 6.14(a) and figure 6.5 where all the minima, except at EMSY1 are achieved for solenoid current below the threshold given by the aperture (see following subsection and figures 6.14(a) and 6.14(b)).

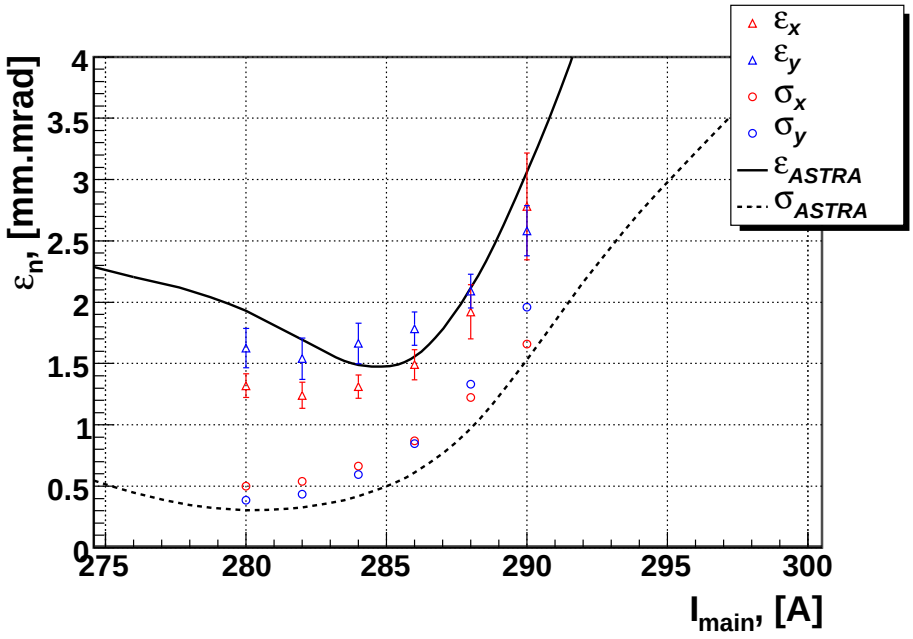

(a) $\phi_b = -10\ deg$

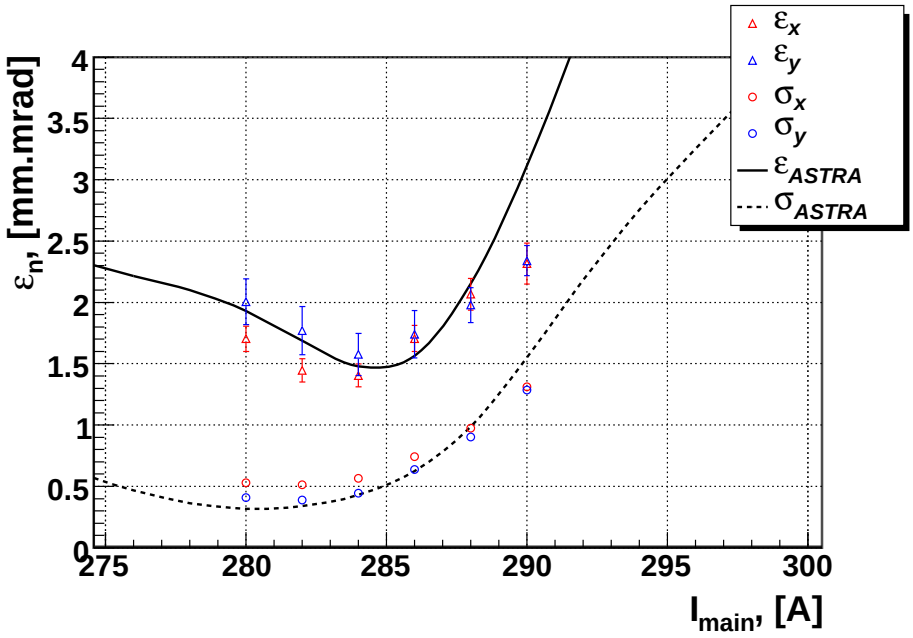

(b) $\phi_b = -15\ deg$

Figure 6.9: Transverse emittance (ε_x and ε_y) as a function of the solenoid focusing strength, measurements and simulations at EMSY1 ($z = 4.3\ m$), $\phi_g = -2\ deg$, two booster phases. The rms beam size is shown in mm (open circles).

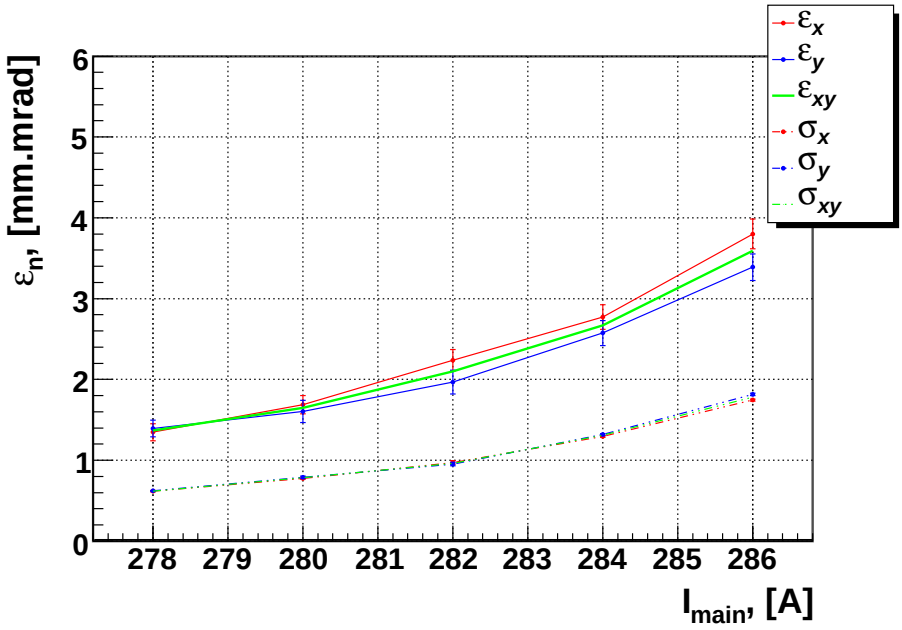

(a) EMSY2, $\phi_b = -10\ deg$

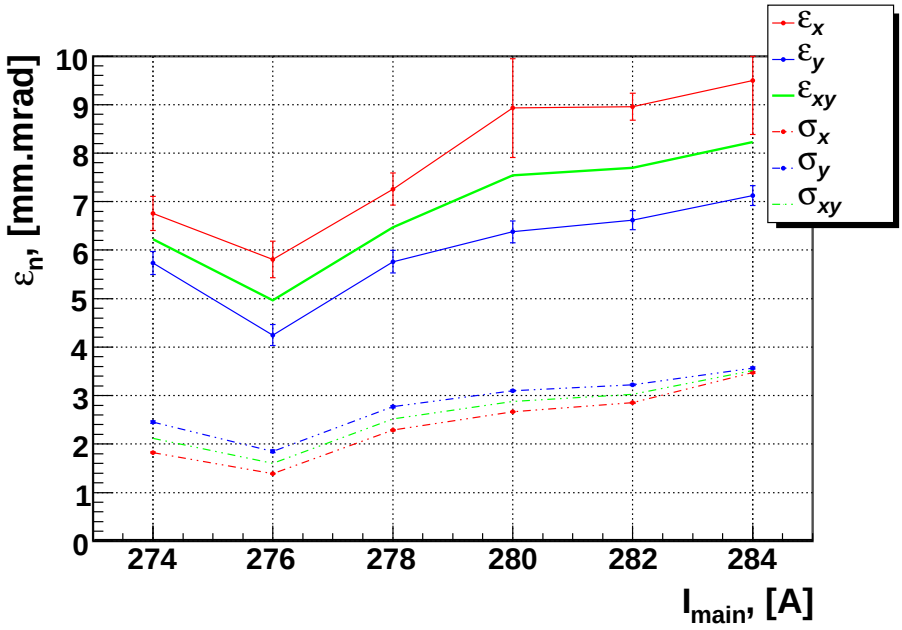

(b) EMSY3, $\phi_b = -10\ deg$

Figure 6.10: Measurement of the emittance at EMSY2 (6.6 m) and EMSY3 (9.9 m) as a function of the solenoid focusing strength, $\phi_g = -2\ deg$. The rms beam size is shown in mm (open circles).

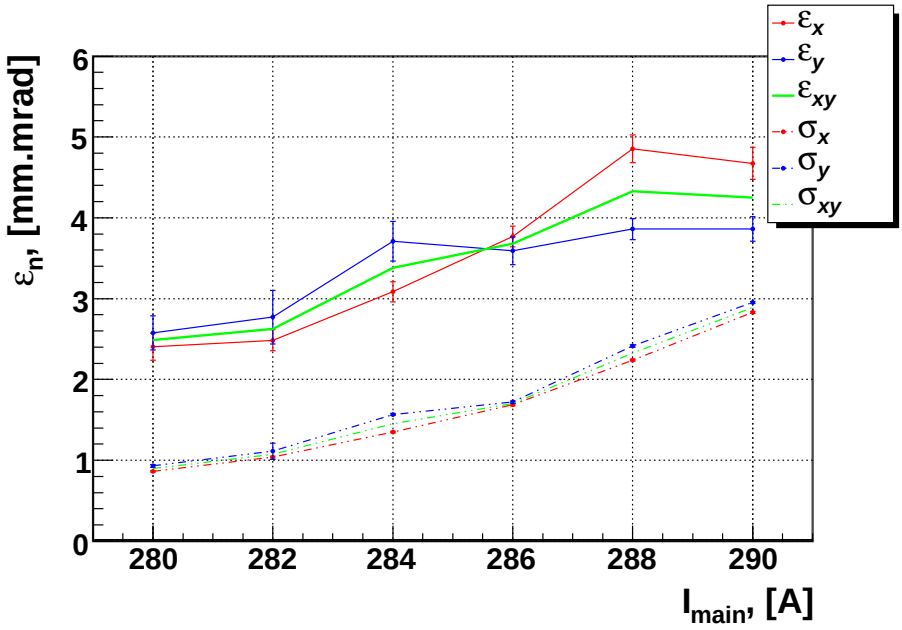

(a) EMSY2, $\phi_b = -15\ deg$

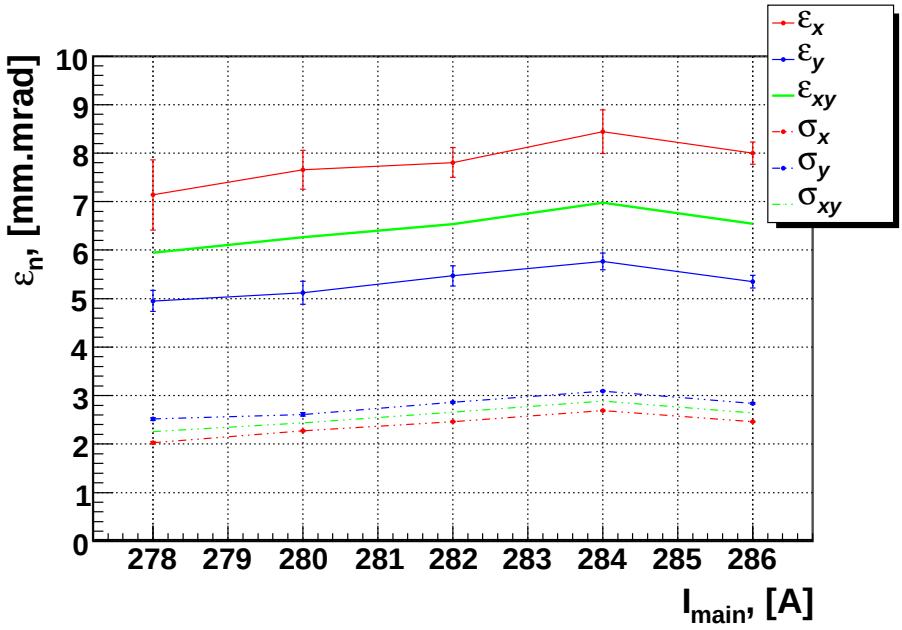

(b) EMSY3, $\phi_b = -15\ deg$

Figure 6.11: Measurement of the emittance at EMSY2 (6.6 m) and EMSY3 (9.9 m) as a function of the solenoid focusing strength, $\phi_g = -2\ deg$. The rms beam size is shown in mm (open circles).

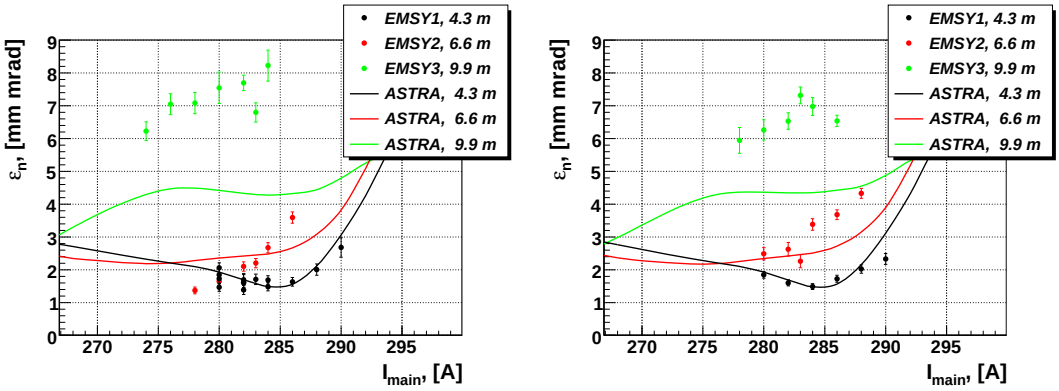

(a) $\phi_{booster} = -10\ deg$ (b) $\phi_{booster} = -15\ deg$

Figure 6.12: Measurement and simulations of the emittance as a function of the current in the main solenoid at the three locations where EMSYs are installed. Gun at 41.85 MV/m and booster phase with respect to the maximum acceleration phase is -10 and -15 deg.

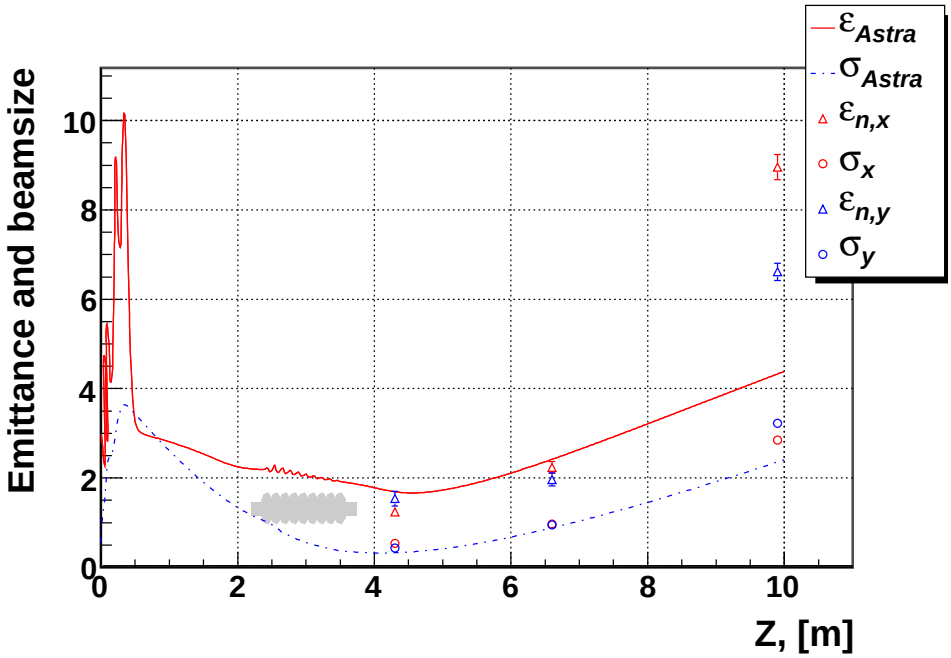

Figure 6.13: Emittance as a function of the distance to the cathode, measurements and simulation at $\phi_b = -10\ deg$, $\phi_g = -2\ deg$, $I_{main} = 282\ A$.

Limitations due to machine aperture

For historical reasons, some of the diagnostic components in the low energy section of PITZ resemble some of the diagnostic components installed at FLASH, such as the Low Energy Dispersive Arm (LEDA) installed at PITZ 1.0 m

downstream the cathode. Following the requirements for the dynamic range of the momentum measurements in LEDA and the size of the dipole magnet, the opening of the vacuum chamber for the magnet is $\sim 12\ mm$, being the narrowest section of the beamline. Due to this limitation in the machine aperture, the minimum of emittance with respect to the solenoid current could not be demonstrated for EMSY2 and EMSY3, which require lower solenoid currents. At such low solenoid settings the beam interacts with the walls of the narrow chamber, thus producing mirror charge that perturb the phase space of the beam, resulting in the peculiar shape shown on figure 6.14(e).

Beside the narrow aperture at LEDA there are other suspicious in-vacuum components that could do possible damage to the quality of the beam. It was shown in [28] that the vacuum mirror of the cathode laser also can contribute to a distortion of the phase space quality.

Another possible reason for deteriorating the quality of the beam phase space could be a mechanical misalignment of the vacuum chamber of the Double Diagnostics Cross (DDC), installed at $0.7\ m$ downstream the cathode.

On figure 6.14(a) a simulation with ASTRA is shown where the beam diameter at the position where the dipole magnet is installed is given for different values of the solenoid focusing strength. As beam diameter the distance between the leftmost to the rightmost particle is taken. One can see that below $282\ A$ parts of the beam are truncated in the walls of the dipole chamber producing an image charge potential that deforms the beam. The measurement of the charge against the solenoid current is shown on figure 6.14(b). It is done with ICTs at two different positions downstream the cathode, Low.ICT1 located at $0.935\ m$ and High1.ICT1 located at $4.2\ m$ downstream. Whereas, the transmission loss at high solenoid currents is due to overfocusing, the charge loss at low solenoid currents is due to the electrons scattered in the walls of the LEDA vacuum chamber.

On figure 6.14(c) an ASTRA simulation of the transverse beam distribution at a distance of $1\ m$ downstream the cathode is shown together with the aperture at LEDA. A comparison between the beam transverse distribution as observed on the screen at position $z = 9.9\ m$ and an ASTRA simulation at the same distance from the cathode is shown on figures 6.14(e) and 6.14(d). It can be seen that although the beam has similar dimensions both as rms values and span (left- to rightmost) the measured distribution is strongly affected by

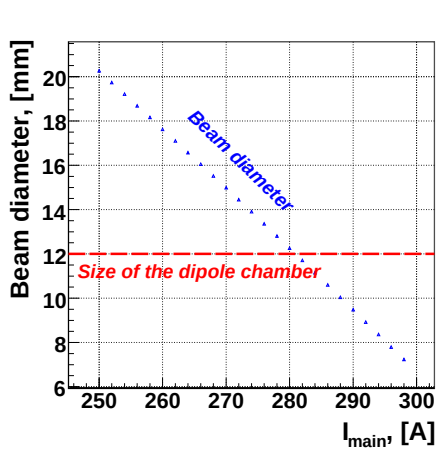

(a) aperture at $z = 1.0\ m$ (LEDA)

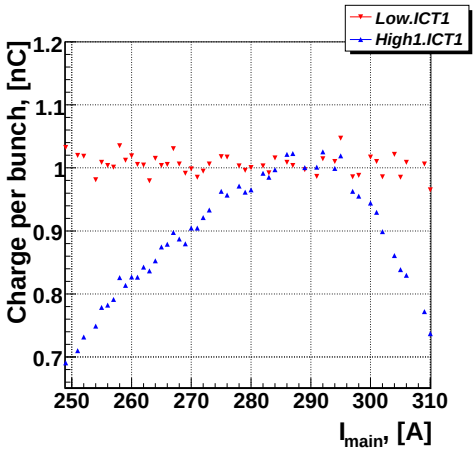

(b) charge transmission

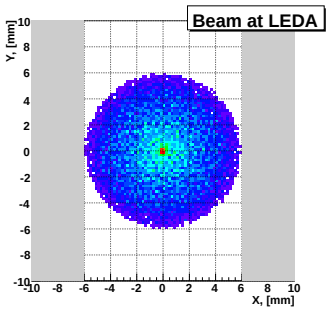

(c) ASTRA simulation, $z = 1.0\ m$ (LEDA), $I_{main} = 282\ A$

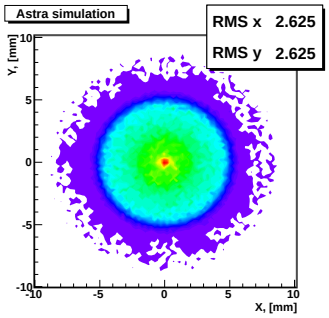

(d) ASTRA simulation, $z = 9.9\ m$ (EMSY3), $I_{main} = 282\ A$

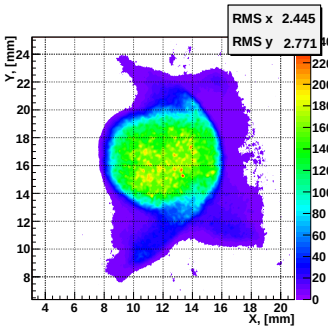

(e) beam measured on screen at EMSY3, $I_{main} = 282\ A$

Figure 6.14: The effect on the beam distribution from the aperture at $z = 1.0$. The phase of the gun is $\phi_g = -2$, booster phase was set to $\phi_b = -10\ deg$.

some wake field whose orientation coincides with the orientation of the dipole chamber and the vacuum mirror (upward).

It is obvious that no reasonable measurements can be made at solenoid focusing strength below 280 A.

Detailed scan of the local divergence

A detailed scan of the local divergence distribution across the beam was done with the single slit for direct reconstruction of the phase space distribution in the horizontal plane. The result is shown on figure 6.15.

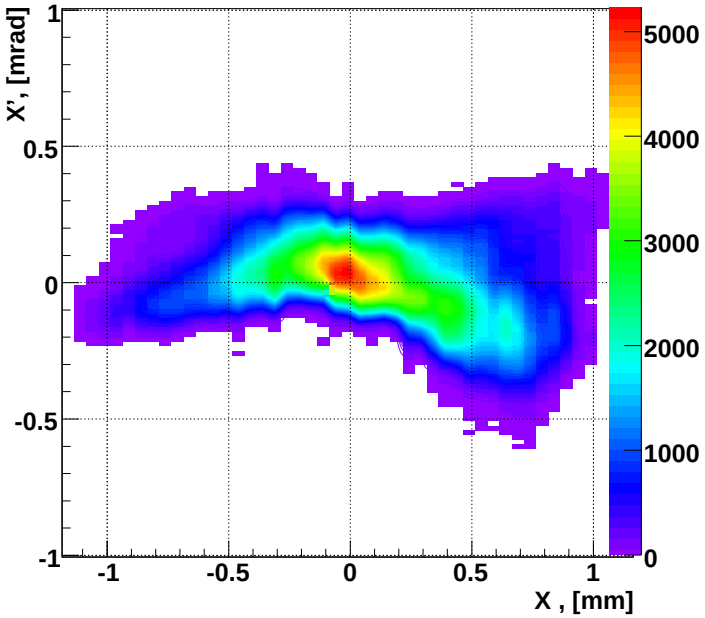

Figure 6.15: Horizontal phase space distribution at EMSY1, gun3.1 at 40 MV/m, $P = 12.99\ MeV/c$, $I_{main} = 282\ A$, RF phases $\phi_{gun} = -2,\ \phi_b = -10\ deg.$

Emittance measurements gun 3.1 summarized

The emittance measurement system using the 10 μm slit was successfully employed. Emittance was measured for maximum accelerating gradient of about 42 MV/m. The lowest emittance measured with gun 3.1 in the horizontal plane was $1.32 \pm 0.11\ mm \cdot mrad$ and in the vertical plane $1.43 \pm 0.175\ mm \cdot mrad$ at the following conditions: $I_{main} = 282\ A$, mean momentum from the gun was about 4.94 MeV/c, final momentum after the booster 12.85 MeV/c, accelerating phases -2 and -5 deg and the laser spot size on the cathode (initial beam size) of ~ 0.55 mm. As expected no strong dependence on the phase is visible, and the condition for emittance compensation is found between 282 and 284 A. The measurements at EMSY1 ($z = 4.3\ m$) is in good agreement with the result from the ASTRA simulations, shown on figure 6.8.

Due to problem with the machine aperture, the optimum emittance conditions for EMSY2 and EMSY3 could not be established.

Estimate of the systematic deviation

Using the models described in chapter 5, an estimation of the systematic deviation for the lowest measured emittance was done. As initial conditions for the model, $\sigma_0 = 0.5\ mm,\ \varepsilon_n = 1.37\ mm \cdot mrad$, beam momentum 13 MeV/c and resolution of 30 m^{-1} were used.

The expected systematic deviation is 6.3 % with the 10 μm slit mask. If the 50 μm mask was used it would have been 13.9 %. In the above estimation the contribution of the 8 bit camera is not included. On page 106 a comparison between 8 and 12 bit measurement reveals that the deviation can be about -7 %.

6.4 Emittance results with gun 3.2

Gun 3.2 was installed and conditioned in PITZ in the spring of 2007. The maximum RF power in the cavity was increased up to the limit of the PITZ RF system ($\sim$ 7 MW in the gun). This corresponds to an accelerating gradient[3] of about 60 MV/m or mean beam momentum after the gun up to 6.5 MeV/c. In addition, a new type of camera for beamlets measurement was installed. The new camera was a 12-bit digital Prosilica described in section 3.4.3

In the optimization process the emittance was measured as a function of the cathode laser-spot diameter and the accelerating strength of the booster cavity. Again, the focusing strength of the main solenoid was used as a primary scan parameter and the accelerating gradient of the booster, as a secondary one. After three final beam momenta of 9.5, 11 and 13 MeV/c were measured, the laser spot size on the cathode was changed using the beam shaping aperture (BSA). At the smallest BSA (diameter of 1.2 mm), the emittance was measured also for final mean momentum of 14.5 MeV/c.

All the measurements were made for RF phases corresponding to the maximum acceleration ($\phi_g = 0,\ \phi_b = 0\ deg$). Three different cathodes were used, conventionally called #83, #42 and #34 [70] (in order of the insertion of the cathode into the cavity). A major difficulty during this measurement period was the fast degradation of the cathode's quantum efficiency. For instance the cathode #83 was able to deliver 1 nC with 1.5 mm BSA diameter for

[3] calculation based on the measurements in [27]

about 140 hours. For #34 this time was even shorter since the cathode was already used in the preceeding conditioning period when measurements other than emittance were made. For establishment of the proper compensating condition at each optimization stage (laser diameter and booster momentum gain), the emittance was allways measured as a function of the current in the main solenoid.

However the problem with the narrow machine aperture remained. Therefore, the emittance measurements were made only at the position of EMSY1 (4.3 m).

Measurements using different BSA

Measurements using four different beam shaping aperture (BSA) diameters were made. Each laser BSA was characterized for three final beam momenta ranging from 9.5 up to 14.5 MeV/c. The primary goal of the BSA scan was to establish the best conditions for emittance compensation at accelerating gradient of $\sim$60 MV/m. All the BSAs used for measurement of the transverse emittance are summarized in table 6.6.

The minimum emittance as a function of the initial rms size of the cathode laser is shown on figure 6.6. As can be seen, the minimum lies somewhere between 0.35 and 0.4 mm initial rms size.

Table 6.6: Size of the laser spot on the cathode used for the emittance measurements with gun 3.2. The notation of BSA (first column) corresponds to the BSA diameter size (given in the second column). The third column is the rms size measured at the position of the virtual cathode (VC), where VC is installed next to the gun cavity along an equivalent optical path to the real cathode.

notation	**diameter, [mm]**	σ_{ini}**, [mm]**
BSA2	2.0	0.56
BSA18	1.8	0.50
BSA15	1.5	0.40
BSA12	1.2	0.36

On figure 6.16 a measurement of the emittance as a function of the solenoid current is shown for the case of BSA2. The measured mean momentum after

the gun cavity was 6.48 MeV/c, the minimum geometrical average emittance of 1.61±0.08 $mm \cdot mrad$ is located at a final mean momentum of 13.2 MeV/c and a solenoid current of $I_{main} \simeq 367\ A$.

The next BSA used (BSA18) delivered higher value for the measured emittance. The smallest emittance of 1.79±0.09 was measured at a final beam momentum of 11 MeV/c and $I_{main} = 368\ A$, where the mean momentum after the gun was 6.5 MeV/c. The result is shown on figure 6.17.

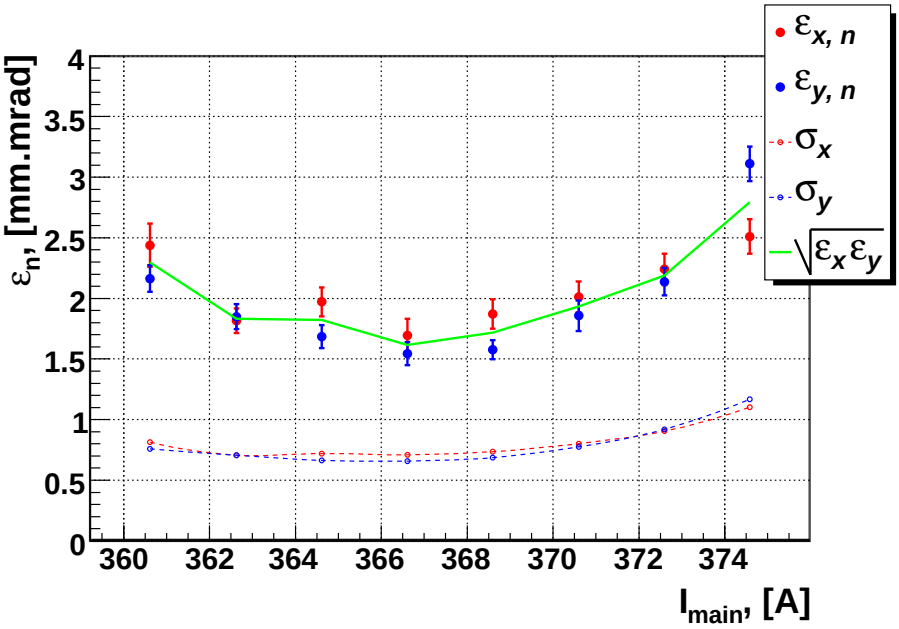

Figure 6.16: Emittance as a function of the main solenoid focusing strength for gun 3.2. BSA2 was used and mean momentum after the booster was 13.2 MeV/c. The doted lines show rms beamsize in mm.

Measurements with BSA15 resulted in a minimum emittance of 1.38±0.09 $mm \cdot mrad$ at $I_{main} = 371\ A$ (figure 6.18). The momentum gain from the gun was 6.4 MeV/c, and final mean momentum after the booster 13 MeV/c.

BSA15 corresponds to initial rms size of about 0.4 mm which is close to the location of the simulated minimum of emittance as a function of the initial rms size (see figure 6.6). The measurement of the emittance for BSA12 (with $\sigma_{ini} \sim 0.36\ mm$) revealed further decrease of the emittance to 1.27±0.16 $mm \cdot mrad$ (see figure 6.19), measured at $I_{main} = 373\ A$, with mean momentum after the gun of 6.47 MeV/c and a final beam momentum of 14.46 MeV/c.

All the results from emittance measurements as a function of the BSA di-

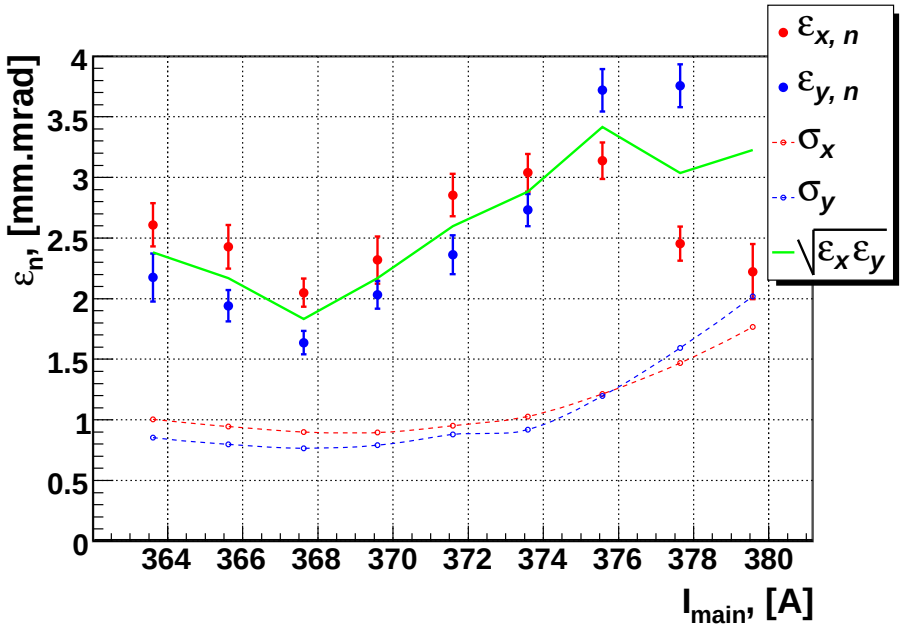

Figure 6.17: Emittance as a function of the main solenoid focusing strength for gun 3.2. BSA18 was used and mean momentum after the booster was 11 MeV/c. The doted lines show rms beamsize in mm.

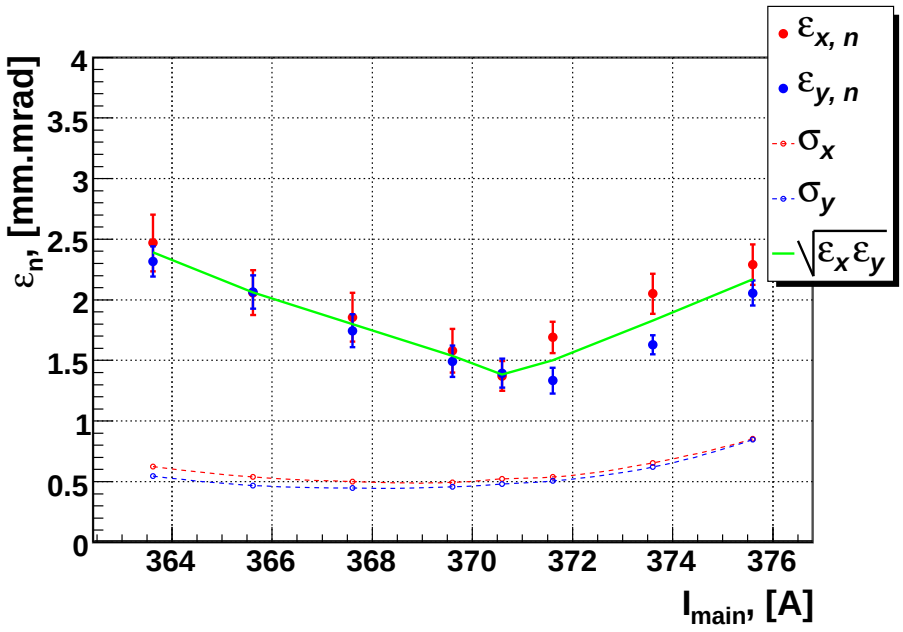

Figure 6.18: Emittance as a function of the main solenoid focusing strength for gun 3.2. BSA15 was used and mean momentum after the booster was 13 MeV/c. The doted lines show rms beamsize in mm.

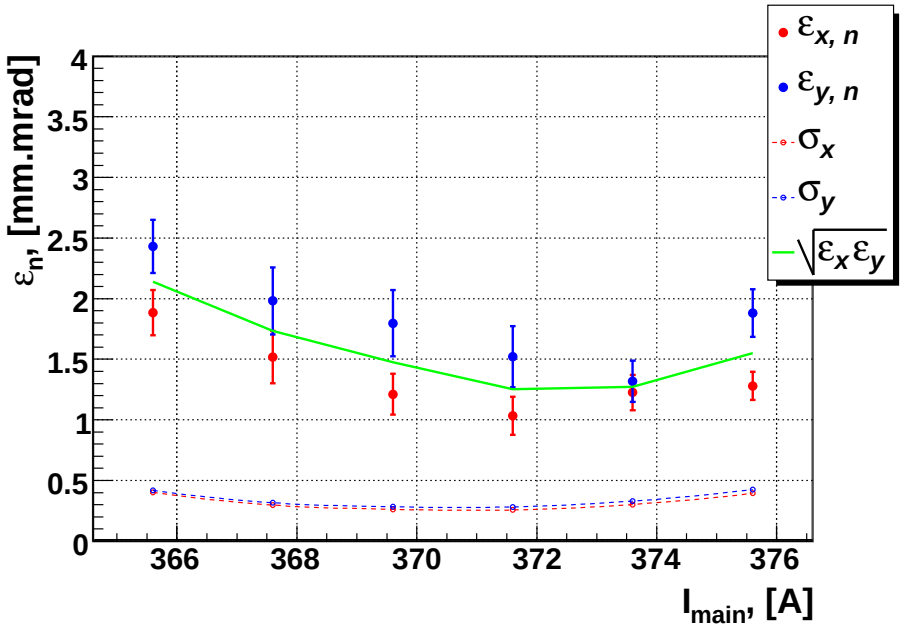

Figure 6.19: Emittance as a function of the main solenoid focusing strength for gun 3.2. BSA12 was used and mean momentum after the booster was 14.46 MeV/c. The doted lines show rms beamsize in mm.

ameter are summarized in table 6.7, and the error bars shown on the table and on the plots is the statistical uncertainty due to fluctuation of the measured values and does not include the systematic uncertainty discussed in chapter 5. Emittance measurements for smaller BSA diameters were not possible, due to the fast degradation of the cathode's quantum efficiency.

Table 6.7: Beam shaping apertures used for the emittance measurements with gun 3.2.

BSA, $[mm]$	ε_{xy}, $[mm \cdot mrad]$	**momentum,** $[MeV/c]$	$I_{main}, [A]$
2.0	1.61±0.082	13.2	367
1.8	1.79±0.088	11.0	367
1.5	1.38±0.086	13.0	371
1.2	1.27±0.155	14.5	373

The best resulting emittance as a function of the initial rms size σ_{ini} is plotted together with the results from ASTRA simulations on figure 6.20. To reveal the discrepancies, thorough analysis of the data was made. It turned out

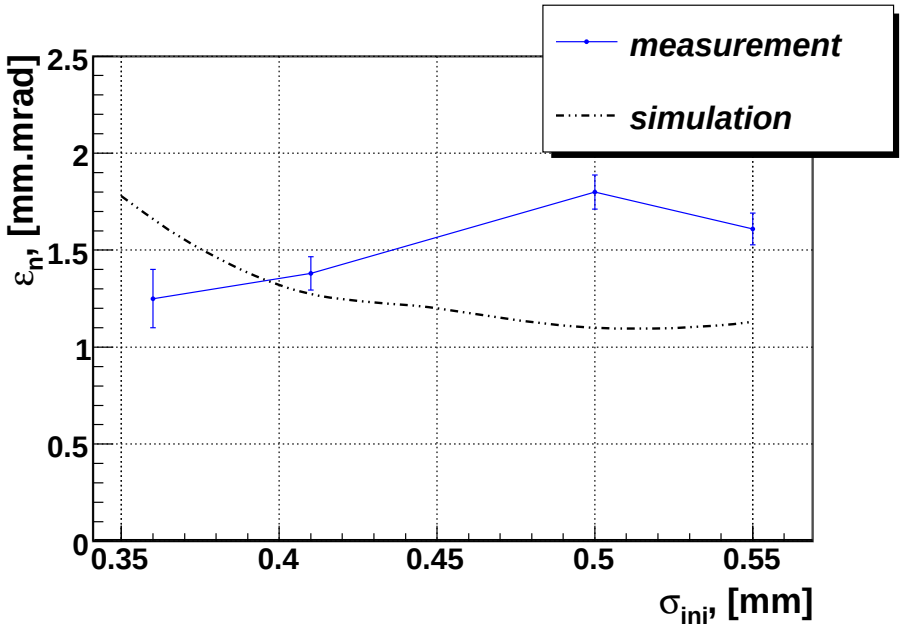

Figure 6.20: Minimum of emittance as a function of the initial rms size at the cathode.

that the beamlet intensity for BSA2 does not always cover the requirements for data consistency. More specifically, the beamlet intensity reaches maximum values of up to 2100 (out of 4095) this corresponds to signal to noise ratio of 12 and brings systematic underestimation of the divergence of about 8 %. Unfortunately, due to time restrictions we were not able to repeat the measurements at 2 mm diameter of the BSA. Still the decrease of the measured emittance at lower aperture is not in agreement with the ASTRA simulations.

Measurements with different final beam mean momentum

The energy gain from the booster cavity was varied such that the final beam momentum was tuned to 9.5, 11.0, 13.0 and 14.5 MeV/c by changing only the gradient in the booster cavity. Limitations in the capacity of the booster water regulation system restricted the maximum momentum of the beam in this range. After complete scan against the momentum gain was performed, the BSA was replaced with a different one following the direction in which the minimum emittance is expected. The minimum values of the emittance were measured with BSA diameter of 1.2 mm, for all final beam momenta except at 9.5 MeV/c. The minimum value at this momentum was measured with

BSA diameter of 2 mm. Due to time limitation, we were unable to measure emittance with BSA12 at 9.5 MeV/c. The results from the emittance measurements against the final beam momentum are summarized in figure 6.21. A summary of the emittance measurements against the beam momentum is

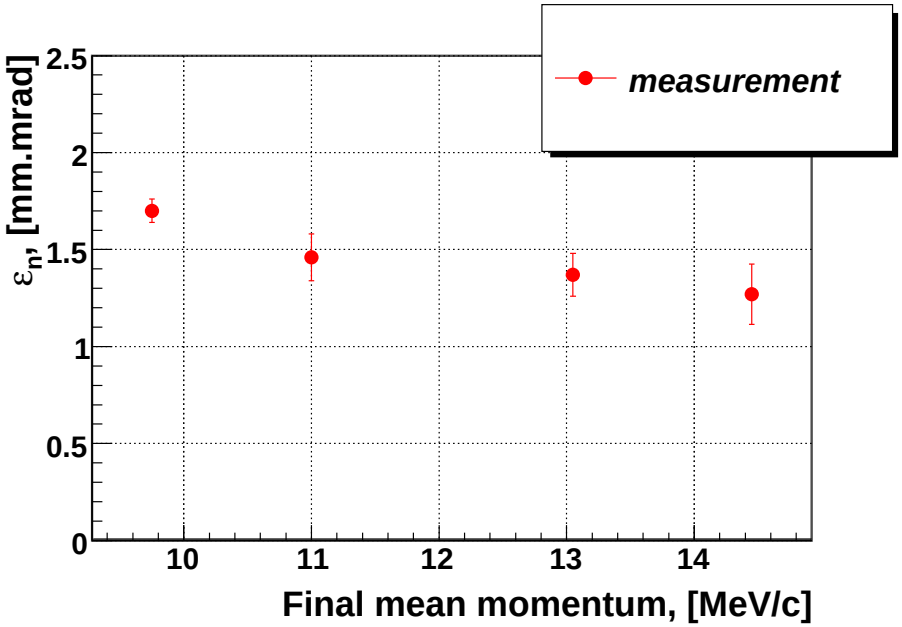

Figure 6.21: Emittance as a function of the momentum gain from the booster cavity.

given in table 6.8.

Table 6.8: Minimum of the emittance for different booster momentum gain.

Final momentum, $[MeV/c]$	ε_{xy}**,** $[mm \cdot mrad]$	I_{main}, $[A]$
9.75	1.70±0.06	363
11.00	1.46±0.12	372
13.05	1.37±0.11	371
14.46	1.27±0.16	373

The lowest emittance was measured with BSA12 and final beam momentum of 14.5 MeV/c. This result is shown on figure 6.19. The region with the lowest beam emittance was re-measured for the corresponding machine parameters: $P = 14.46$ MeV/c, I_{main} in the range $372 - -376$ A, rms laser spot size on the cathode 0.35 mm. A very good reproducibility of about 2-3% has

been demonstrated. The smallest measured emittance together with repeated measurements around the minimum are shown on figure 6.22.

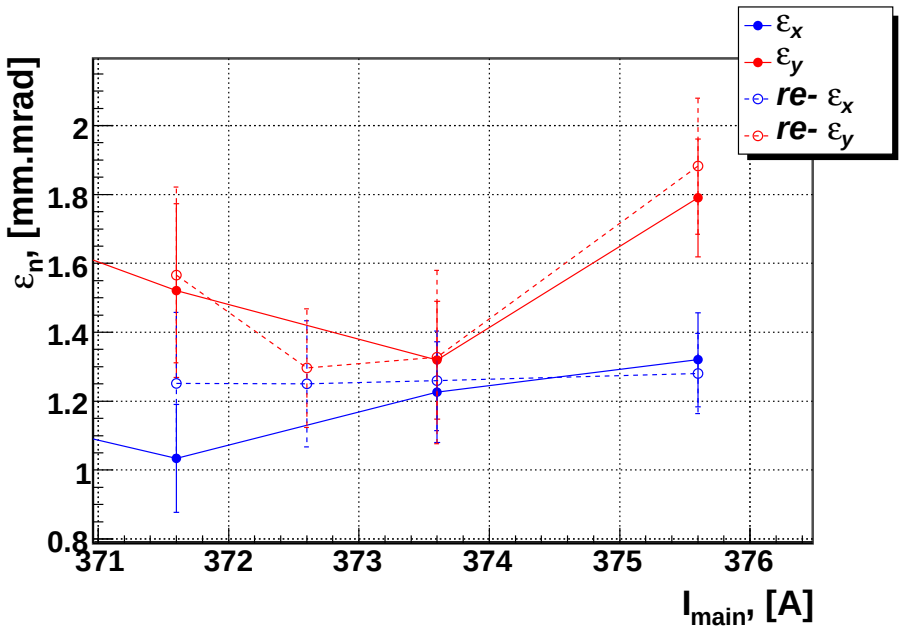

Figure 6.22: Reproducibility of the emittance measurements around the minimum emittance. BSA12, final momentum 14.46 MeV/c.

Estimate of the systematic deviation

Using the model described in chapter 5, an estimation of the systematic deviation for the lowest measured emittance was done. On figure 6.23 the evolution of the beamlet size is shown together with a measured one. As initial conditions for the model, $\sigma_0 = 0.3\ mm$, $\varepsilon_n = 1.25\ mm \cdot mrad$, beam momentum 14.46 MeV/c and resolution of 30 m^{-1} were used. One can see a very good agreement between the beamlet size measured with the 10 μm slit mask and the estimated beamlet size. The beamlet size was measured in the center of the distribution, the error bars are the statistical fluctuations.

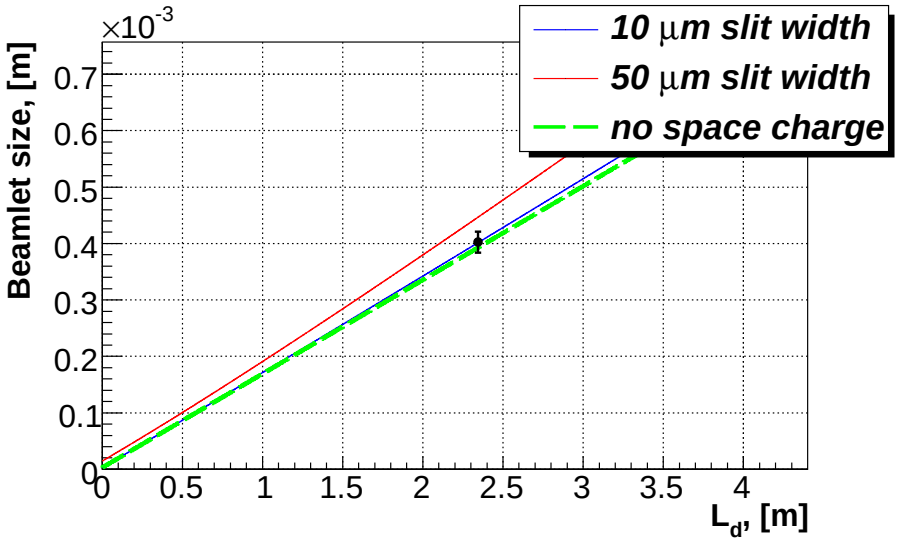

Figure 6.23: Comparison between the measured beamlet size (black dot with error bar) and the beamlet size evolution estimated using the model in chapter 5.

The expected systematic deviation is 5.6 % with the 10 μm slit mask and 13.6 % if the 50 μm slit mask was used. This leads us to the following expression for the measurement uncertainty, ε_x=$1.25^{+0.02}_{-0.07}\pm 0.155\ mm \cdot mrad$. Where the first number is the measured value, the second pair of numbers is the systematic deviation and the last number representing the statistical fluctuation of the measured value.

Detailed scans with the slit

A detailed scan with the single slit using as small as 25 μm separation between the individual slit positions has been performed for detailed reconstruction of

the phase space distribution. The phase space distribution for the minimum measured emittance is shown on Fig. 6.24.

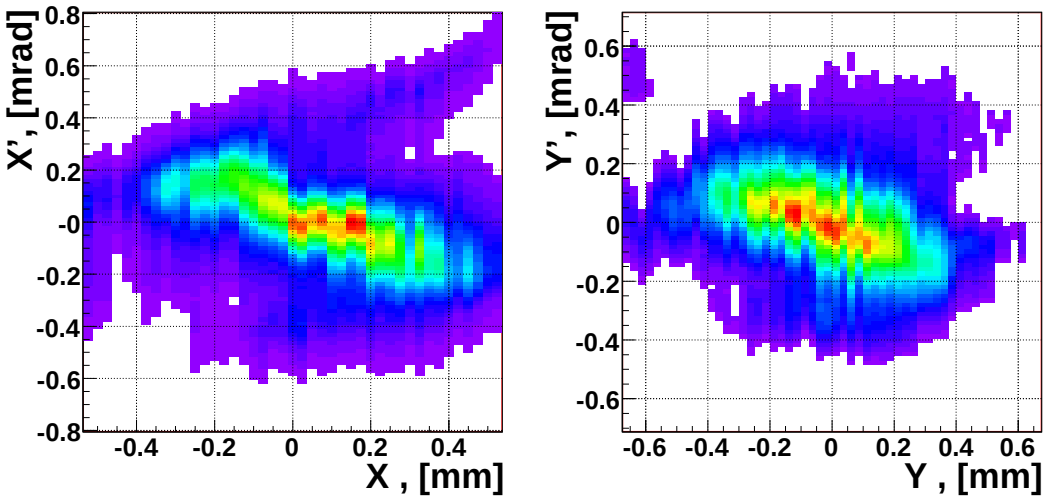

(a) phase space, X plane

(b) phase space, Y plane

Figure 6.24: Phase space distribution at $P = 14.46$ MeV/c, $I_{main} = 373$ A, on crest phases of gun and booster.

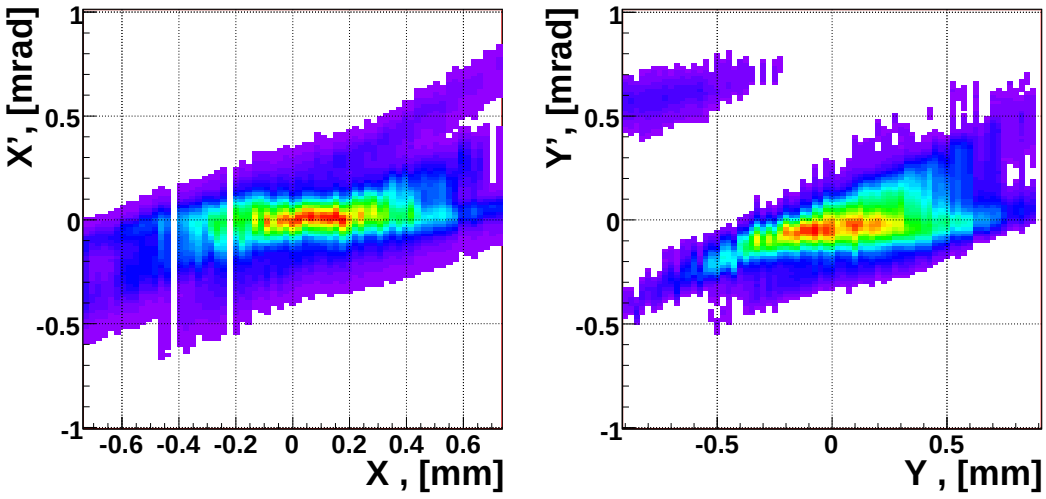

(a) phase space, X plane

(b) phase space, Y plane

Figure 6.25: Phase space distribution at $P = 14.46$ MeV/c, $I_{main} = 376$ A, on crest phases of gun and booster.

Figures 6.25 show another example of a detailed scans using the single slit for different beam momentum and solenoid focusing strength. This detailed scan using a single slit reveals a strange formation in the vertical phase space (see figure 6.25(b)). This points out that a fraction of the beam (about 5%) has different flight direction than the rest. For the case shown on figure 6.25(b), this formation is also visible in the transverse distribution (x, y) of the beam on the screen, where the slit scan was performed (see figure 6.26). One can see a fraction of the beam approximately at position $z = 4.3\ m$ with screen coordinates $X = 14.6\ mm$ and $Y = 17.2\ mm$ that is even further separated from the beam on the next screen at position $z = 6.6\ m$ (screen coordinates $X = 13.8\ mm$ and $Y = 17.1\ mm$).

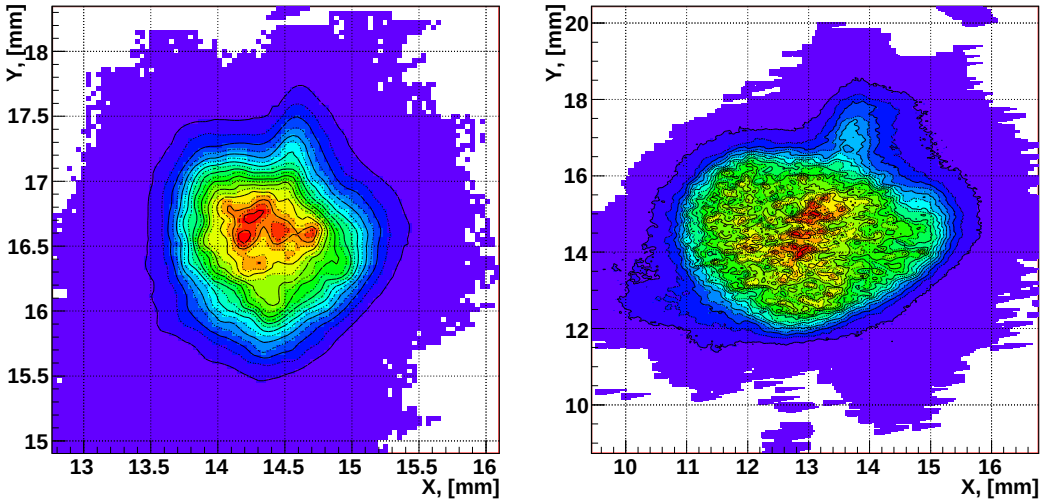

(a) $z = 4.3\ m$ (b) $z = 6.6\ m$

Figure 6.26: Beam distribution on the screen at the slit position (a) and on the beamlet observational screen (b), $P = 14.46$ MeV/c, $I_{main} = 376$ A, on crest phases of gun and booster.

6.5 Comparison between gun 3.1 and gun 3.2 at 40 MV/m

The conditions from the measurement with the lowest emittance from gun 3.1 were reproduced also with gun 3.2 after it was conditioned to 60 MV/m. The comparison between the two cavities is shown on Fig. 6.27. Altough there is agreement within the error bars between the minimum values, $\varepsilon_{n,3.1} = 1.37 \pm 0.1$, $\varepsilon_{n,3.2} = 1.54 \pm 0.11$, there is obviously large discrepancy between the minimum position with respect to I_{main} of about 8 A. This large discrepancy is still to be understood. It must be noted that small changes in the max-

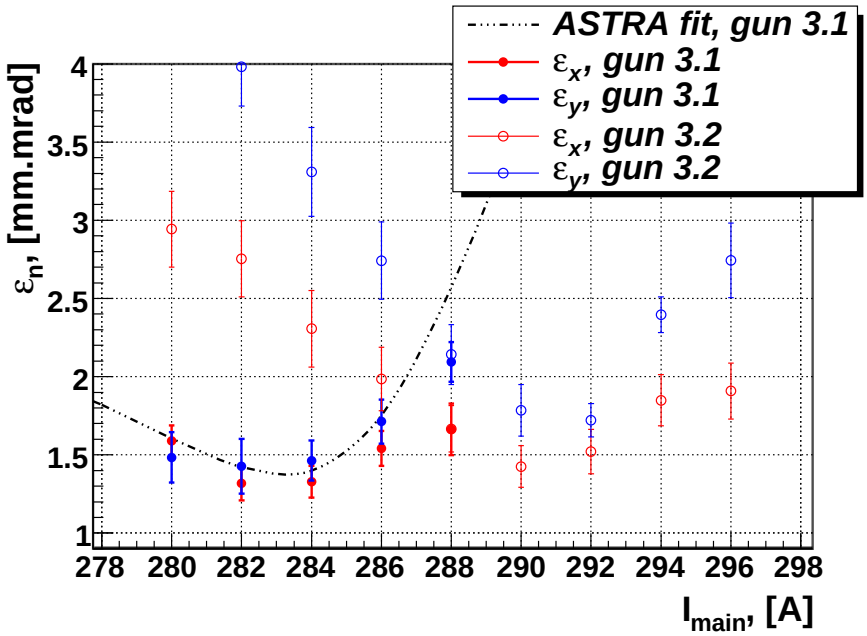

Figure 6.27: Comparison of the measurement with gun 3.1 and gun 3.2 as well as with ASTRA simulations for the gun 3.1 case. The machine was set to have the same mean momentum at about 40 MV/m, booster phase with respect to the maximum acceleration phase is -5 deg, initial beamsize is 0.55 mm.

imum accelerating gradient can bring shift in the position of the emittance minimum. Altough the beam momentum after the gun cavity was kept the same ($\sim 4.94\ MeV/c$), the beam dynamics in the RF gun strongly depends on the form of the field distribution inside the cavity. This partially could explain the difference in the position of the emittance minimum. However a remeasurement of the field profile of gun 3.1 after dismounting did not show

big discrepancy.

One must remember that the measurements done in 2006 were performed using 8 bit JAI camera where in 2007 it was a 12 bit. The rescaling of the 12 bit data to 8 bit resulted in $\varepsilon_{n,3.2} = 1.41 \pm 0.11\ mm \cdot mrad$ which is in better agreement with the minimum value measured with gun 3.1. Still this can not explain the difference in I_{main}. The difference between the measurement with a 12 bit camera and the result rescaled to 8 bit (about 7 %), is used as systematic deviation for the case of measurements done with the 8 bit camera.

Chapter 7

Core emittance for gun 3.2

7.1 Emittance for different charge contours

For some applications of electron beams, it is better suitable to consider the projected normalized rms emittance of a smaller fraction of the total phase space distribution. In such cases, only that signal is considered, which is inside a equidensity contour surrounding an appropriate fraction of the whole charge. The calculations are done in the same manner as for the full beam emittance. On figures 7.1 (I_{main} = 373 A) and 7.2 (I_{main} = 376 A), an example for three equidensity contours in the phase space are shown.

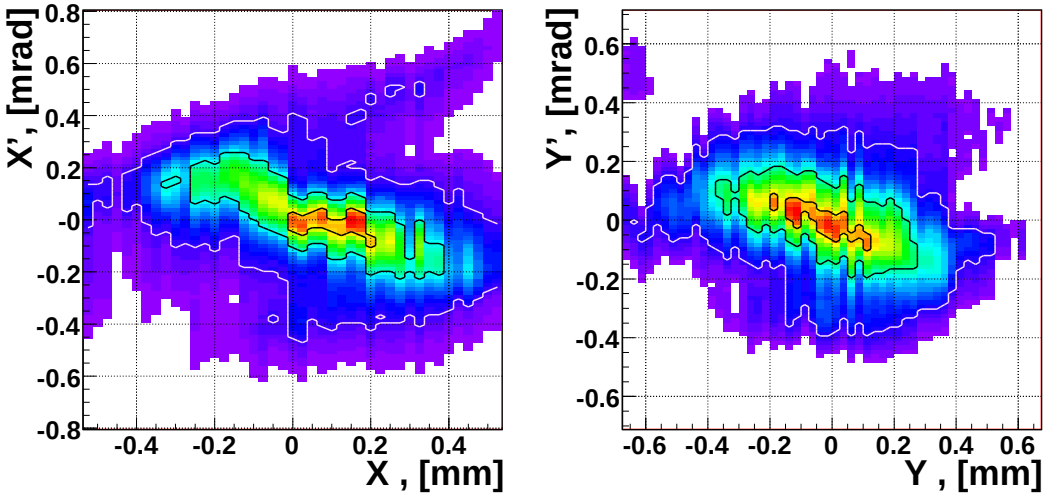

(a) phase space, X plane

(b) phase space, Y plane

Figure 7.1: Phase space distribution shown on figures 6.24, I_{main} = 373 A. The contours surrounding 90, 50 and 10 % from the charge are shown.

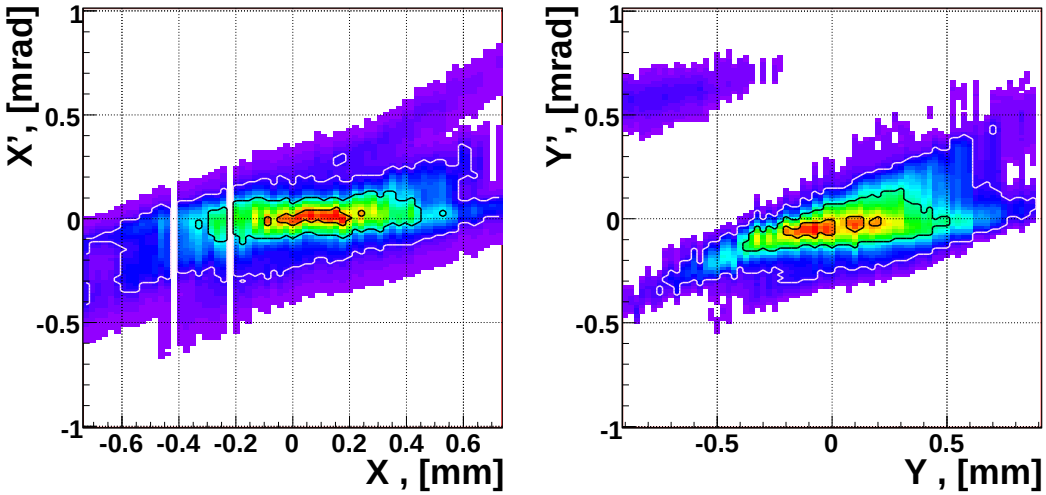

(a) phase space, X plane

(b) phase space, Y plane

Figure 7.2: Phase space distribution shown on figure 6.25, I_{main} = 376 A. The contours surrounding 90, 50 and 10 % from the charge are shown.

The resulting emittance inside the contours is given in table 7.1 and summarized as reduction in percent in table 7.2. One can see that when only 10 % of the charge is removed the emittance is reduced by more than 25 %.

Table 7.1: Emittance in the equidensity contours surrounding 90, 50 and 10 % of the total charge. Emittance values are in $mm \cdot mrad$.

Charge, [%]	$\varepsilon_x^{373\ A}$	$\varepsilon_y^{373\ A}$	$\varepsilon_x^{376\ A}$	$\varepsilon_y^{376\ A}$
100	1.27	1.29	1.28	1.88
90	0.912	0.968	0.954	0.995
50	0.336	0.373	0.316	0.377
10	0.068	0.081	0.057	0.076

Table 7.2: Emittance reduction in percent for different charge cut of 90, 50 and 10 % from the total charge.

Charge, [%]	$\Delta\varepsilon_x^{373\ A}$	$\Delta\varepsilon_y^{373\ A}$	$\Delta\varepsilon_x^{376\ A}$	$\Delta\varepsilon_y^{376\ A}$
100	0	0	0	0
90	28.1	25.1	28.3	47.1
50	73.5	71.1	76.3	79.9
10	94.6	93.7	95.7	96

7.2 Core emittance at PITZ

The emittance as a function of the charge in the equidensity contours reveals important characteristic of the phase space distribution, namely the *core emittance*. Usually the beams are characterized with two types of core emittance, ε_c and $\varepsilon_{c,90\%}$ [47]. The core emittance is defined as the value of the tangent to the origin of the function at full charge ε_c or at 90 % of the charge $\varepsilon_{c,90\%}$. On figures 7.3 the emittance is plotted as a function of the charge in the contour for the phase space distributions shown on figure 7.1.

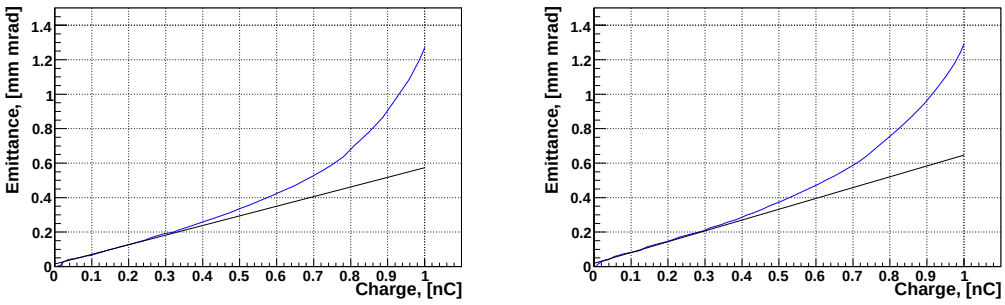

(a) X plane (b) Y plane

Figure 7.3: Emittance as a function of the charge in a contour (blue) and the core emittance (black). $I_{main} = 373\ A$.

As a tangent, a linear fit in the range from 0.05 to 0.2 nC is used. The core emittance values are as follows: $\varepsilon_{c,x} = 0.587$, $\varepsilon_{c,y} = 0.664\ mm \cdot mrad$.

The same is shown on figures 7.4, for the distribution on figure 7.2. The core emittance values in this case are: $\varepsilon_{c,x} = 0.507$, $\varepsilon_{c,y} = 0.606\ mm \cdot mrad$ slightly lower than for the case of figure 7.1, despite the fact that the

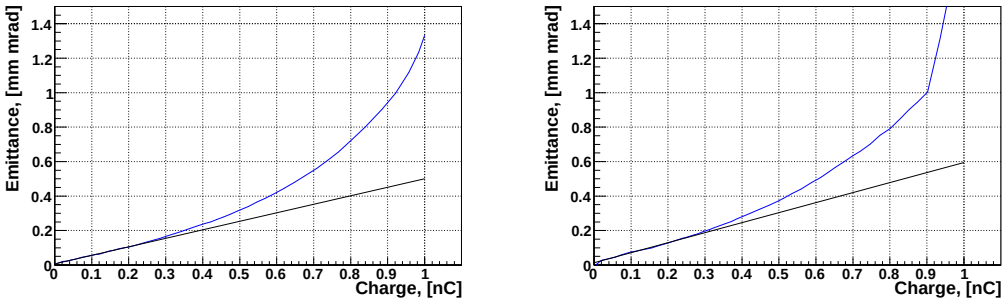

(a) X plane

(b) Y plane

Figure 7.4: Emittance as a function of the charge in a contour (blue) and the core emittance (black). $I_{main} = 376\ A$.

projected emittance for the full beam is higher.

Due to technical reasons the same analysis of the emittance as a function of the charge in equidensity contours could not be made for gun 3.1.

Chapter 8

Different charge schemes

As nominal operating mode of the XFEL bunch charge of 1 nC is considered. However some FEL applications may require beams with special properties i.e. extremely short pulse length ($\leq 10\ fs$). Achieving this might be impossible with a bunch charge of 1 nC.

The main effects degrading the beam quality during the pulse length compression are the space charge forces, wake field and coherent synchrotron radiation (CSR) effects. While the first two are scaling linearly with the charge, the CSR effects are proportional to N^2 where N is the number of the particles involved in the interaction. In addition operation at low charge allows short pulse length which is reducing the influence from the RF curvature in the accelerating cavities.

In this appendix an extended optimization of the PITZ photo-injector is made for bunch charges of 0.07, 0.2, 0.5 and 1.0 nC. Later estimation of the emittance measurement system at the optimized points is given.

8.1 photo-injector optimization for different bunch charges

The optimization was done using the SWARM algorithm (see page 77) and ASTRA. During the SWARM search 20000 macro particles were used, the obtained optimum was repeated with 200000 macro particles. Minimum of the transverse projected emittance for bunch charges of 0.07, 0.2, 0.5 and 1.0 nC was investigated for two different booster cavities, one is a standard TESLA

type used for the measurements shown previously, and the other is Cut Disc Structure (CDS). Installation of the CDS booster is foreseen for the middle of 2009.

In table 8.1 the ranges of the parameters used for optimization are given[1].

Table 8.1: Optimization parameters.

parameter	range		
	min	max	unit
σ_{ini}	0.07	0.65	[mm]
ϕ_g	-5	5	[deg]
I_{main}	330	410	[A]
E_{acc}	3	30	[MV/m]
$Z_{booster}$	2	6	[m]
Z_{min}	–	10	[m]

The maximum accelerating gradient of the gun was fixed at 60 MV/m, the field ballance was 1.1. As longitudinal laser distribution a flat top with FWHM of 20 ps and 2 ps rise and fall time. The initial kinetic energy of the electrons was 0.5 eV. The phase of the booster was fixed to -4 deg, which correspond to the minimum momentum spread at bunch charge of 1 nC. The location of the minimum was searched from 0.2 m after the exit of the booster up to 10 m downstream the cathode.

The optimized parameters for the TESLA booster are summarized in table 8.2 and for the CDS booster in table 8.3. The lower four rows are presenting the emittance resulting from a simulations with 200000 particles. They are as follows: final mean kinetic energy, the peak current and the beam rms size at the position of the minimum. These four parameters were used to estimate the systematic deviation of a measurement when the existing EMSY is used.

[1]The only difference between the search parameters for the TESLA and the CDS cavities is the maximum accelerating gradient which for TESLA was up to 16 MV/m.

Table 8.2: Optimum parameters and resulting emittance for the case of TESLA booster.

parameter	charge				unit
	0.07	0.2	0.5	1.0	$[nC]$
σ_{ini}	0.09	0.174	0.313	0.494	$[mm]$
ϕ_g	2	1.2	1.2	2.4	$[deg]$
I_{main}	371	375	376	383	$[A]$
E_{acc}	13.7	15.8	16	14.65	$[MV/m]$
$Z_{booster}$	5.9	4.8	4.5	3.3	$[m]$
Z_{min}	10.7	8.77	8.63	4.93	$[m]$
result					
ε_n	0.102	0.209	0.429	0.714	$[mm \cdot mrad]$
E_k	13.55	14.72	14.78	14.05	$[MeV]$
I_p	4.2	11.5	27.2	53.3	$[A]$
σ_0	0.383	0.419	0.981	0.699	$[mm]$

Table 8.3: Optimum parameters and resulting emittance for the case of CDS booster.

parameter	charge				unit
	0.07	0.2	0.5	1.0	$[nC]$
σ_{ini}	0.116	0.187	0.320	0.446	$[mm]$
ϕ_g	1.7	-0.6	0.5	-0.5	$[deg]$
I_{main}	371	376	377	380	$[A]$
E_{acc}	3.7	18.2	21.3	22.3	$[MV/m]$
$Z_{booster}$	2	4.1	4.1	3.5	$[m]$
Z_{min}	7.24	9.23	11.0	9.11	$[m]$
result					
ε_n	0.123	0.219	0.368	0.618	$[mm \cdot mrad]$
E_k	9.37	22.19	24.86	26.78	$[MeV]$
I_p	4.2	12	27.5	51.3	$[A]$
σ_0	0.206	0.329	0.585	0.723	$[mm]$

8.2 Performance estimation of the single slit measurement

The performance of the measurement system was estimated using the models described in chapter 5. The influence of the space charge, the initial slit opening and finite optical resolution were all considered. As optical resolution 50 $lines/mm$ was used. The calculation was done for maximum drift length L_d of 4 m.

In table 8.4 the minimum of the estimated systematic deviation $\Delta\varepsilon_{min}$ of a measurement with the 10 μm slit is given in %, together with the drift length L_d^{min} in $[m]$ at which this minimum occurred.

Table 8.4: Emittance and systematic deviation in percent for the optimized parameters.

charge, $[nC]$	TESLA			CDS		
	ε_n	$\Delta\varepsilon_{min}$	L_d^{min}	ε_n	$\Delta\varepsilon_{min}$	L_d^{min}
0.07	0.102	17.4	4	0.123	13.7	2.53
0.2	0.209	11.7	4	0.219	10.2	4
0.5	0.429	11.5	4	0.368	12.7	4
1.0	0.714	6.9	4	0.618	11.5	4

It is observed that except for one case, in all others L_d^{min} is allways at 4 m. The systematic deviation of the emittance measurement with initial conditions same as the case of 1 nC and CDS booster is shown on figure 8.1 as a function of the drift length. The red line represents the case of 50 μm slit opening, the blue is showing 10 μm opening and green is again for 10 μm slit but the beamlet current was set to zero, in order to estimate the influence of the optical resolution and the initial slit opening independent on the space charge.

One can see that the influence of the space charge is negligible with respect to the other two effects. In this case in order to have lower systematic deviation it is feasible to increase the resolution of the beamlet size measurement and to subtract the initial beamlet size in order to exclude the influence of the finite slit opening. The emittance measurement uncertainty in this case will increase because it will include the statistical uncertainty together with the uncertainty of the slit opening. The slit opening can be measured with

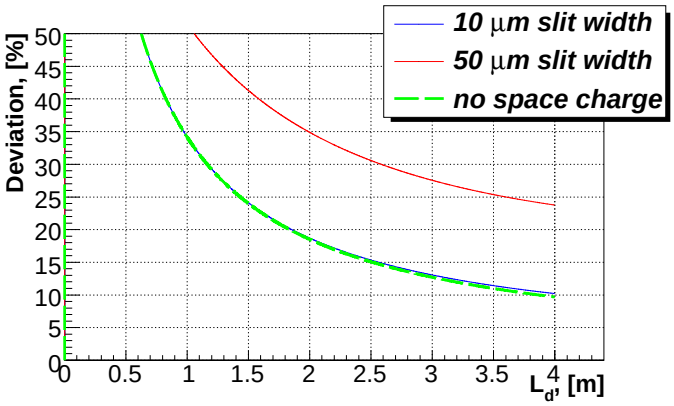

Figure 8.1: Evolution of the systematic deviation downstream the slit mask. The initial conditions are as the case of 1 nC and CDS booster.

precission better than 1 μm. Therefore it will play a significant role if the beamlet size is smaller than 15 μm.

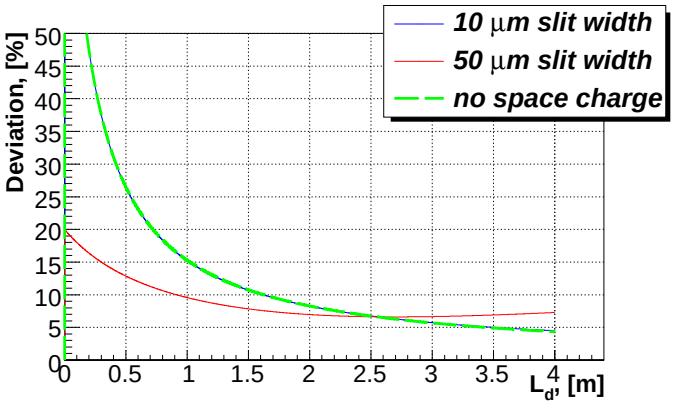

Figure 8.2: Evolution of the systematic deviation downstream the slit mask, resolution of 100 $lines/mm$, the influence of initial beamlet size is subtracted. The initial conditions are as the case of 1 nC and CDS booster.

On figure 8.2 the systematic deviation as a function of L_d is shown where the optical resolution was increased to 100 $lines/mm$ and the influence of the initial slit opening is excluded. It is interesting that initially the deviation is smaller for 50 than for 10 μm slit opening. This is explained with the fact that the systematic deviation is dominated entirely from the optical resolution, the beamlet size out of the 50 μm slit is larger which reduces the influence of the optical resolution in the first meters downstream the slit mask.

In table 8.5 a summary of the performance of the slit based measurement

is given, when the initial beamsize is subtracted and an optical resolution of 100 $lines/mm$ is applied. The systematic deviation is reduced with 5 to 10 % in all of the cases.

Table 8.5: Emittance and systematic deviation in percent for the optimized parameters. In this case the optical resolution is 100 $lines/mm$ and the initial beamlet size is subtracted for the divergence estimation.

charge, $[nC]$	TESLA			CDS		
	ε_n	$\Delta\varepsilon_{min}$	L_d^{min}	ε_n	$\Delta\varepsilon_{min}$	L_d^{min}
0.07	0.102	8.2	4	0.123	7.7	1.56
0.2	0.209	6.2	3.75	0.219	5.3	4
0.5	0.429	5.3	4	0.368	5.5	4
1.0	0.714	4.1	2.70	0.618	4.4	4

In order to have reliable measurements for the optimized cases shown above, an optical resolution of 100 $lines/mm$ is needed. The initial beamlet size should be also subtracted to cancel the influence of the finite slit opening.

Chapter 9

Conclusions

9.1 Summary

A low emittance photo-injector has been developed and its emittance was studied at PITZ. Two identical gun prototypes were installed, commissioned and optimized under different conditions in the period 2006-2007. A reduction of the normalized emittance from $1.37^{+0.12}_{-0.1} \pm 0.1\ mm{\cdot}mrad$ to $1.27^{+0.02}_{-0.07} \pm 0.15\ mm{\cdot}mrad$ is achieved with increase of the maximum accelerating gradient at the photo cathode.

The existing emittance measurement system (EMSY) at PITZ was optimized successfully to measure small emittance at wider mean momentum range. The optimization of EMSY includes the slit masks, screen setup and readout system and the drift length after the slit. The sources of systematic uncertainties such as influence from the space charge, screen and camera calibration etc. were studied and error maps for the most important photo-injector variables were created. An automatic measurement procedure was developed which allows faster and more reliable measurements.

The emittance compensation principle in a photo-injector was experimentally studied using the PITZ setup and the improved emittance measurement system. We can conclude that:

- higher gun gradients result in a decreased projected emittance
- applying additional booster acceleration leads to decrease of the emittance

- the optimal initial rms size of the electron beam is 0.55 mm for 40 MV/m and 0.35 mm for 60 MV/m
- the solenoid current is the most sensitive photo-injector parameter

The smallest normalized projected rms emittance measured at PITZ was ε_{xy} =$1.27^{+0.02}_{-0.07}$±0.15 $mm \cdot mrad$. This value is a geometrical average in both transverse planes. It was obtained with maximum gradient in the gun cavity of ∼60 MV/m, mean beam momentum of 6.46 MeV/c, after the gun and 14.45 MeV/c, after the booster. The initial laser rms spot size was 0.35 mm. This measurement is in good agreement with the emittance minimum obtained from ASTRA simulations. Still the discrepancy between the expected parameter dependence in the numerical simulations and the obtained results is to be understood. In addition, the emittance enclosed in an equidensity contour including 90 % of the total charge and the core emittance were calculated. They were $\varepsilon^{90\%}_{xy}$ =0.939±0.12 $mm \cdot mrad$ and $\varepsilon_{c,x} = 0.587$, $\varepsilon_{c,y} = 0.664$ $mm \cdot mrad$, respectively.

A numerical optimization algorithm called Simplex Wide Area Routing Method (SWARM) was developed to minimize the transverse emittance in the photo-injector. It was applied for bunch charge of 1.0, 0.5, 0.2, 0.07 nC and for two different booster cavities, i.e. the presently installed TESLA type and a newly developed CDS. Transverse projected emittance of 0.618 $mm \cdot mrad$ was obtained with 1 nC bunch charge, when higher acceleration with the CDS booster cavity was applied. At lower bunch charge of 0.07 nC, the emittance was as low as 0.102 $mm \cdot mrad$.

The performance of the single slit method was estimated for various bunch charges with the numerically optimized photo-injector parameters. The systematic deviation in these cases was dominated by the small beamlet size, typicaly less than 70 μm. In order to reduce the systematic deviations at lower charges, the optical resolution of the system needs to be improved and the initial beamlet size subtracted from the divergence measurement.

9.2 Outlook

In the near future, the installation of a new type of booster cavity providing higher accelerating gradients and better field uniformity, together with a ma-

jor upgrade of the laser system will allow to study the transverse normalized emittance below 1 $mm \cdot mrad$ at 1 nC bunch charge.

Upgrade of the transverse beamsize diagnostic to 12 bit cameras at each screen as well as improvement of the optical lense setup will enhance the performance of the emittance measurement system widening our possibility to study beams with small emittance in broader range of photo-injector parameters.

Appendix A

Image analysis

After the acquisition of the beam image data from the carefully optimized measurement system, the next step is to extract the most correct amount of information from the resulting distributions. For this a set of algorithms for image processing was developed at PITZ, from Velizar Miltchev and the author of this thesis.

A digital image is defined as a 2-dimensional rectangular array of quantized brightness levels (pixels). The image analysis is done in order to distinguish if the reading from each particular pixel comes from useful signal, i.e. beam or beamlet, or is associated to dark current, camera noise and/or other parasitic effects such as reflections from components of the acquisition system etc. After selecting the pixels containing signal, the statistic central moments of the resulting distributions are calculated.

The image processing can be divided into three steps:

- background analysis
- signal processing
- calculation of the central moments of the resulting distribution

A.1 background analysis

The background signal is analyzed typically over 50 independent images acquired in sequence. The reading in each pixel is averaged and the standard deviation is calculated. On figure A.1 the raw image before any background

analysis is shown, the result from the calculation of the rms size is dominated strongly by the presence of the background.

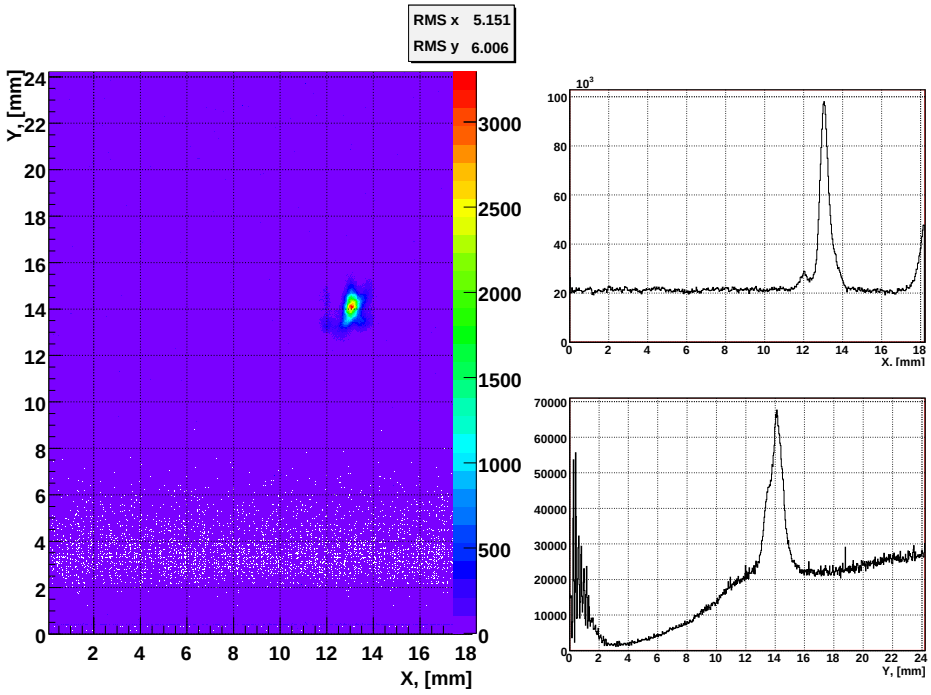

Figure A.1: Beamlet and background. Image (left) and projections (right).

A.2 signal processing

The next step is pixel by pixel comparison between the average values of the signal and the background image. If the signal height in the examined pixel does not exceed one standard deviation of the background, the reading is considered as noise and the value in the pixel is set to zero. The result from this operation is shown on figure A.2. Still the rms calculation is strongly influenced by the presence of background. One can see that noise with amplitude higher than one standard deviation consist mostly of single pixels scattered randomly in the image area. Therefore, the next test we perform is if the signal reading belongs to a large cluster of pixels or is solely. If one of the direct following neighbors of pixel $P_{i,j}$ is zero, the reading is considered as noise and its weight set to null. In other words the product of $P_{i,j} \cdot P_{i+1,j} \cdot P_{i,j+1} \cdot P_{i+1,j+1}$ must

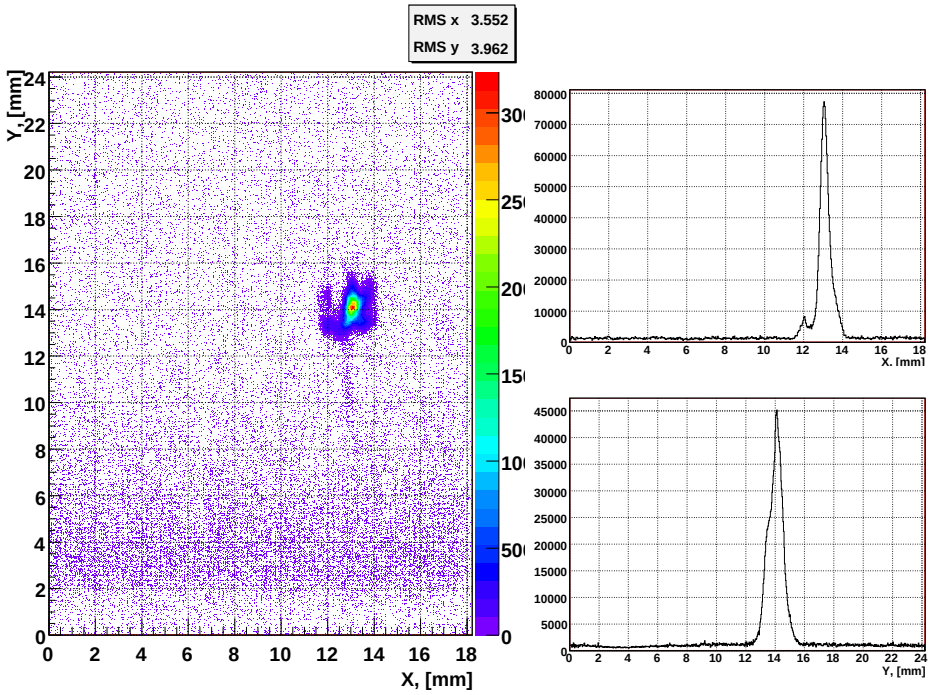

Figure A.2: Background subtracted from the beamlet. Image (left) and projections (right).

be greater than zero in order to consider the signal in pixel $P_{i,j}$. The result of such a test is shown on figure A.3. Large fraction of the noise was removed and what remains are again randomly scattered pixels that due to their big displacement from the beamlet signal are bringing large contribution to the rms size of the image. It is easy to select an area around the visible signal in order to exclude the pixels with large displacement from the main signal but this needs a subjective decision from skillful operator and can not be automatized. Therefore, the last operation is repeated until all the suspicious pixels are nullified. Typically this is done three times or in other words the signal area must have a radius exceeding three pixels in order to be considered as useful reading. Since in this operation also the real signal radius is reduced by the same amount, the last operation of the signal processing is to restore the area around the remaining signal with as much as it has been shrinked.

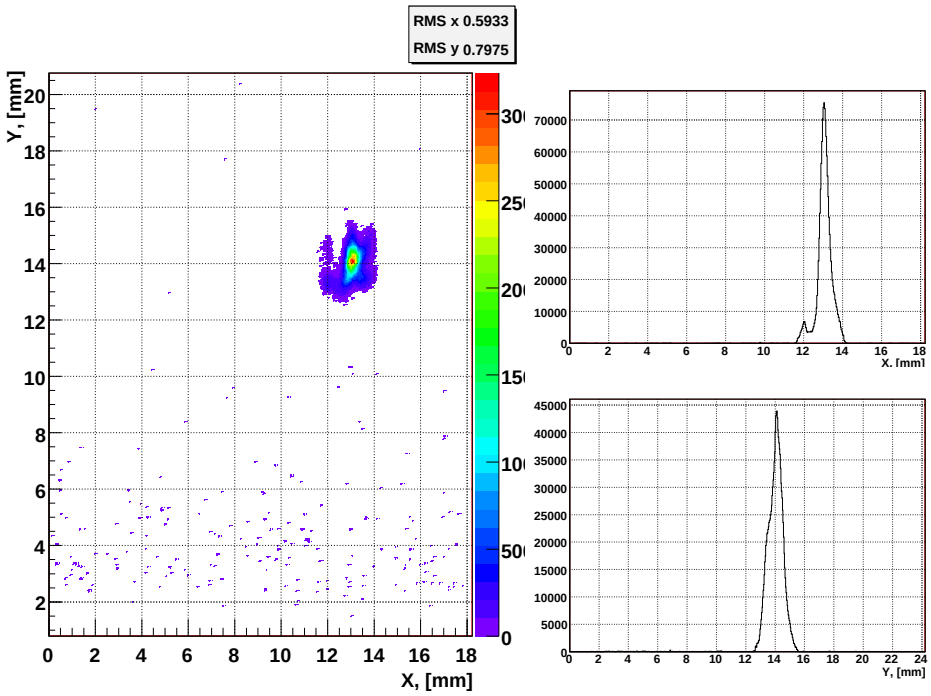

Figure A.3: Background subtracted from the beamlet and single pixels are filtered. Image (left) and projections (right).

On figure A.4 the result from different depth of noise filtering is shown, one can see the effect from the increased area of the filter but the calculation of the rms remains stable within the second digit after the coma. The results are summarized in table A.1

Table A.1: Comparison of results from the rms calculation between filtering of noise with different area.

area radius in pixels	**X rms,** $[mm]$	**Y rms,** $[mm]$
0	0.5468	0.6367
1	0.3866	0.4853
2	0.3838	0.4817
3	0.3812	0.4827

In order to test the efficiency of this image processing algorithm for signal with different amplitude or in other words for different signal to noise ratio, the

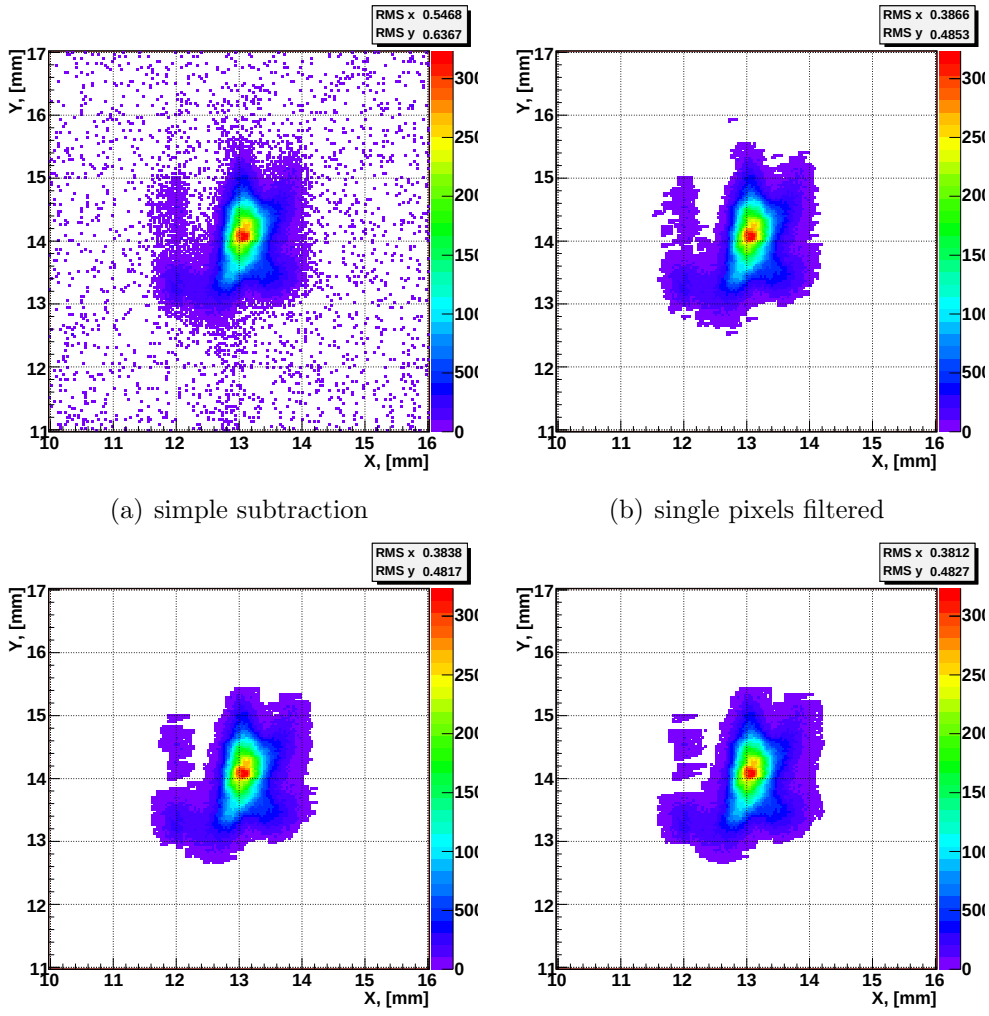

(a) simple subtraction

(b) single pixels filtered

(c) double pixels filtered

(d) triple pixels filtered

Figure A.4: Comparison between filtering of noise with different areas.

procedure described above was applied to artificially generated Gaussian distributions using the same background image as shown above. The dimensions of the Gaussian distributions are 0.5 mm rms size of a symmetric distribution and 0.5 and 0.2 mm rms sizes for an asymmetric one. The result is shown on figure A.5, it can be seen that this procedure is rather stable in wide range of signal intensities.

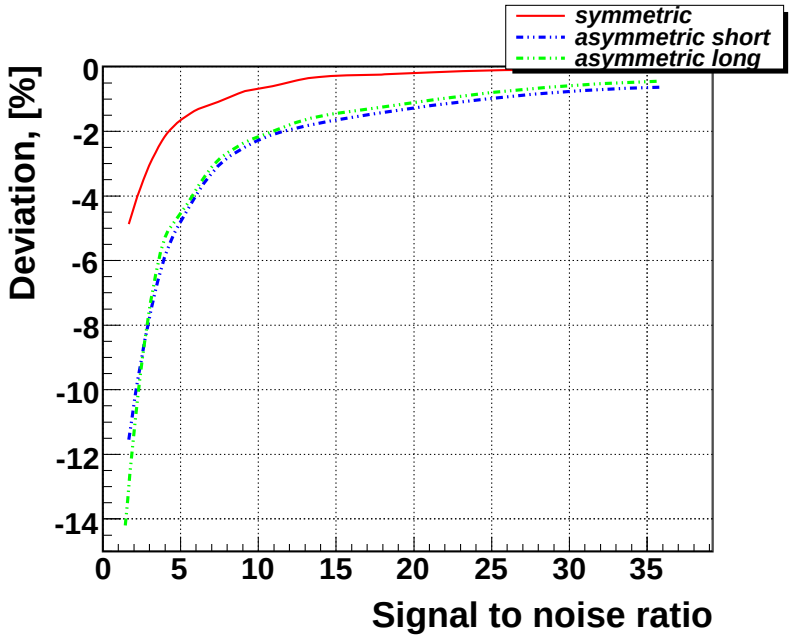

Figure A.5: Deviation of the results from the image processing for different signal to noise ratio of the signal.

Appendix B

Procedures for emittance measurements

The emittance measurements are on the top of the measurement food-chain at PITZ. As such, the preparation of the photo-injector for emittance measurement and sustaining the proper conditions is a complex multi loop task involving adjustment of sensitive parameters and monitoring number of machine and beam characteristics.

A description of how to prepare the photo-injector for emittance measurement and how the measurement is conducted will be given next.

B.1 Machine preparation

B.1.1 Laser beam

The laser beam must have round and homogeneous transverse profile and a flat top longitudinal distribution with FWHM about 20 ps and rise/fall times in the order of 6 ps. The power of the laser set such to deliver electron bunches with charge of 1 nC for each one of the emittance measurements. In the beginning of the measurements of emittance both the longitudinal and the transverse laser distribution must be recorded using sufficient statistics of both the signal and the background i.e. 50 image frames for the transverse distribution.

B.1.2 RF gun cavity

The phase of the RF with respect to the laser pulse is the most sensitive RF gun parameter. The control of phase is done by measuring the mean momentum of the electron bunch using the low energy dispersive arm, located at approximately 1 m downstream the cathode. The phase at which the mean beam momentum is at maximum is referred to as $\phi_{gun} = 0,\ deg$. After obtaining the set point phase coresponding to the maximum momentum the power of the laser must be adjusted so that to provide the nominal charge (1 nC per bunch).

Measurement of the momentum distribution of the electron bunch after the gun is necessary for better comparison of the results from the emittance measurements with simulations.

B.1.3 Booster cavity

The phase of the booster cavity is determined the same way, but the high energy dispersive arm is used. The phase at which the mean beam momentum after the booster is at maximum is referred to as $\phi_{booster} = 0,\ deg$.

Measurement of the final momentum distribution of the electron bunch is critical for obtaining the result from the emittance measurements.

B.1.4 Beam trajectory

Before the emittance measurements, the beam distribution must be observed on each of the screens downstream the screen where the measurements are to be taken. This is necessary in order to verify if the beam is not penetrated from any of the existing apertures. Accordingly the trajectory of the beam must be corrected to remove any visible influence. Usually this means that the beam center coinside with the center of the screens.

B.2 Emittance measurements

After setting up the desired parameters in the machine, the emittance measurement can start. For to unify the measurement procedure in order to optimize the speed of the measurement and to mitigate the subjective human factor, a

computer program for automatization of the measurements is developed.

The emittance measurement is initiated with measurement and recording of the transverse beam distribution at the screen where the slit mask is located. The signal from the camera must be optimized such that the full dynamic range of the device is used in order to collect as much details as possible. Next step is to measure the distribution of the full beam at the screen where the beamlets are to be measured. This is necessary for relaxing the noise and background subtraction procedures.

The next step is determination of the slit position across the beam coresponding to the beamlet with the maximum peak intensity. There the light signal is adjusted such that the full range of the camera amplitude resolution is used. This assures that the widest range of beamlet intensity can be recorded.

Final step of the measurement is performing scan with the slit across the beam and recording at minimum 11 equidistant beamlets. The step size is adjusted such that the lateral beamlets are with the smallest intensity possible.

B.3 Data consistency

In order to have more reliable and comprehensive measurement results, several criteria for data consistency were elaborated at PITZ. Those include the completeness and the quality of the data as well as the available auxiliary information.

B.3.1 Completness of data

The absence of any of the following parameters makes the analysis of the data impossible: the beamsize at the slit mask position, the drift length between the slit mask and the screen, the final beam momentum and the slit scan itself. As consistent slit scan those with at least 11 equidistant slit positions across the beam is accepted. In addition in order to enable the analysis on the phase space distribution, the actuator positions during the scan must also be known.

B.3.2 Quality of the data

The stability of the machine operation is important for the reliability of the acquired data. M. Krasilnikov has estimated that a jitter of the beam position on the slit mask can dilute the phase space portrait creating up to 30 % of emittance overestimation.

Another very important aspect of the data quality is the image intensity, one must allways operate the cameras in such a way that to use the largest amount of amplitude range. It was estimated that for the 8 bit JAI cameras the most reliable regime is when the signal amplitude is more than 200. For the 12 bit Prosilica, this limit is 3000.

B.3.3 Auxiliary information

This is all the data which is not directly connected to the emittance measurements, but the absence of which obscures the understanding or the proper interpretation of the results. As *mission critical* auxiliary information is considered, the current in the main and the bucking solenoids, the cavity/ies phase/s and accelerating gradient/s, the laser transverse and longitudinal distribution and the charge of the bunch. All these data are necessary for the unilateral comparison between the experimental results and the theoretical or numerical estimations. For improved understanding of the results, scan of various beam parameters such as the charge dependence on the gun phase, the beamsize downstream the cathode or as a function of I_{main}. Other important beam parameters are the electron bunch longitudinal distribution, the beam momentum before the booster cavity, the number of the laser pulses in the train etc.. It is obvious that this list can be extended until it include a complete set of the machine and beam parameters. The above list tries to summarize the most important photo-injector parameters from the emittance measurement point of view.

Bibliography

[1] K. Wille. *The Physics of Particle Accelerators, an introduction.* Oxford, 2000.

[2] M.V.Yurkov E. L. Saldin, E. A. Schneidmiller. *The Physics of Free Electron Lasers.* Springer, 2000.

[3] K. Flötmann, F. Stephan. *RF Photoinjectors as Sources for Electron Bunches of Extremely Short Length and Small Emittance.* Internal note, DESY, 1999.

[4] V. Ayvazyan et al. "*Generation of GW Radiation Pulses from a VUV Free-Electron Laser Operating in the Femtosecond Regime*". Phys. Rev. Lett., **88**(10):104802, February 2002.

[5] J. Rossbach, For the TTF FEL Group. *Demonstration of gain saturation and controlled variation of pulse length at the TESLA test facility FEL.* Nuclear Instruments and Methods in Physics Research Section A: Accelerators, Spectrometers, Detectors and Associated Equipment, **507**:362-367(6), 11 July 2003.

[6] XFEL Collaboration. *The European X-Ray Free-Electron Laser - Technical Design Report.* Published by DESY XFEL project group, 2006.

[7] W. Ackermann et al. *Operation of a free-electron laser from the extreme ultraviolet to the water window.* Nature Photonics, **1**:336-342(7), June 2007.

[8] J. Rossbach et al. *Fundamental limitations of an X-ray FEL operation due to quantum fluctuations of undulator radiation.* Nuclear Instruments

and Methods in Physics Research Section A: Accelerators, Spectrometers, Detectors and Associated Equipment, **393**:152-156(5), 1 July 1997.

[9] J. Rossbach et al. *Interdependence of parameters of an X-ray FEL.* Nuclear Instruments and Methods in Physics Research Section A: Accelerators, Spectrometers, Detectors and Associated Equipment, **374**:401-407(7), 1 June 1996.

[10] B. Faatz et al. *Parameter optimization of X-ray free-electron lasers at a linear collider.* Nuclear Instruments and Methods in Physics Research Section A: Accelerators, Spectrometers, Detectors and Associated Equipment, **407**:302-306(5), 21 April 1998.

[11] L. Serafini, J. Rosenzweig . *Envelope analysis of intense relativistic quasilaminar beams in rf photoinjectors:mA theory of emittance compensation* . Phys. Rev. E, **55**(6):7565–7590(25), June 1997.

[12] THALES group. www.thalesgroup.com/electrondevices.

[13] M. Krasilnikov et al. *Experimental characterization and numerical simulations of the Electron Source at PITZ.* Proceedings of the 8th International Computational Accelerator Physics Conference (ICAP 2004), St. Petersburg, Russia, 29 Jun - 2 Jul 2004.

[14] J.Bähr et al. *Upgrade of the Laser Beam-line at PITZ.* Proceedings of the 27th International Conference on Free Electron Lasers (FEL2005), Palo Alto, California, USA, August 21-26, 2005.

[15] M.Hänel et al. *Photo Cathode Laser Pulse Diagnostics At PITZ.* Proceedings of the 29th International Free Electron Laser Conference (FEL2007), Novosibirsk, Russia, August 26-31, 2007.

[16] Y. Ivanisenko. *Photo Injector Cathode Laser Beam Intensity and Position Monitoring System.* Master's thesis, Karazin Kharkiv National University, Ukraine, 2007.

[17] Hamamatsu photonics. *Universal streak kamera C5680 Series. Manual.*

[18] M. Krasilnikov et al. *Experimental Optimisation of the Cathode Laser Temporal Profile.* Proceedings of 8th European Workshop on Beam Diagnostics and Instrumentation for Particle Physics (DIPAC2007), Venice, Italy, May 20-23, 2007.

[19] http://tesla.desy.de/doocs/doocs.html. *DOOCS: a Distributed Object Oriented Control System.*

[20] P. Bartkiewicz, P. Duval. *TINE as an accelerator control system at DESY.* Measurement Science and Technology, **18**(8):2379-2386, 2007.

[21] P. Michelato. *Photocathodes for RF photoinjectors.* Nuclear Instruments and Methods in Physics Research A, **393**(1):455-459, 1997.

[22] S. Schreiber et al. *Properties of Cathodes used in the photoinjector RF gun at the DESY VUV-FEL.* Proceedings of 9th European Particle Accelerator Conference (EPAC2004), Lucerne, Switzerland, 5 - 9 July, 2004.

[23] S. Lederer. *Reliability studies of photocathodes at PITZ and FLASH.* Technical report, EUROFEL, Report-2007-DS1-041, 2007.

[24] K. Flöttmann et al. *RF gun design for the TESLA VUV Free Electron Laser.* Nuclear Instruments and Methods in Physics Research A, **393**:93-95, February 1997.

[25] J-P. Carneiro et al. *Behaviour of the TTF2 RF Gun with long pulses and high repetition rates.* Technical report, TESLA Note 2003-33, 2003.

[26] S. Rimjaem et al. *Status And Perspectives Of The PITZ Facility Upgrade.* Proceedings of the 29th International Free Electron Laser Conference (FEL2007), Novosibirsk, Russia, August 26-31, 2007.

[27] A. Oppelt et al. *Tuning, Conditioning and Dark Current Measurements of a New Gun Cavity at PITZ.* Proceedings of the 28th International Conference on Free Electron Lasers (FEL2006), Berlin, Germany, August 27 to September 1, 2006.

[28] V. Miltchev. *Investigations on the transverse phase space at a photo injector for minimized emittance.* PhD thesis, Humboldt-Universität zu Berlin, DESY-THESIS-2006-025, 2006.

[29] L. Staykov. *Calibration of the solenoids in PITZ - 2003.* Technical report, DESY Zeuthen, 2005.

[30] C. Wang et al. *Criteria for emittance compensation in high-brightness photoinjectors.* Phys. Rev. ST Accel. Beams, **10**(10):104201(7), October 2007.

[31] A. Oppelt et al. *Status and first results from the upgraded PITZ facility.* Proceedings of the 27th International Free Electron Laser Conference (FEL 2005), Stanford, USA, August 21-26, 2005.

[32] V. Paramonov et al. *Desgign Parameters Of The Normal Conducting Booster Cavity For The PITZ-2 Test Stand.* Proceedings of 22nd International Linear Accelerator Conference (LINAC2004), Lübeck, Germany, August 16-20, 2004.

[33] http://www.bergoz.com/. *ICT-178-2-XXX-X.*

[34] D. Lipka. *Untersuchungen zum longitudinalen Phasenraum an einem Photoinjektor für minimale Strahlemittanz.* PhD thesis, Humboldt-Universität zu Berlin, DESY-THESIS-2004-021, 2004.

[35] J. Rönsch et al. *Investigations of the Longitudinal Phase Space at PITZ.* Proceedings of 10th European Particle Accelerator Conference (EPAC2006), Edinburg, Scotland, June 23-30, 2006.

[36] H-J. Grabosch et al. *Test of a Wire Scanner in the Diagnostic Section of PITZ.* Proceedings of the 29th International Free Electron Laser Conference (FEL2007), Novosibirsk, Russia, August 26-31, 2007.

[37] JAI Ltd. . *CV-M10SX Monochrome Progressive Scan Camera, Operation manual.* JAI industries, http://www.jai.com/.

[38] Prosilica Inc. *High Performance CCD and CMOS Cameras for Industrial Applications.* http://www.prosilica.com/, 2007.

[39] S. Weisse et al. *Status of a versatile Video System at PITZ, DESY-2 and EMBL Hamburg.* Proceedings of the International Conference on Accelerator and Large Experimental Physics Control Systems (ICALEPCS2007), Knoxville, Tennessee, USA., October 15 - 19, 2007.

[40] L. Staykov. *Design Optimization of an Emittance Measurement System at PITZ.* Proceedings of 7th European Workshop on Beam Diagnostics and Instrumentation for Particle Accelerators (DIPAC2005), Lyon, France, June 6 - 8, 2005.

[41] K. Flöttmann. *Some basic features of the beam emittance.* Phys. Rev. ST Accel. Beams, **6**(3):034202(7), March 2003.

[42] B. Carlsten. *New photoelectric injector design for the Los Alamos National Laboratory XUV FEL accelerator.* Nuclear Instruments and Methods in Physics Research Section A: Accelerators, Spectrometers, Detectors and Associated Equipment, **A285**:313-319, 10 December 1989.

[43] J-H. Han. *Dynamics of Electron Beam and Dark Current in Photocathode RF guns.* PhD thesis, Universität Hamburg, DESY-THESIS-2005-045, 2005.

[44] K. Flöttmann. *Note on the Thermal Emittance of Electrons Emitted by Cs_2Te Photo Cathodes.* TESLA-FEL internal note 97-01, 1997.

[45] K-J. Kim. *RF and space-charge effects in laser-driven rf electron guns.* Nuclear Instruments and Methods in Physics Research Section A: Accelerators, Spectrometers, Detectors and Associated Equipment, **275**(2):201-218, February 1989.

[46] S. Hartman, J. Rosenzweig. *Ponderomotive focusing in axisymmetric rf linacs.* Phys. Rev. E, **47**(3):2031–2037(6), March 1993.

[47] C. Lejeune, J. Aubert. *Emittance an Brightness: Definitions and Measurements.* Academic Press inc., Advances in electronics and electron physics/Supplement 13A, ISBN 0-12-014573-1, 1980.

[48] B. Carlsten, D. Palmer. *Enhanced emittance compensation in high-frequency RF photoinjectors.* Nuclear Instruments and Methods in Physics Research Section A: Accelerators, Spectrometers, Detectors and Associated Equipment, **425**(1):37-50, 1 April 1999.

[49] M. Ferrario et al. *Recent Advances And Novel Ideas For High Brightness Electron Beam Production Based On Photo-Injectors.* SPARC-BD-

03/003, LNF-03/06 (P), 5 Maggio 2003, Invited talk at the ICFA Workshop on The Physics and Applications of High Brightness Electron Beams, Chia Laguna, Sardina, Italy, July 1-6, 2002.

[50] C. Wang. *Comment on the invariant-envelope solution in rf photoinjectors*. Nuclear Instruments and Methods in Physics Research A, **557**:94-97, February 2006.

[51] M. Ferrario et al. *Conceptual Design of the XFEL Photoinjector*. Technical report, TESLA FEL Report 2001-03, 2001.

[52] M. Ferrario et al. *HOMDYN study of the LCLS RF photoinjector*. Contributed to 2nd ICFA Advanced Accelerator Workshop on the Physics of High Brightness Beams, Los Angeles, California, 9-12 November 1999, SLAC-PUB-8400.

[53] B. Carlsten et al. *Measuring emittance of nonthermalized electron beams from photoinjectors*. Nuclear Instruments and Methods in Physics Research A, **331**:791-796, July 1993.

[54] S. Anderson, et al. *Space-charge effects in high brightness electron beam emittance measurements*. Phys. Rev. ST Accel. Beams, **5**(1):014201(12), January 2002.

[55] J. Rosenzweig, G. Travish,. *Design Considerations for the UCLA PBPL Slit-based Phase Space Measurement Systems*. UCLA Department of Physics, PBPL Tech. Note 64, 1994.

[56] P. Piot. *Zeroth-Order Considerations for a single slit-based Emittance Diagnostics at the PITZ facility*. Technical report, DESY Hamburg, 2000.

[57] V. Miltchev. *Construction and Commissioning of a Transverse Emittance Measurement System for the Photoinjector Test facility at DESY Zeuthen*. Master's thesis, Humboldt-Universität zu Berlin, June 2002.

[58] F. Stephan et al. *First Measurements at the Photo Injector Test Facility at DESY Zeuthen*. Proceedings of the 8th European Particle Accelerator Conference (EPAC2002), La Villette-Paris, France, June 3-7, 2002.

[59] R. Bakker et al. *First beam measurements at the photo injector test facility at DESY Zeuthen.* Nuclear Instruments and Methods in Physics Research Section A: Accelerators, Spectrometers, Detectors and Associated Equipment, **507**:210-214(5), 11 July 2003.

[60] V. Miltchev et al. *Transverse Emittance Measurements at the Photo Injector Test Facility at DESY Zeuthen (PITZ).* Proceedings of 6th European Workshop on Beam Diagnostics and Instrumentation for Particle Accelerators (DIPAC03), Mainz, Germany, 5 - 7 May 2003.

[61] A. Oppelt et al. *Future plans at the Photo Injector Test Facility at DESY Zeuthen.* Proceedings of the 25th International Free Electron Laser Conference and the 10th FEL Users Workshop, Tsukuba, Ibaraki, Japan, 8-12 September 2003.

[62] A. Oppelt et al. *Status of the PITZ Facility Upgrade.* Proceedings of the 24th Internal Linear Accelerator Conference (LINAC2006), Knoxville, TN, USA, 21-25 August 2006.

[63] K. Flöttmann. *Pepper Pot Design for Space Charge Dominated High Brightness Beams.* TESLA-FEL internal note 96-09, 1996.

[64] L. Serafini, J. Rosenzweig and S. Anderson. *Space charge dominated envelope dynamics of asymmetric beams in RF photoinjectors.* Number 1997. Particle Accelerator Conference (PAC'97), Vancouver, B.C., Canada, 12-16 May 1997.

[65] GEANT collaboration. *Geant4: A toolkit for the simulation of the passage of particles through matter.* CERN, http://www.geant4.org/geant4/.

[66] R. Spesyvtsev, L. Staykov, S. Khodyachikh. *SCREEN STUDIES AT PITZ.* Proceedings of 8th European Workshop on Beam Diagnostics and Instrumentation for Particle Physics (DIPAC2007), Venice, Italy, May 20-23, 2007.

[67] R. Spesyvtsev. *Transverse Beam Size Measurement Systems at Photo Injector Test Facility in Zeuthen.* Master's thesis, Karazin Kharkiv National University, Ukraine, 2007.

[68] K. Flötmann. *A Space Charge Tracking Algorithm.* DESY Hamburg, http://www.desy.de/~mpyflo/.

[69] I. Bazarov, C. Sinclair. *Multivariate optimization of a high brightness dc gun photoinjector.* Phys. Rev. ST Accel. Beams, **8**(3):034202(7), March 2005.

[70] http://wwwlasa.mi.infn.it/ttfcathodes. *TTF Photocathodes Database.* Technical report, INFN LASA Milano, since 2003.

Acknowledgements

I would like to express my sincere gratitude to all the people who helped me create this thesis:

Professor Jörg Rossbach from the Institut für Experimentalphysik in University of Hamburg for presenting me with the honour to accomplish my doctoral study in his group for Accelerator Physics.

Professors Ivan Tsakov and Jordan Stamenov from the Institute for Nuclear Research and Nuclear Energy in Sofia for introducing me to the people in DESY and for the continuous backup when I needed it.

Ulrich Gensch for his decisive support and trust through all these years.

All members of the PITZ project since year 2003, in particular to Frank Stephan and Mikhail Krasilnikov for the useful things they taught me; Velizar Miltchev for the kind introduction to the secrets of the photo-injector phase space characterisation; Bagrat Petrosyan and Gunter Trowitzsch for software support and lovely interactions in the process; Jürgen Bähr and Anne Oppelt for helping me deal with all the documentation about ordering, sending and receiving scientific equipment in Germany and EU; Hartmut Lüdecke, Jochen Bienge, Luchezar and Hristo Yotovi for the precise mechanical support; Sergiy Khodyachikh for the helpful jokes and advices, and Chase Boulware for the proof reading of my thesis and useful discussions.

Siegfried Schreiber, Katja Honkavaara and Klaus Flöttmann from DESY, Hamburg site and Thorsten Kamps from BESSY, for the fruitful discussions and whole lots of fun.

Professors Georg Höffstaedter and Ivan Bazarov from Cornell University for their hospitality and helpful discussions on photo-injector optimisation. The knowledge we shared had a great influence on this thesis.

Nick Cave and The Bad Seeds for enriching my English and releasing their great album *Dig, Lazarus, Dig!* in the most difficult time of writing the thesis.

I would like to thank as well to my friends in Germany who supported my *Sprache* efforts and shared their amity in this urban landscape.

Special thanks I owe to Galina Asova, for sharing her coding experience, her coffee and the atmosphere in the office.

Most of all I would like to thank to my lovely family, Margarita and Vihra and to my parents who stayed by me all these days and nights and never failed me in return.

Thank You All!